UNIVERSITÀ
DEGLI STUDI
FIRENZE

DOTTORATO DI RICERCA IN
SCIENZE CHIMICHE

CICLO XXIX

COORDINATORE Prof. PIERO BAGLIONI

Optimization of components for Dye-Sensitized Solar Cells: a combined approach for performance improvement.

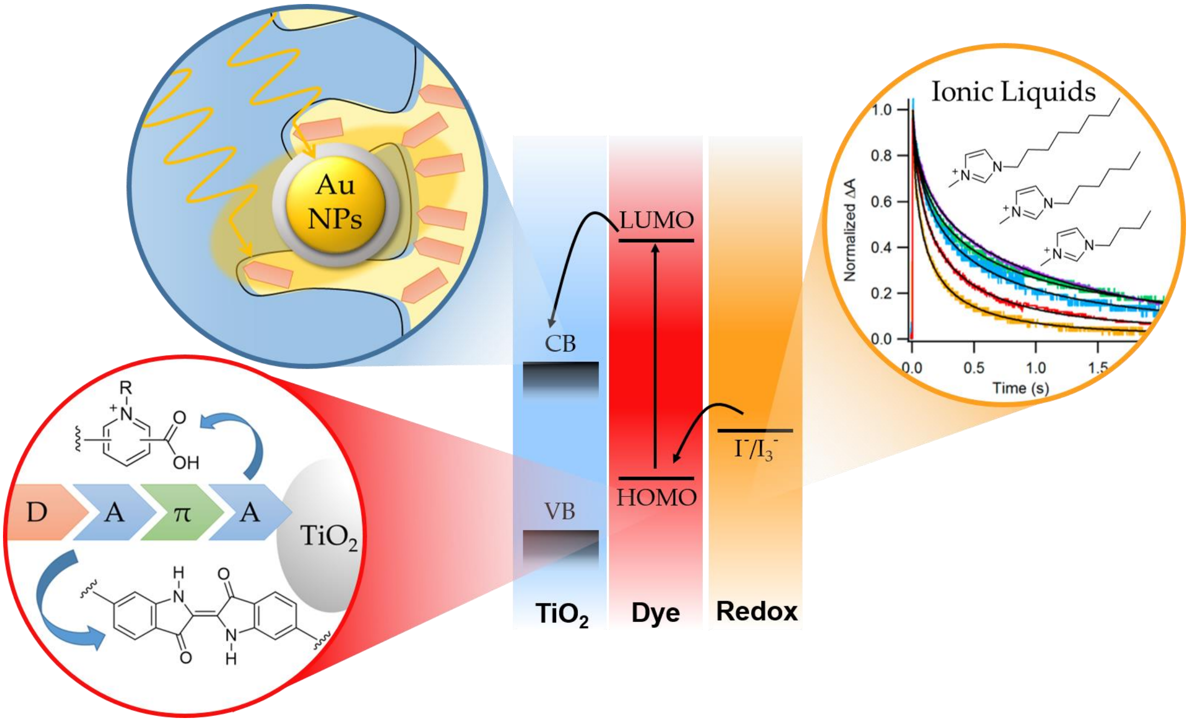

Dottorando
Dr. Daniele Franchi

Tutore
Dr. Alessandro Mordini

UNIVERSITÀ
DEGLI STUDI
FIRENZE

DOTTORATO DI RICERCA IN
SCIENZE CHIMICHE

CICLO XXIX
COORDINATORE Prof. PIERO BAGLIONI

Optimization of components for Dye-Sensitized Solar Cells: a combined approach for performance improvement.

Settore Scientifico Disciplinare CHIM/06

Dottorando
Dr. Daniele Franchi

Tutore
Dr. Alessandro Mordini

Coordinatore
Prof. Piero Baglioni

Anni 2013/2016

Table of content

Chapter 1 – Introduction

Chapter 2 - Aim of the work

Chapter 3 – Dyes

Chapter 4 – Gold Nanoparticles

Chapter 5 – Ionic Liquids

Chapter 6 – Conclusions

Abstract

Photovoltaic devices are capable of converting light into an orderly flow of charges also known as Electricity. Dye-Sensitized Solar Cells (DSSCs) are new-generation photovoltaic devices in which the component capable of absorbing light and creating a separation of electric charges are dye molecules adsorbed on a semitransparent thin layer of a semiconductor.

Despite their simple architecture, DSSCs are devices characterized by a very complex entanglement of physical variables, each one interacting with the others to determine macroscopic features of the device. For example: the energy levels of the photoactive compound set limits on the portion of solar light that will be absorbed; the orbital overlap between the semiconductor substrate and the dye rule on the electron injection; the electron density on the solid surface and the ions concentration in the liquid charge carrier shape the outcome voltage. The all of this parameters, and many more, needs to be tuned each other to convert the solar energy with the best efficiency.

In this piece of writing, I am analyzing tree of the main parts of DSSCs: the semiconductor solid surface, the photoactive dye material, and the electrolyte charge transporter. Not only will efficiency issue be addressed, but also longevity of the devices, generally hampered by dye degradation or electrolyte evaporation; esthetical needs such as transparency and color; and deep understanding of nanocomposites or ionic liquids application response will be addressed.

Annex

Abbreviations

Ac_2O	Acetic anhydride
acac	Acetylacetonate
ACN	Acetonitrile
AM	Air Mass
APTES	(3-aminopropyl)triethoxysilane
a-Si	Amorphous Silicon
BAI	Bay-Annulated Indigo
BID	Biimidazolylidene-dione
BMIM	1-butyl-3-methylimidazolium
Boc	*tert*-butoxy carbonyl
CB	Conduction Band
CDCA	Chenodeoxycholic acid
CdTe	Cadmium Telluride
CIGS	Copper Gallium Indium Selenide
CTAB	Cetyl-trimethylammonium bromide
dcb	2,2′-Bipyridine-4,4′-dicarboxy
DFT	Density Functional Theory
DLS	Dynamic Laser Scattering
DMAP	N, N-dimethylpyridin-4-amine
DMF	Dimethyl formaldehyde
DPP	Diketopyrrolopyrrole
DSSC	Dye-Sensitized Solar Cell
E^*_{OX}	Excited-state oxidation potential
E_{0-0}	Optical band gap energy
EC	Ethylcellulose
E_{EXC}	Vertical excitation energies
E_F	Fermi Level potential
E_{OX}	Ground-state oxidation potential
EPBT	Energy Payback Time
EROI	Energy Return on Investment
Et_2O	Diethyl Ether
EtGly	Ethyleneglycol
EtOAc	Ethyl Acetate
EtOH	Ethanol
EWG	Electron withdrawing

f	Oscillator strengths
ff	Fill Factor
FTO	Fluorine doped Tin oxide
HMIM	1-hexyl-3-methylimidazolium
HOMO	Highest Occupied Molecular Orbital
IL	Ionic Liquid
IPCE	Incident Photon-to-electron Conversion Efficiency
i-PrOH	*Iso*-propanol
J_{SC}	Short Circuit Current
k_{KWW}	KWW back electron-transfer rate constant
KWW	Kohlrausch-Williams-Watts (kinetic model)
LUMO	Lowest Unoccupied Molecular Orbital
MAA	Mercapto-Acetic Acid
MeOH	Methanol
MPTMS	(3-mercaptopropyl) trimethoxysilane
MSSC	Meso-Superstructured Solar Cell
NBS	N-Bromosuccinimide
NFE	Near-Field Enhancement
NIR	Near Infrared
NP	Nanoparticle
OMIM	1-octyl-3-methylimidazolium
PAN	Polyacrylonitrile
PE	Petroleum Ether
Poly-Si	Polycrystalline silicon
ProDOT	3,3-dipentyl-3,4-dihydro-2H-thieno[3,4-b][1,4]dioxepine
p-TsOH	*Para*-Toluenesulfonic acid
PV	Photovoltaic
r.t.	Room temperature
sc-Si	Single-crystal Silicon
SPR	Surface Plasmon Resonance
TCO	Thin Conducting Oxide
THF	Tetrahydrofuran
toe	Tons of Oil Equivalents
V_{OC}	Open Circuit Voltage
β	Coefficient of deviation from monoexponential decay
ΔA	Differential absorption (excited state – ground state)
ΔV	Differential of Potential
ε	Molar extinction coefficient
η	Solar-to-electric energy Conversion Efficiency
$\langle \tau_{KWW} \rangle$	KWW mean relaxation time

General procedures

All reactions were performed under an inert nitrogen atmosphere in a flame- or oven-dried apparatus, using Schlenk techniques. Tetrahydrofuran was purified by distillation over metallic sodium in the presence of benzophenone, toluene was distilled over metallic sodium. Methanol, CH_2Cl_2, and N,N-dimethylformamide were dried by storing under nitrogen over 4 Å molecular sieves. All other chemicals employed were commercially available and used as received. Petroleum ether was the 40-60° C boiling fraction. Thin layer chromatography was carried out on aluminum-supported Merck 60 F254 plates; detection was carried out using UV light and permanganate solutions followed by heating. Flash column chromatography was performed using Merck Kieselgel 60 (300-400 mesh) as the stationary phase. ^1H-NMR spectra were recorded at 200 or 400 MHz, and ^{13}C-NMR{^1H} spectra were recorded at 50.3 or 100.6 MHz. Chemical shifts were referenced to the residual solvent peak ($CHCl_3$, δ 7.27 ppm for ^1H-NMR and δ 77.00 ppm for ^{13}C-NMR). FT-IR spectra were recorded in the range 4000 – 400 cm^{-1} with a 2 cm^{-1} resolution. ESI-MS spectra were obtained by direct injection of the sample solution, using a Thermo Scientific LCQ-FLEET instrument and are reported in the form *m/z*. HRMS spectra were measured using a Thermo Scientific LTQ Orbitrap (FT-MS) instrument.

For the preparation of gold colloidal solutions, all glassware was cleaned with aqua regia and rinsed with plentiful of water before use. Water used was always MilliQ grade (resistivity higher than 18 MΩ cm). All chemicals employed were commercially available, used as received and stored under nitrogen or as standard solutions. Absolute EtOH and *i*-PrOH were dried by storing under nitrogen over 4 Å molecular sieves. Centrifugations were carried out with PK121R centrifuge from ALC with A-M10 rotor. A syringe-pump system was used for slow addition of reactants over a long time. Sonication was performed at 10° C by means of ultrasonic horn Vibra Cell VC375 from Sonic & Material with a power of 150 watts. Homogenization of the slurries was performed with T18 digital ultra-turrax dispersers homogenizer from IKA at the speed of 20000 rpm. TEM images were recorded on carbon-copper grids and statistic sets of at least 30 images were used to determine the average dimensions. DLS measurements were carried out by means of Zetasizer Nano ZS90 from Malvern instruments. A DEC-248CE semi-automatic screen printer with a customized structure with 24 1 cm × 1 cm spots with 43-80 mesh was used to deposit the slurries in thin layers. UV-Vis spectra were recorded with a Shimadzu UV-2600 spectrophotometer equipped with integration sphere, in the range 850 – 300 nm with a 0.5 nm resolution.

TiO_2 films for the kinetic studies were prepared by doctor-blading technique on FTO (TEC-15) (Solaronix) substrates using commercially available TiO_2 paste (18-NR-T, Dyesol). Dye **D35** was purchased from Dyenamo, while dyes **N3** and $[(Ru(dcb)_3)Cl_2]$ were acquired from Solaronix; all dyes were used as received and stored as powders at 4° C under nitrogen. Electronic steady state spectra were recorded using a Varian Cary 50 Bio spectrometer. Single-wavelength transient spectroscopic measurements were performed using a Continuum Surelight II, Nd:YAG laser at 10 Hz repetition rate with a Continuum Surelight optical parameter oscillator, producing pulsed (ca. 8 ns fwhm) 425 nm excitation light. The power of the pulse was adjusted between 1 and 3 mW cm^{-2} depending on samples. Probe light was generated with a Quartz Tungsten Halogen lamp (Ushio) powered by a radiometric power supply (Newport). The wavelength of interest was selected by two Cornerstone 130 monochromators (Oriel Instruments). Data were collected using either a five-stage photomultiplier tube, PMT (Applied Photophysics), or a Costronics photodetector amplified by a Costronics Optical Transient Amplifier connected to a Tektronix TDS 2022 oscilloscope. The data were analyzed using the Igor Pro software from WaveMetrics.

Chapter 1

Introduction

1.1. The world's energy issue

In the last decade, the world has faced its greatest economic crisis since the World War II, however, the global energy consumption has grown at an average of 1.9% per year in the same period. (*Figure 1.1*) Nowadays, it reaches a value of almost 13.15 billions of tons of oil equivalents (toe) per year, which corresponds to an average rate of consumption of 17.5 TW (1 toe has a calorific energy of about 42 GJ).[1]

Even though renewables are about to reach a 10% overall share, fossil fuels still provide 86% of the global primary energy supply; indeed, we are consuming 1006 barrels of oil, 110352 cubic meters of natural gas and 183 tonnes of coal per second.[1] The main energy source continues to be oil, the majority of which (ca. 80%) is used to power the world transportation system, the remainder is used for heating and electricity, petrochemicals, asphalt, and lubricants, in order of decreasing importance.[2]

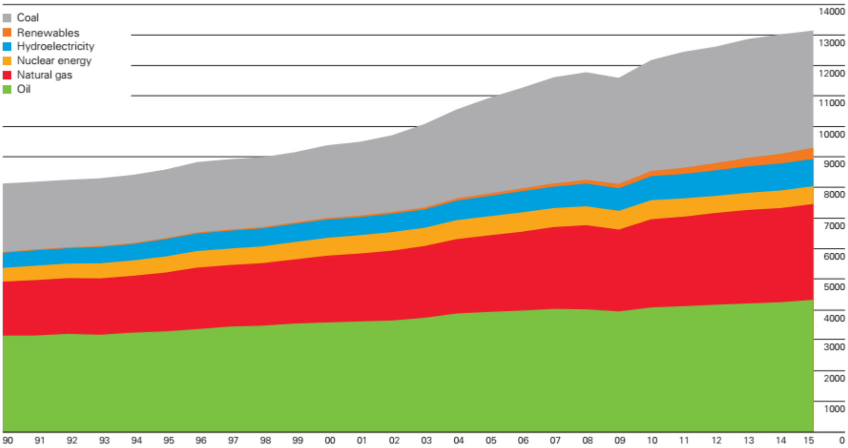

Figure 1. 1: ***World primary energy consumption*** *grew by a below-average 1.0% in 2015. All fuels except oil and nuclear power grew at below-average rates. Oil remains the world's dominant fuel but coal's market share fell to the lowest level since 2005. Renewables in power generation accounted for a record 2.8%. Consumptions for the last 15 years are here reported in million toe. Reproduced from ref*[1]

Anyway, fossil fuels are destinated to finish: the estimated reserves of coal are by far the largest among fossil fuels, as they might cover the present world demand for over 114 years, to be compared to 50.7 and 52.8 years for oil and natural gas, respectively.[1] While these deadlines are approaching, a radical shift from fossil fuels to renewable energies is more than desirable in the very next future. Although the rise of renewable energies is already taking place since several years, affecting primarily the electricity sector, the energy system is a gigantic and complex machine; therefore, this transition is expected to be a long, complicated and difficult process.[3]

1.1.1. Energy transition

In 2014, for the first time, global carbon emissions associated with energy production did not increase despite continued global energy consumption growth. This achievement is primarily attributed to the increasing penetration of renewables and enhanced energy efficiency, particularly in the affluent world.[4] Renewable energy sources in power generation continued to increase in 2015 accounting for 6.7% of global power generation;[1] the most affected sector is electricity production, (*Figure 1.2*) where approximately 23% of the overall world's generation is coming from renewable resources.[5] A rapid technological gain has supported strong growth in renewable energy, led by wind and solar power. These advances mean that all renewable energy technologies recorded solid growth in 2015. Their gain was at the expense of coal, which saw its largest fall on record, taking its share within primary energy to its lowest level since 2005.[1]

At the end of 2015, in the global scenario, hydroelectric capacity exceeded 1 TW, wind was 433 GW, and photovoltaic (PV) almost 230 GW; they covered 16.6, 3.7 and 1.2%, respectively, of the world electricity demand.[5] To better understand such shares one may recall that, while hydroelectricity has been an established technology for over 120 years, wind and PV were virtually non-existing just two decades ago.

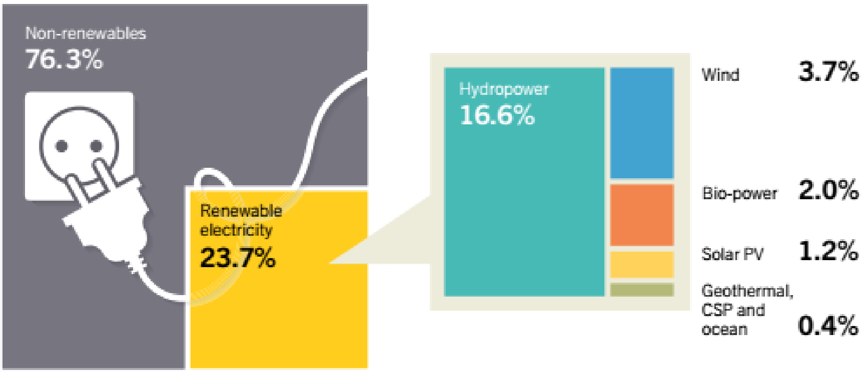

*Figure 1. 2: **Estimated renewable energy share of global Electricity production by the end of 2015**. Electricity is the kind of energy where renewables are employed the most. Consideration on how long the technologies were employed should be done when reading the shares of renewable sources. Reproduced from ref* [5]

The key player in this changing scenario is China, which already in 2014 produced as much electricity from water, wind, and sunlight, as all France and Germany's power plants combined, covering 20% of its demand.[6] The almost 7-fold drop of the PV module price in the last decade has also to be addressed to China where the production has increased 10-fold.[4]

One of the fastest growing sectors in renewables is PV: the number of areas where the price of PV has become competitive with conventional technologies is increasing and, in some industrialized countries, a remarkable portion of electricity production is already held by PV. In 2015, Italy produced almost 8% of its electricity consumption by PV, now the second largest share per capita in the word.[5]

Finally, it is of great relevance pointing out that a transition from fossil fuels to renewable energies needs to come with energy-saving policies too. The world population is expected to keep on growing and use energy-consuming technologies, therefore the consumption of the produced energy should be characterized by an increasing consciousness. A useful parameter to set a reasonable path for the energy consumption is the average annual per capita primary energy consumption of a given country. Such parameter can be correlated to many indicators that describe the quality of life of such country (human development index, infant mortality, average longevity, access to education and so forth).[7] From a comparison of such consumption parameter against the infant mortality (*Figure 1.3*), a rapid enhancement of life quality is registered with the increase of energy consumption until around 1.5 toe per year, this can be considered a critical energy consumption for a good quality live. On the other hand, this positive trend decelerates fast enough that consumptions higher than 3 toe per year result simply useless. In a planet with finite resources and an energy over-consumption, this crucial information should be taken into high consideration.

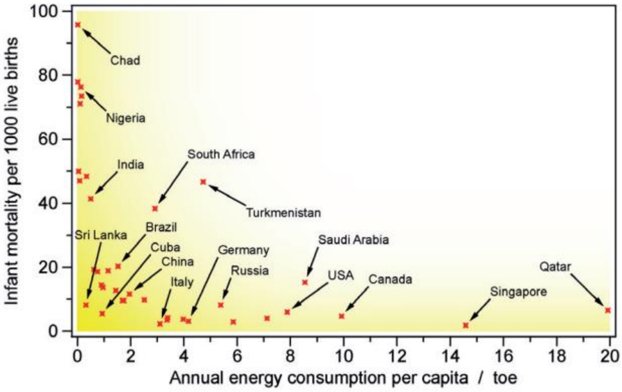

Figure 1. 3: ***Infant mortality versus per capita annual energy consumption of selected nations****. Increasing energy consumption until 1.5 toe, the life quality improves rapidly; instead, no significate infant mortality decrease is found for annual energy consumptions per capita higher than 3 toe. Reproduced from ref*[4]

1.2. The exploitation of Sunlight

Life requires energy and humanity does not make any exception to this rule, so that energy consumption can indeed be used as an indicator of the human quality of life and technological evolution. Sunlight has always been the primary source of energy for the whole of our planet: it is continuously converted in other kinds of energy and has been stored for thousands of years in fossil fuels. Sunlight is abundant: the Sun shines 90 PW on the Earth's surface; it will last for more than 4 billion years which makes it virtually an inexhaustible energy source, and finally is also fairly well distributed over the planet.[3]

The rate of energy consumption of our civilization (17.5 TW in 2015) is almost four orders of magnitude smaller than the solar energy irradiating the surface of the Earth. However, to make it useful for the humankind, solar energy needs to be converted into one of the final usable energy forms: heat, electricity, or fuels. While the conversion of light into heat is a straightforward process, the conversion in electricity and fuel can only be done through threshold processes that limit the overall conversion efficiency.[8]

The devices utilized to exploit sunlight energy are called solar panels. Among those, PV devices are the one capable of converting solar energy into electricity. The ways to obtain such conversion, and the materials that can perform it, can be different; PV installations may be ground-mounted, rooftop mounted or wall mounted, and each of those can be grid-connected or not, depending if the implant is connected to utility grid of electric power transmission of a certain area or has its own electricity accumulation system.

PV devices are capable of generating clean energy without producing any pollution during operation: however, considering the whole of their lifecycle, from raw materials purification to end-of-life disposal, the average environmental impact of PV devices is not negligible.[9] PV technology exhibits a series of remarkable merits also in the industrial field, such as the possibility to be scaled from the kW to the GW scale, both on-grid and off-grid, without affecting efficiency and economic performance (conventional fossil fuel and nuclear plants have an optimal operational size; below that or above that, they under-perform). One needs only an up-front investment which will be followed by decades of electricity produced by a 100% guaranteed free primary source with very low maintenance costs. Installation is possible on existing urban surfaces like roofs or walls with no land consumption, contributing to decentralization of the electricity production system. Not only is the decentralizations of electricity production needed to enhance energy security, but it also gives the possibility of providing electricity to communities in off-grid rural or isolated areas, improving the quality of life in underdeveloped regions.[4]

1.2.1. The dawn of photovoltaic: Silicon

The first established technology for sunlight exploitation is based on two consecutive slices (wafers) of semiconductor with opposite doping. (*Figure 1.4*) The semiconductor used is crystalline silicon: while growing a single crystal with 0.1% of a 3rd group element like Boron can be done to afford a p-doped Silicon wafer, on the other hand, the same amount of a 5th group element like Phosphorus provides an n-doped layer. At the interface between the two wafers a p–n junction is created, and the migration of the superficial charges provides a so-called "depletion zone". The electric field across this zone is known as insulating potential. Light beams hitting the device with an appropriate angle and energy can create a separation of charges in the depletion zone, producing a free electron and a free hole. The two charges migrate thanks to the insulating potential and accumulate on the corresponding doped semiconductor defining a differential of potential (ΔV).[10] Still, today over 90% of the commercial solar cells are based on these same materials and concepts developed at the Bell Laboratories in the early 1950s: light-induced charge separation at p–n junction between two wafers of doped silicon in either single-crystal or polycrystalline form (sc-Si and poly-Si, respectively).[11]

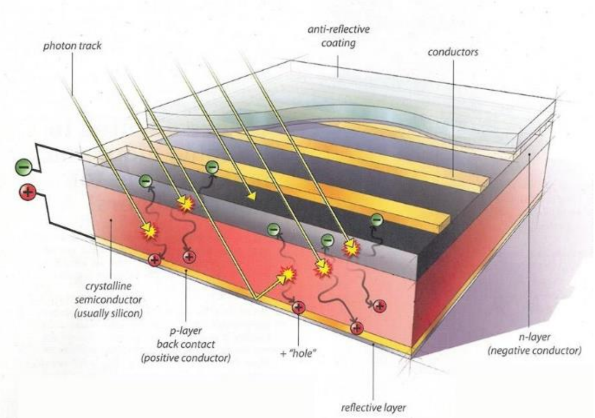

Figure 1. 4: ***Single-crystal silicon photovoltaic cell****: representation of a p-n junction. When light is absorbed by the semiconductor an electron-hole pair is created and migrate to the conductors thanks to an internal electric field.*

This promising technology is over 60-years old and deeply established; the lifetime of modules is in the decades time scale; efficiency of light-to-electricity conversion (the ratio between electric energy produced, and the radiating energy hitting the device; see below for further discussions) reaches 25.6 ± 0.5 % for cells made of single-crystal silicon;[12] cost reduction trajectories recall those of past disruptive technologies (e.g., the trends observed at the dawn of the automobile industry);[13] key materials (e.g., copper, silver, aluminum, plastics, silicon) are abundant, non-toxic and recyclable at end-life. Last but not least, silicon PV cumulative production will reach a TW scale within a decade, a landmark goal for future dominance not only in the PV but also in the entire electricity market.[14]

Even if Silicon is widely abundant and non-toxic, for PV application, a high purity degree is required and the production of a single crystal layer is a process that requires temperatures reached only with furnaces. Silicon has to undergo this kind of treatments both at the beginning of its life cycle and at the end of it to be recycled. This has an effective impact on production cost that is the highest among all the PV technologies;[15] using a polycrystalline material such cost can be reduced while efficiency remains fairly good: 21.3 ± 0.4 %.[12] Moreover, silicon PV devices have strict installation requirements: to be effective, solar radiation needs to hit the p-n junction with a specific inclination and therefore moving supports are often used; silicon panels are built up assembling typically 60 single Si wafers together, each of them 100-500 μm thick in photoactive compound, the final device turns out to be quite heavy (16 kg/m^2) and completely opaque. This is the reason why such technology is mostly employed for rooftop or on-land application.

1.2.2. Thin film technology as evolution of crystalline Silicon

Thin film solar cells are a more recent technology whose industrial exploitation has also grown in the past few years, but at a much lower rate.[4] This kind of devices recalls the working principle of sc-Si and poly-Si PV but the photoactive p-n junction of Si is replaced by thin layers of doped amorphous silicon (a-Si) or cadmium sulfide in combination with cadmium telluride (CdTe) or copper gallium indium selenide (CIGS). (*Figure 1.5*) In both cases, CdS acts as electron acceptor mimicking the n layer in the heterojunction. Also in this case, at the interface with CdTe or CIGS, a p-n junction is formed, where charge separation can occur in the case of photoexcitation.

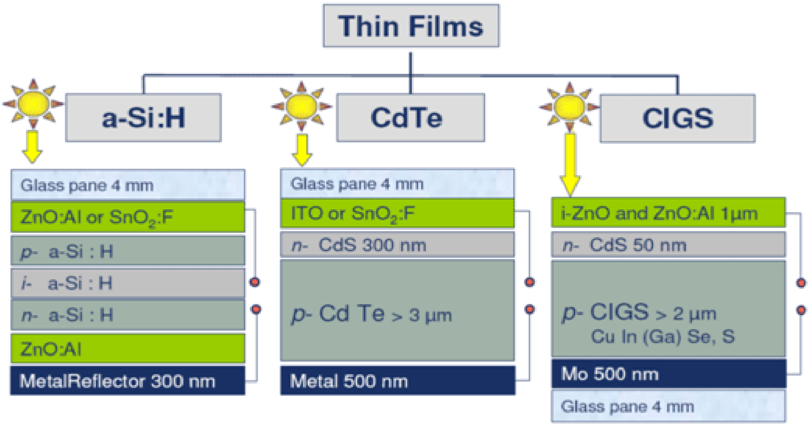

*Figure 1. 5: **Thin film PV**: classification and schematic composition of tree type of cells.*

The technology is named after the possibility of growing such semiconductors in thinner layers than the sc-Si one, ranging from 5 to 10 µm, making cells much lighter, bendable and therefore applicable also to portable devices. In the case of a-Si, the production costs are much lower since there is no more need for growing a single-crystal structure, but the yields of energy conversion are much lower too: about 10.2 ± 0.3%.[12] As far as CdTe and CIGS are concerned the deposition of photoactive compounds for the production of modules is possible by “roll to roll” process. Again, the production costs are lower reaching 1 $/WP for CdTe, and also the conversion efficiencies of CdTe PV devices are competitive to the crystalline Si PV being 21.0 ± 0.6%,[12] this is due to the band-gab of this p-n junction that fits very well with the average energy of the solar radiation.[16]

A critical issue for this technology is the availability of materials to enable PV deployment on the multi-TW scale. While Silicon is the second most abundant and evenly distributed element on earth’s crust having no risk of shortage, In, Ga, Se, Te, and Cd exhibit a much lower abundance. Even considering sc-Si PV providing the complete electricity supply by 2030, this would require a growth in the sc-Si production rates comparable to that of the last decades. On the other hand, the world reserves of In and Te wouldn’t be able to support not even a 8% world electricity supply, and the historical production trends should be largely exceeded to reach such energy coverage.[17] This is virtually impossible since In, Ga, Se, Te, and Cd are obtained just as byproducts of the extraction of other elements such as Cu, Zn, and Al.[18] Moreover, most of the compounds mentioned above are toxic and require special procedures for their disposal at end-life; therefore, the only way to make thin-film inorganic materials become true competitors of silicon-based technologies in a multi-TW PV market, are new formulations based on more abundant elements.[19] Still, they should be able to replicate, or even surpass, CdTe in terms of low manufacturing costs and high efficiency.

1.2.3. EROI and EPBT as comparison tools

When comparing different technologies for the exploitation of a common energy source, one has to deal with the concept that usable energy has an energy cost. This energy cost is not related to the conversion efficiency from the original form of energy to a more useful one, but to the energy required to build and maintain operative the infrastructure needed for its extraction, exploitation, stock and transportation. This concept is typically quantified by using the EROI index (energy return on investment)[20] which is equal to the ratio between the energy gained and the energy required to get that energy available. The higher the EROI value, the more fruitful the energy source. When EROI approaches values equal to or lower than one, the energy source becomes an "energy sink". For example, EROI can be used to estimate the "energy break-even point" of fuel extraction considering not only the energy to find or produce it but also the energy needed to carry it to the point of use and the energy needed to maintain the entire infrastructure active. For solar energy, the EROI refers to the energy produced by and invested in the converting device only (e.g., the photovoltaic modules) since the system has almost no maintenance costs. While the average fossil fuels EROI is decreasing over time because the most available fields were exhausted first, for renewable energies, the EROI tends to increase over time because of technological improvement. Recent estimations of the EROI of PV systems on the market are quite positive: 8.7 (sc-Si), 11.6 (poly-Si), 14.5 (a-Si), 19.9 (CIGS), 34.2 (CdTe), under the assumption of a 30-years system lifetime.[15]

Another important parameter is the energy payback time (EPBT), that is the period required for an energy production system to generate the same amount of energy that was used to make it. In principle, this parameter is related to EROI by the equation EPBT = lifetime/EROI. The EPBT for PV turns out to be 4.1 (sc-Si), 3.1 (poly-Si), 2.3 (a-Si), 1.7 (CIGS) and 1.0 (CdTe) years, which are remarkable values for devices operating for three decades.[15]

1.2.4. A greener solution to PV demand: Dye Sensitized Solar Cells (DSSC)

DSSC technology was introduced by O'Regan and Grätzel in 1991,[21] and is based on a completely different mechanism of electric current generation which is inspired from photosynthesis. (*Figure 1.6*) The photoactive compound is a colored molecule, whose structure has been intensively investigated passing from Ruthenium complexes to nature-inspired polyaromatic compounds or artificial metal-free scaffolds.[22] Such dye is the central core of this system and generates a separation of charges upon light irradiation. A thin semi-opaque semiconducting layer, generally made of nanocrystalline titanium dioxide, is supporting the dye and collecting the electrons, while a redox couple transports the formal holes to the cathode.[22,23]

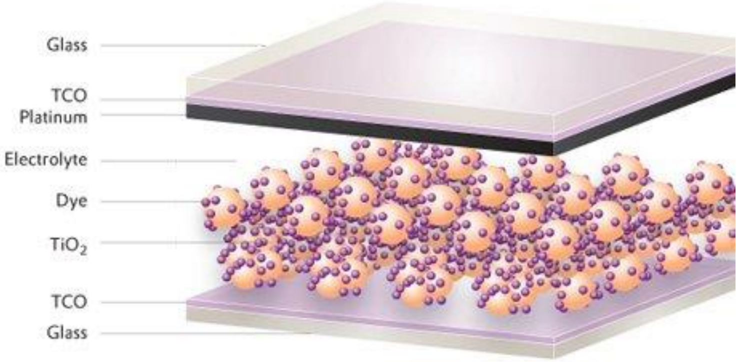

*Figure 1. 6: **Dye-Sensitized Solar Cell (DSSC)**: schematic representation of a PV device where the dye molecules are adsorbed on the nanocrystalline titanium dioxide particles. The cell filled with electrolyte is kept together by means of two conductive glasses acting as electrodes.*

Such architecture gives the module some special properties such as transparency and the possibility to be built with a wide variety of different colorations; moreover, unlike a p-n junction, that requires a specific inclination and intensity of light to perform charge separation, dye molecules can absorb light from any direction and even in low irradiance conditions.

When metal-free organic compounds are used as sensitizers, remarkable features can be highlighted, starting from the broad and wide availability of all the components. Thus, DSSCs require low quantity and quality of raw materials, that are also completely non-toxic, and can be manufactured at smaller economic and energetic costs.[9] Nowadays the highest efficiency certificated for DSSC sensitized with organic dyes is 11.9 ± 0.4% (for a 1 cm^2 cell under AM1.5 irradiation at 25° C) but when submodules are concerned the efficiencies decrease to maximum 8.8 ± 0.3% (26 serial cells reaching almost 400 cm^2 of surface irradiated with AM1.5 at 25° C).[12] However, even if DSSC efficiencies are still not comparable to those of sc-Si PV, the former should be considered as a relatively new technology having some improvement margin [24] while the last is a well-established one that is already facing its limits.[25] Moreover, compared to the established technologies discussed in the previous section, DSSC have the advantage to be easily integrable in buildings (not only on rooftops, but also in windows and facades) since they are transparent, and ensure good performances in non-standard illumination and temperature conditions as well, being able to exploit also indoor diffuse light. Nonetheless, they are still not competitive on efficiency and, most remarkably, lifetime, which is a formidable barrier for their widespread market diffusion.[4]

1.2.5. The new-come Perovskites

With the name of perovskites, a wide class of minerals is meant, all exhibiting a common crystal structure and the general formula ABX_3 (where A and B are two cations of different size and X is an anion that binds to both). Perovskites utilized in PV are synthetic hybrid organic–inorganic formyl-, methyl-, or ethyl-ammonium lead halide materials[26] of general formula RNH_3PbX_3 (in which X is I, Br or Cl), which were first utilized for solar applications in 2009.[27]

2012 Was a landmark year for perovskite solar cells that suddenly overcame 10% efficiencies. [28,29] In those devices the perovskite material was used as the light harvester, while the cell structure was similar to that of DSSCs: (*Figure 1.7*) a 500 nm thick mesoporous n-type TiO_2 layer sensitized with methyl-ammonium trihalogen plumbates acting as light-absorbing material. On top of the light-harvesting layer, a redox active medium was spin-coated, that in this case happened to be a *spiro*-OMe-TAD solid hole conductor. Nowadays the Perovskites based technology has evolved further in Meso-Superstructured Solar Cell (MSSC) where the TiO_2 is replaced with Al_2O_3, whose role is no more of electron collection and transport, but merely to act as a mesoporous scaffold, a superstructure upon which the photoactive layer is coated.[30]

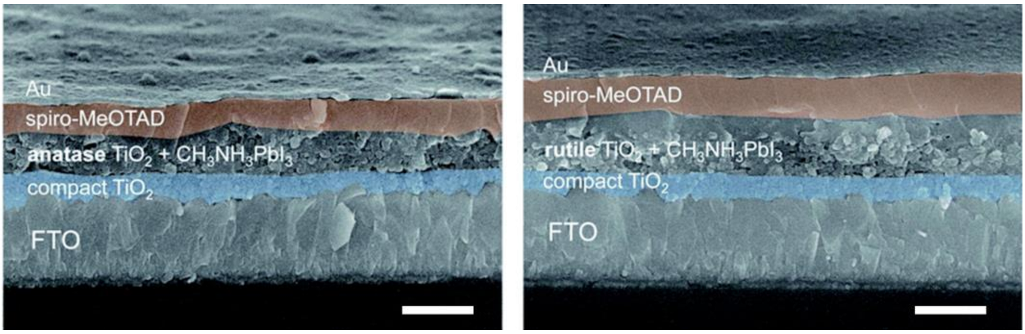

Figure 1. 7: ***SEM image of solid Perovskite solar cells****: pictures of films with perovskites supported on titanium dioxide with different crystalline structure, Left: anatase, right: rutile. Scale bars are 500 nm long.*

These all-solid-state devices can be made with a very standard lab equipment, simple chemicals, and easy fabrication protocol,[31] causing the research in this field to progress very quickly. At present, the certified record efficiency for a perovskite PV cell is 15 ± 0.6%[12] (for a 1 cm^2 cell under AM1.5 irradiation at 25° C), but notable exceptions overcoming 20% efficiency[32] for small-scale devices have been reported, an impressive achievement considering that these devices were non-existent one decade ago. The Shockley-Queisser limit is set at 30% for Perovskite cells[33] and, noteworthy, the EPBT has been recently estimated to be 2–3 months: the lowest among PV technologies.[31] Such quick progress, the high efficiencies, and the low EPBT could convince that perovskites will be the best option for lightweight, transparent, easy-to-manufacture solar devices suitable for building integration, however, perovskite-based PV cells are still very far from commercialization.

Despite the huge efforts made to find an alternative,[34] ammonium lead halide is still the unique class of compounds giving such performances. Unfortunately, while its solubility makes such compounds excellent for facile device fabrication, on the other hand, they require the device to be rigorously kept away from moisture, substantially enhancing sealing requirements. Moreover, its perfect crystallinity can be lost at temperatures typically experienced inside solar panels under intensive irradiation vanishing the efficiency and, finally, upon dissolution, PbI_2, a carcinogen compound, is generated.

1.3. Dye-Sensitized Solar Cells

Among all the PV technologies presented above, the research I carried out during my Ph.D. was focused on DSSC sensitized with purely organic dyes (from now simply referred as DSSC). Such choice was done in light of some advantages characterizing this technology such as the low environmental impact of this type of PV devices: as already highlighted, DSSCs are characterized by a low manufacturing and purification requirements, non-toxic components, low quantity of active material, easy recycling processes, and no release of harmful components. None of the other technologies fulfills all these ecological requirements. Despite the DSSCs have poor efficiency, that can be enhanced by engineering a better system, there the eco-friendly properties are intrinsically linked to the components of the device, and it has been shown that the other technologies could have poor margins of improvement in this field.

1.3.1. How a DSSC is made

Having a closer look at the architecture of a DSSC, one can recognize a multicomponent system isolated from the environment by two conductive glass sheets sealed together. (*Figure 1.8*) Indeed, the sides of these glass sheets facing the inside the cell are conductive thanks to deposition of a thin film of Fluorine doped Tin oxide (FTO), that allows charge collection. One of this two FTO glasses is covered with a thin film of semiconducting oxide. The most utilized material for the fabrication of this electron-collecting photo-electrode is a mesoporous nanocrystalline TiO_2 coated on one or more layers over the conducting film, reaching a thickness ranging from a few microns up to around 15 microns, depending on the final transparency desired. The mesoscopic film has an active surface area around three orders of magnitude larger than the flat surface[35] and it possesses DSSC-suitable properties in terms of energy levels and electron mobility, especially in its anatase state.[36] The TiO_2 conduction band (CB) lies between -0.4 and -0.5 V vs. NHE, making this material insulating in resting condition, but allowing charge conduction when electrons are energetic enough: such behavior makes TiO_2 a semiconductor. Absorption of the visible solar spectrum is obtained through a dye photosensitizer anchored to the nanocrystalline TiO_2 which, due to the high surface area, guarantees photoexcitation of a large number of molecules and high photocurrents. The chemical nature of the dye can vary a lot and, even if the amount of it loaded on a DSSC is really low (about 1 g/m^2),[37] we can say without any doubt that it is the central core of a DSSC. The connection of the previously described photo-anode with the cathode is ensured by an electrolyte solution. Such medium is usually an iodide/triiodide (I^-/I_3^-) redox couple dissolved in a liquid organic solvent, although attention is increasingly focusing on alternative solvents, including ionic liquids (ILs), as well as gelled electrolytes, polymer electrolytes, and water-based electrolytes.[38] Finally, to catalyze the charge transfer, a thin transparent film of Platinum is spread on the conducting surface of the FTO glass acting as the cathode.

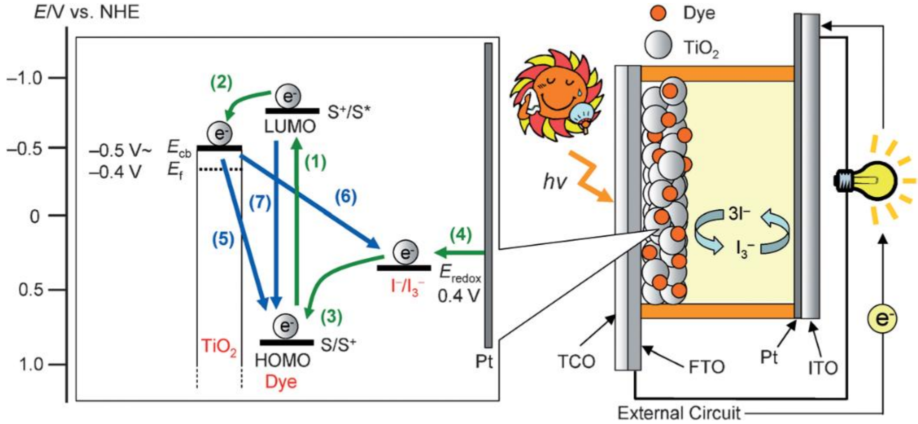

*Figure 1. 8: Right**: Schematic composition of a DSSC**. The main components of a cell, the TiO_2 substrate, the dye, and the electrolyte are represented. Left: **Schematic representation of the electronic transitions occurring in a DSSC**. The name and the reactions relative to the transitions are listed above. Reproduced from ref.*[22]

DSSC modules (*Figure 1.9*) are obtained by placing a number of cells on a common substrate and interconnecting them together.[39] Single cells are shaped as long rectangular stripes (with widths ranging from few mm to 1 cm),[40] where electrons are collected along the longer dimension, this way the path that the electrons have to follow to reach the collector is reduced and the current losses occurring along this path are reduced too. Current collecting fingers can be connected in series to increase module voltage or in parallel, scaling the current output of the module.

*Figure 1. 9: **Example of a DSSC module.***

1.3.2. How a DSSC works

Photoexcitation (*Eq. 1.1*) of the sensitizer results in the transition of one electron of the dye from the ground state to an excited state (occurring in a 0.1 ps to ns time scale). If the photosensitizer is characterized by a high electron density localized in proximity of the semiconductor and by a LUMO energy higher than that of the conduction band edge of TiO_2, injection of the electrons into the TiO_2 conduction band can occur. Since the dye is adsorbed on TiO_2 as a monolayer, there is no requirement for exciton diffusion to the dye/metal oxide interface and *injection* (*Eq. 1.2*) into the semiconductor can occur in a straightforward way. Such fast injection (circa 100 ps) avoids the non-radiative *quench* (*Eq. 1.7*) of excited states (ns timescale) which is often associated with thicker molecular films or dye-dye interaction.

Thus, photoexcitation of the dye results in electron injection of one electron in TiO_2. The acceptor state of the semiconductor is an extension of a bulk CB to the surface. Such extension is a region of injection where the surface interactions shape a decreasing potential profile.[41] Accumulation of electrons generates a local field of potential that drives the electrons to the FTO collecting surface. The high surface area of such mesoporous films could, however, have a significant downside, as it also promotes interfacial *charge recombination* (*Eq. 1.6*) losses (ms to s timescale) as it facilitates the contact with the redox mediator too.

The injection of an excited electron into the CB of the semiconducting oxide generates the oxidized form of the dye, the ground state of which is subsequently restored by electron donation from the electrolyte; this step is often referred to as the *regeneration* (*Eq. 1.3*) reaction (circa μs). Regeneration of the sensitizer hampers the *recombination* (*Eq. 1.5*) of the injected electron with the oxidized dye (μs to ms). The redox mediator is in turn regenerated by the *cathodic reduction* (*Eq. 1.4*) at the counter electrode, with the electrical circuit being closed.[42]

Photoexcitation	$S(TiO_2) + h\nu \rightarrow S^*(TiO_2)$	*Eq. 1.1*
Injection	$S^*(TiO_2) \rightarrow S^+(TiO_2) + e^-(TiO_2)$	*Eq. 1.2*
Regeneration	$2\ S^+(TiO_2) + 3\ I^- \rightarrow S(TiO_2) + I_3^-$	*Eq. 1.3*
Cathodic reduction	$I_3^- + 2\ e^-(Pt) \rightarrow 3\ I^-$	*Eq. 1.4*
Recombination	$S^+(TiO_2) + e^-(TiO_2) \rightarrow S(TiO_2)$	*Eq. 1.5*
Charge recombination	$I_3^- + 2\ e^-(TiO_2) \rightarrow 3\ I^-$	*Eq. 1.6*
Quench	$S^*(TiO_2) \rightarrow S(TiO_2)$	*Eq. 1.7*

1.3.3. DSSC characterization

The solar emission spectrum can be compared to that of a black body at the temperature of 5760 K. Sun shines light with wavelength ranging from UV to IR with a maximum in the visible region. The spectrum reaching the sea level of our planet is slightly modified in intensity and shape because of reflection, diffraction, and adsorption due to atmospheric molecules. (*Figure 1.10*) The effects of all these phenomena are generally quantified with a parameter called air mass (AM) that depend on the direct optical path length through the Earth's atmosphere. Such length is expressed as a ratio relative to the path length vertically upwards therefore can be approximated to the reverse of the cosine of the angle of the incident light, i.e., when the sunlight hits the earth surface perpendicularly we have the lowest energy loss and the spectrum is called AM1, while at sunset it will be AM38.[43]

Generally, for solar cell characterization, a simulated sun spectrum AM1.5 is used, whose intensity is normalized so that the density of output power is 100 mW/cm^2. The performances of DSSC are usually characterized measuring the six parameters reported below.

1.3.3.1. Incident Photon-to-current Conversion Efficiency (IPCE)

It is the ratio between the number of electrons determining the current in the external circuit and the number of photons of a certain wavelength that hit the solar photoactive surface. (*Eq. 1.8*)

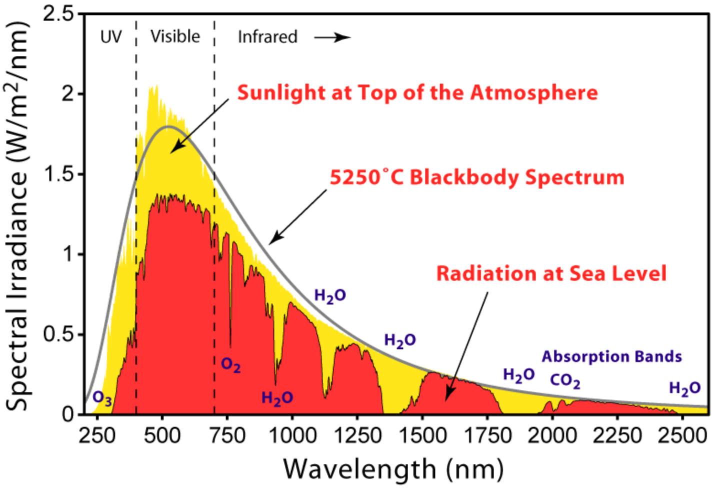

*Figure 1. 10: **Solar emission spectrum** with absorption band due to the atmosphere.*

$$IPCE[\%] = 1240[V\ nm]\frac{J_{ph}(\lambda)[mA\ cm^{-2}]}{\lambda[\mathrm{nm}]\ I(\lambda)[mW\ cm^{-2}]} \qquad \textit{Eq. 1.8}$$

Where $J_{ph}(\lambda)$ is the density of photocurrent generated from a monochromatic radiation with a wavelength λ and $I(\lambda)$ is the power density of such monochromatic radiation. The constant 1240 V nm is a numerical factor, which takes into account the conversion from density of current to number of electrons and from intensity of light to number of photons.

The IPCE spectrum is the graphic representation of IPCE values with respect to different λ and it is strictly correlated to the absorbance of the dye, the amount of dye loaded on TiO_2, the efficiency of injection and the charge collection efficiency of the circuit. In DSSC the IPCE value is hampered also by reflection and absorption of the covering glass, setting the theoretical maximum to 80-85%.[22]

1.3.3.2. Open Circuit Voltage (V_{OC})

It represents the ΔV between the photoanode and the cathode when the electronic circuit is open and the solar cell is shined with light. This is the maximum voltage that the solar cell can generate and reflects the maximum energy that can be extracted from any absorbed photon. The maximum theoretical value can be estimated as the difference between the semiconductor potential of the CB (Fermi level) and the electrochemical potential of the redox couple. Since the CB of TiO_2 lies between -0.4 and -0.5V vs. NHE, and the standard redox potential of I^-/I_3^- is 0.4 V vs. NHE, the maximum V_{OC} for a DSSC using that redox couple can be estimated to be around 0.8 – 0.9 V.[22]

Generally, the "loss-in-potential" in a solar cell can be calculated as the difference between the lowest-energy absorbed photon that can contribute to free carrier generation, determined from the onset of the IPCE spectrum, and the V_{OC} under full sunlight.[24] Due to thermodynamic constraints, the minimum loss in potential is in the order of 250–300 mV, following the Shockley–Queisser treatment[8] but is much higher in DSSC, since overpotentials (few hundreds of mV) are needed between the LUMO level of the dye and the CB of TiO_2 to promote electron injection, and between the redox potential of the electrolyte and the HOMO of the dye to ensure fast regeneration.[44] Other drops in potential are due to undesired phenomena occurring within the cell, such as recombination (with the dye *Eq. 1.5*) and charge recombination (*Eq. 1.6*) affecting also the photocurrent. Finally, semiconductor surface interactions with the electrolyte and the dye trigger the shift of the TiO_2 CB, affecting the V_{OC}. (*Figure 1.11*) This is the case of adsorbed injecting dyes having a dipole oriented toward the solution, which generates a displacement of the Fermi level (E_F) towards more negative potential, increasing the V_{OC}. Conversely, cations adsorbed on the surface of the semiconductor move downwards the potential, and this strategy is generally applied to enhance the overpotential of injection. Obviously, the V_{OC} can be tuned also changing the redox couple: for instance electrolyte based on Co^{+2}/Co^{+3}, with a redox potential of 0.5 V vs. NHE, can be employed but in this case, the efficiency of regeneration of the dye has to be verified.[45]

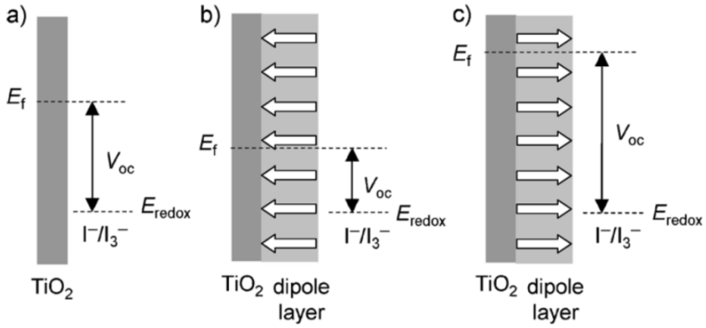

Figure 1. 11: ***Shift of the Fermi level of the semiconductor****. a) Potentials of the semiconductor and the electrolyte without considering interfacial interactions. b) Decrease of the* E_F *due to adsorption of a dipole orientate towards the surface e.i. cations adsorption. The* V_{OC} *decreases. c) Enhancement of the* E_F *due to dipole orientated toward the solutions e.i. injecting dyes adsorbed. The* V_{OC} *increase. Reproduced from ref.*[46]

1.3.3.3. Short circuit density of current (J_{SC})

This is the highest value of photocurrent produced by a cell, and it is measured at short circuit under irradiation. It is expressed as a density since the produced current is strictly dependent upon the illuminated photoactive surface. J_{SC} is related to the light harvesting properties of the dye: broad spectrum and high molar coefficient of absorption ensure a massive excitation of the dye. Thus the efficiency of injection of the excited dye in the semiconductor, and the speed of regeneration by the redox media play their role in avoiding quench and recombination respectively. Since the J_{SC} is strongly dependent on the dye photophysical- and electrochemical properties, it is of great importance to design dyes with intense light absorption and efficient electronic interaction with the TiO_2 CB.

The J_{SC}, as well as the V_{OC}, can be obtained by plotting the photocurrent produced by a solar cell versus the potential applied while illuminating it. The intercepts of the curve with the axis are the desired values and the product of each correlated J and V reveals the output power at each voltage. In *Figure 1.12* the couple of J and V giving the maximum power is reported.

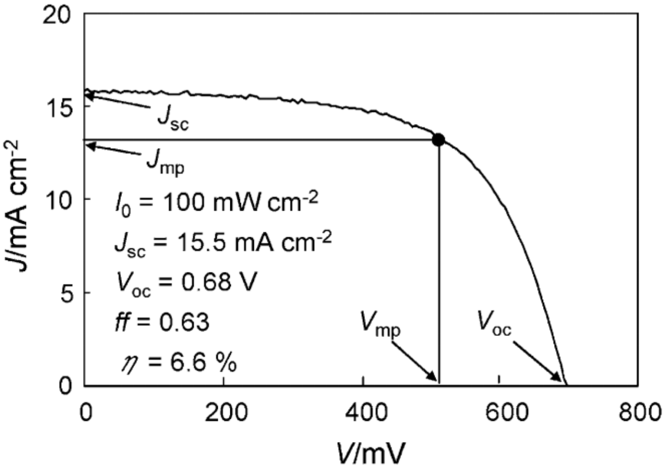

Figure 1. 12: ***J/V plot of a DSSC****. J_{SC} and V_{OC} can be extracted directly from the graphic where the curve meets the axis. The power of the device can be calculated for couple of J_{SC} and V_{OC}, the black spot represents the couple giving the maximum power of the device. Reproduced from ref.*[22]

1.3.3.4. Fill factor (*ff*)

Since the maximum power gained from a cell is not the product of the maximum current and voltage, this parameter expresses how close the actual cell is to an ideal behavior. (*Eq. 1.9*)

$$ff = \frac{J_{mp}\,V_{mp}}{J_{SC}\,V_{OC}} \tag*{Eq. 1.9}$$

The maximum value for *ff* is therefore 1 and it would be reached if the J/V curve (*Figure 1.12*) was a rectangle. Values lower than 1 of fill factor have to be related to electric resistances into the cell circuit, like the one affecting the ionic transport in the redox media and the one arising at the cathode interface, or to losses of generated charges, due to recombination or charge recombination. The first one affects the horizontal part of the curve (high J values) making it sweeper, while the second affect the vertical one (high V values) flattening it. From the interpretation of the J/V curve shape and the *ff* value, good insight can be obtained concerning cells' dysfunctions.

1.3.3.5. Solar-to-electric energy Conversion Efficiency (η)

This is the parameter generally used to evaluate the overall cell efficiency. It is calculated as the ratio between the maximum electric power emitted by the cell and the power of light source shining the cell. (*Eq. 1.10*)

$$\eta[\%] = \frac{J_{SC}[mA\ cm^{-2}]\ V_{OC}[V]\ ff}{I[mW\ cm^{-2}]} \qquad \textit{Eq. 1.10}$$

1.3.4. Stability

Together with efficiency and low costs, stability is one of the features building the "golden triangle" that a PV technology is required to fulfill to access the market. Stability is assessed by aging tests where the cell is irradiated with AM1.5 light at 100 mW/cm^2 while heating the sample at 60° C for at least 1000 h. Such harsh conditions are meant to accelerate the processes causing cell degradation. The key electric features explained above are recorded and plotted against exposition time to highlight losses in efficiency. The most common reason for cells loss of efficiency can be traced back to the photoactive compound, that might detach from the semiconductor or even directly decompose,[47] otherwise evaporation and leaching of the electrolyte solution can occur, especially if the solvent is volatile.

References

[1] BP. *BP Statistical Review of World Energy June 2016*. (**2016**).

[2] Vennestrøm P. N. R., Osmundsen C. M., Christensen C. H., Taarning E. Beyond petrochemicals: The renewable chemicals industry. *Angew. Chemie - Int. Ed.* **2011**, *50*, 10502–10509.

[3] Armaroli N., Balzani V. *Energy for a Sustainable World: From the Oil Age to a Sun-Powered Future*. *Energy for a Sustainable World: From the Oil Age to a Sun-Powered Future* (Wiley-VCH, **2010**).

[4] Armaroli N., Balzani V. Solar Electricity and Solar Fuels: Status and Perspectives in the Context of the Energy Transition. *Chem. - A Eur. J.* **2016**, *22*, 32–57.

[5] Seyboth K., Sverrisson F., Appavou F., Brown A., Epp B., Leidreiter A., Lins C., Musolino E., Murdock H. E., Petrichenko K., Farrell T. C., Krader T. T., Tsakiris A., Sawin J. L., Skeen J., Sovacool B. *Renewables 2016 Global Status Report*. *Global Status Report* (**2016**).

[6] Mathews J. *Greening of Capitalism: How Asia is Driving the Next Great Transformation*. (Stanford University Press, **2014**).

[7] Smil V. *Energy in nature and society : general energetics of complex systems*. (MIT Press, **2008**).

[8] Shockley W., Queisser H. J. Detailed balance limit of efficiency of p-n junction solar cells. *J. Appl. Phys.* **1961**, *32*, 510–519.

[9] Parisi M. L., Maranghi S., Basosi R. The evolution of the dye sensitized solar cells from Grätzel prototype to up-scaled solar applications: A life cycle assessment approach. *Renew. Sustain. Energy Rev.* **2014**, *39*, 124–138.

[10] Wenham S. R., Green M. a. Silicon solar cells. *Prog. Photovolt. Res. Appl.* **1996**, *4*, 3–33.

[11] Blandford R., Watkins M. This Month in Physics History: April 25, 1954: Bell Labs Demonstrates the First Practical Silicon Solar Cell. *APS News* **2009**, *18*, 2.

[12] Green M. A., Emery K., Hishikawa Y., Warta W., Dunlop E. D. Solar cell efficiency tables (version 48). *Prog. Photovolt. Res. Appl.* **2016**, *24*, 905–913.

[13] Mathews J. A., Tan H. Economics: Manufacture renewables to build energy security. *Nature* **2014**, *513*, 166–168.

[14] Mayer J. N. N. N., Philipps S., Hussein N. S., Schiegi T., Senkpiel C. *Current and Future Cost of Photovoltaics*. *Agora Energiewende* (**2015**).

[15] Bhandari K. P., Collier J. M., Ellingson R. J., Apul D. S. Energy payback time (EPBT) and energy return on energy invested (EROI) of solar photovoltaic systems: A systematic review and meta-analysis. *Renew. Sustain. Energy Rev.* **2015**, *47*, 133–141.

[16] Fthenakis V. M. Life cycle impact analysis of cadmium in CdTe PV production. *Renew. Sustain. Energy Rev.* **2004**, *8*, 303–334.

[17] Kavlak G., McNerney J., Jaffe R. L., Trancik J. E. Metal production requirements for rapid photovoltaics deployment. *Energy Environ. Sci.* **2015**, *8*, 1651–1659.

[18] Peiró L. T., Méndez G. V., Ayres R. U. Material Flow Analysis of Scarce Metals: Sources,

Functions, End-Uses and Aspects for Future Supply. *Environ. Sci. Technol.* **2013**, *47*, 2939–2947.

[19] Wadia C., Alivisatos A. P., Kammen D. M. Materials Availability Expands the Opportunity for Large-Scale Photovoltaics Deployment. *Environ. Sci. Technol.* **2009**, *43*, 2072–2077.

[20] Murphy D. J., Hall C. A. S. Year in review-EROI or energy return on (energy) invested. *Ann. N. Y. Acad. Sci.* **2010**, *1185*, 102–118.

[21] O'Regan B., Grätzel M. A low-cost, high-efficiency solar cell based on dye-sensitized colloidal TiO_2 films. *Nature* **1991**, *353*, 737–740.

[22] Ooyama Y., Harima Y. Photophysical and electrochemical properties, and molecular structures of organic dyes for dye-sensitized solar cells. *ChemPhysChem* **2012**, *13*, 4032–4080.

[23] Hagfeldt A., Boschloo G., Sun L., Kloo L., Pettersson H. Dye-Sensitized Solar Cells. *Chem. Rev.* **2010**, *110*, 6595–6663.

[24] Snaith H. J. Estimating the maximum attainable efficiency in Dye-sensitized solar cells. *Adv. Funct. Mater.* **2010**, *20*, 13–19.

[25] Rühle S. Tabulated values of the Shockley-Queisser limit for single junction solar cells. *Sol. Energy* **2016**, *130*, 139–147.

[26] Saliba M., Matsui T., Domanski K., Seo J.-Y., Ummadisingu A., Zakeeruddin S. M., Correa-Baena J.-P., Tress W. R., Abate A., Hagfeldt A., Gratzel M. Incorporation of rubidium cations into perovskite solar cells improves photovoltaic performance. *Science (80-.).* **2016**, *354*, 206–209.

[27] Kojima A., Teshima K., Shirai Y., Miyasaka T. Organometal halide perovskites as visible-light sensitizers for photovoltaic cells. *J. Am. Chem. Soc.* **2009**, *131*, 6050–6051.

[28] Lee M. M., Teuscher J., Miyasaka T., Murakami T. N., Snaith H. J. Efficient hybrid solar cells based on meso-superstructured organometal halide perovskites. *Science* **2012**, *338*, 643–7.

[29] Kim H.-S., Lee C.-R., Im J.-H., Lee K.-B., Moehl T., Marchioro A., Moon S.-J., Humphry-Baker R., Yum J.-H., Moser J. E., Grätzel M., Park N.-G. Lead iodide perovskite sensitized all-solid-state submicron thin film mesoscopic solar cell with efficiency exceeding 9%. *Sci. Rep.* **2012**, *2*, 591.

[30] Snaith H. J. Perovskites: The Emergence of a New Era for Low-Cost, High-Efficiency Solar Cells. *J. Phys. Chem. Lett.* **2013**, *4*, 3623–3630.

[31] Gong J., Darling S., You F. Perovskite Photovoltaics: Life-Cycle Assessment of Energy and Environmental Impacts. *Energy Environ. Sci.* **2015**, *8*, 1953–1968.

[32] Yang W. S., Noh J. H., Jeon N. J., Kim Y. C., Ryu S., Seo J., Seok S. Il. High-performance photovoltaic perovskite layers fabricated through intramolecular exchange. *Science* **2015**, *348*, 1234–1237.

[33] Sha W. E. I., Ren X., Chen L., Choy W. C. H. The efficiency limit of $CH_3NH_3PbI_3$ perovskite solar cells. *Appl. Phys. Lett.* **2015**, *106*, 221104.

[34] Boix P. P., Agarwala S., Koh T. M., Mathews N., Mhaisalkar S. G. Perovskite solar cells: Beyond methylammonium lead iodide. *J. Phys. Chem. Lett.* **2015**, *6*, 898–907.

[35] Grätzel M. Mesoscopic Solar Cells for Electricity and Hydrogen Production from Sunlight. *Chem. Lett.* **2005**, *34*, 8–13.

[36] Park N.-G., van de Lagemaat J., Frank a J. Comparison of Dye-Sensitized Rutile- and Anatase-Based TiO_2 Solar Cells. *J. Phys. Chem. B* **2000**, *104*, 8989–8994.

[37] Dell'Orto E., Raimondo L., Sassella A., Abbotto A. Dye-sensitized solar cells: spectroscopic evaluation of dye loading on TiO_2. *J. Mater. Chem.* **2012**, *22*, 11364.

[38] Rahman M. Y. A., Ahmad A., Umar A. A., Taslim R., Su'ait M. S., Salleh M. M. Polymer electrolyte for photoelectrochemical cell and dye-sensitized solar cell: A brief review. *Ionics* **2014**, *20*, 1201–1205.

[39] Hashmi G., Miettunen K., Peltola T., Halme J., Asghar I., Aitola K., Toivola M., Lund P. Review of materials and manufacturing options for large area flexible dye solar cells. *Renewable and Sustainable Energy Reviews* **2011**, *15*, 3717–3732.

[40] Giordano F., Guidobaldi A., Petrolati E., Vesce L., Riccitelli R., Reale A., Brown T. M., Di Carlo A. Realization of high performance large area Z-series-interconnected opaque dye solar cell modules. *Prog. Photovolt. Res. Appl.* **2013**, *21*, 1653–1658.

[41] Beranek R. (Photo)electrochemical Methods for the Determination of the Band Edge Positions of TiO_2-Based Nanomaterials. *Adv. Phys. Chem.* **2011**, *2011*, Article ID 786759, 20 pages.

[42] Listorti A., O'Regan B., Durrant J. R. Electron Transfer Dynamics in Dye-Sensitized Solar Cells. *Chem. Mater.* **2011**, *23*, 3381–3399.

[43] Boxwell M. *Solar Electricity Handbook 2015 Edition*.(Greenstream Publishing Limited, **2015**).

[44] Grätzel M. Dye-sensitized solar cells. *J. Photochem. Photobiol. C Photochem. Rev.* **2003**, *4*, 145–153.

[45] Mosconi E., Yum J.-H., Kessler F., Gómez García C. J., Zuccaccia C., Cinti A., Nazeeruddin M. K., Grätzel M., De Angelis F. Cobalt Electrolyte/Dye Interactions in Dye-Sensitized Solar Cells: A Combined Computational and Experimental Study. *J. Am. Chem. Soc.* **2012**, *134*, 19438–19453.

[46] Ooyama Y., Harima Y. Molecular Designs and Syntheses of Organic Dyes for Dye-Sensitized Solar Cells. *European J. Org. Chem.* **2009**, *2009*, 2903–2934.

[47] Chen C., Yang X., Cheng M., Zhang F., Sun L. Degradation of cyanoacrylic acid-based organic sensitizers in dye-sensitized solar cells. *ChemSusChem* **2013**, *6*, 1270–1275.

Chapter 2

Aim of the work

During my Ph.D. I focused my work on the investigation of some of the components of the complex system of a DSSC. As described before, DSSCs are PV systems characterized by a considerable number of components,[1,2] each of them having its own role and principle of operation. Even more important is the fact that each component is influencing the others, creating an entanglement of photo-electrochemical systems whose cooperation determines the overall efficiency of the device.

Thus, reaching high efficiencies in a cell has not been the most important goal of this work. A great importance was attributed to aesthetic features such as color and transparency, but also to stability over long times, exploitation of new materials and above all, elucidation of mechanisms of interactions taking place at the interface between different DSSC components.

Aiming to develop a technology that could fit at the most with the concept of environmental sustainability, I mainly focused on the exploitation, development, characterization and use of metal-free dyes as sensitizers. This has been done by carrying out the design and synthesis of new dyes but also by engineering of the semiconductor substrate and the investigation of new electrolytes, in order to make them work efficiently in combination with organic sensitizers.

The main part of my research work was focused on the preparation and characterization of new sensitizers, which represent the central core of a DSSC. Among many existing categories of photoactive molecules that fit with this role in DSSC,[3,4] working with the MoRe research group headed by Dr. Mordini and Reginato at ICCOM-CMR in partnership with the University of Firenze, I carried out a research on two classes of innovative dyes characterized by a completely organic structure.

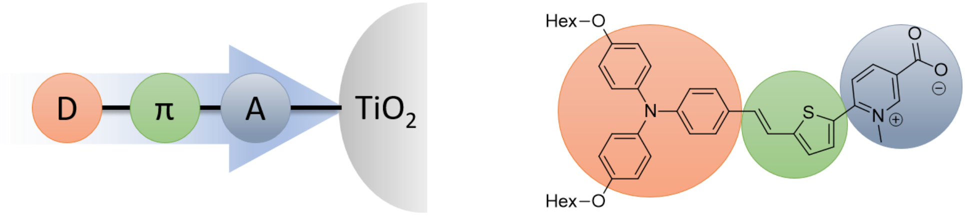

Figure 2. 1: Left: ***D-π-A design****: the acceptor moiety is responsible for both attracting the electron and anchoring the dye to the TiO_2 substrate. Right:* ***Representative carboxy pyridinium dye****, the D-π-A design is highlighted in the dye structure.*

The first one was represented by molecules with a specific design known as D-π-A.[5,6] The compounds of this type were characterized by an electron donor moiety (D) and an electron acceptor one (A) connected together by a conjugated system (π). The synthesized dyes were bearing a carboxy pyridinium as anchoring function.[7] (*Figure 2.1*) This part of the work had the specific purpose of boosting the performances of a set of dyes characterized by high stability,[8] that I developed during my master thesis period. The second group of compounds developed was instead based on a D-A-π-A structure.[9,10] (*Figure 2.2*) This second design can be seen as a D-π-A one where an additional electron withdrawing group (EWG) is inserted between the donor part and the conjugated bridge acting as an internal electron acceptor.

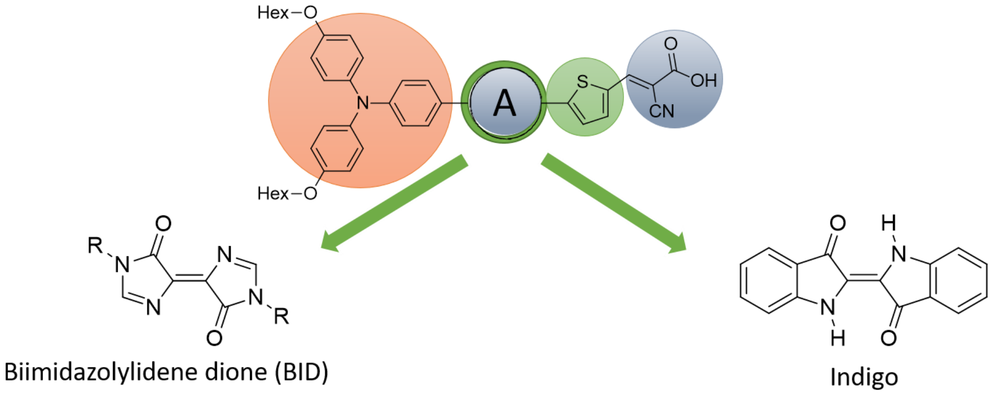

Figure 2. 2: ***D-A- π -A design****. An internal acceptor moiety was added between the donor and the conjugated bridge to obtain the D-A- π -A design. The electron poor heterocyclic scaffold investigated are reported.*

In this work, known electron poor compounds with remarkable light harvesting characteristics such us Indigo[11] and biimidazolylidene-dione[12] (BID) (*Figure 2.2*) were exploited to prepare new dyes by inserting them within the conjugated structure of the molecules. In the latter case, a special attention was given to the coloration of the final compounds. Together with transparency and lightness, the color of the devices represents a key feature for the exploitation of DSSC in building integrated PV. The aim of this class of compounds has been reaching colorations ranging from blue to green. Such colors are indeed almost missing among the libraries of DSSC dyes reported so far but at the same time are highly required by the market because of their added aesthetical value.

The second topic I have addressed in my work concerns the functionalization of DSSC semiconductor substrates with nanostructures. The efficiency enhancement due to the incorporation of metal nanoparticles (NPs) has been already demonstrated for Ru complexes-sensitized DSSCs with some outstanding results,[13,14] but the effectivity of such approach on DSSCs based on organic dyes has not been investigated so far. In this part of the research, I set up an analytical method based on solid state UV-Vis spectroscopy, to prove and evaluate the enhancement of absorption of a synthesized organic dyes adsorbed on solid thin films such as TiO_2 substrates doped with gold NPs. (*Figure 2.3*) In this thesis, I will address the problems concerning AuNPs compatibility with the DSSC environment, the formulation of the TiO_2 paste with nanocomposites, and finally the achievement of homogeneous samples and the determination of the dye loading on the solid substrate.

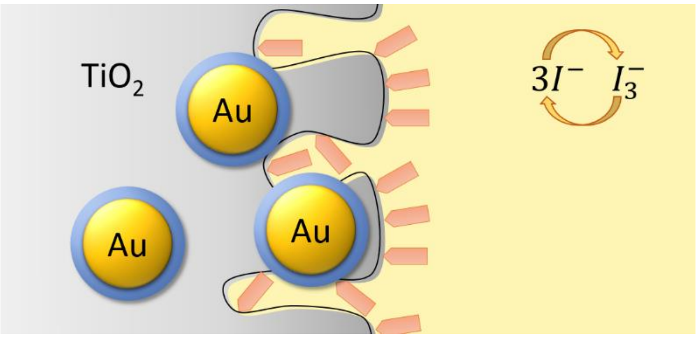

Figure 2. 3: ***Core-shell gold nanoparticles embedded in the semiconducting substrate****. Representation of the TiO_2 mesoporous layer (grey) sensitized with dye molecules (red). The semiconductor was doped with gold nanoparticles covered by an oxide shell (light blue).*

Another fundamental part of this work was related to the elucidation of the enhancement mechanism, for which AuNPs are responsible in DSSCs. To isolate and discriminate between two of the many reported hypotheses concerning how metal NPs affect DSSC operating principle,[13,15,16] two different core-shell systems were employed: gold-silica and gold-titania. These systems were chosen for assessing only electromagnetic interactions (*Figure 2.4*) between the dye and the NPs that were embedded in the photoanode support. Indeed, NPs are capable of enhancing the electromagnetic field in their surroundings, such phenomenon is known as near field enhancement.[17,18] Chromophores in the proximity of the NPs can experience an intensified electromagnetic field and absorb more light. (*Figure 2.4 C*) By spectroscopic investigation., it was possible to quantify such enhancement of dye absorption due to the interaction with the electromagnetic field produced by the nanoparticles in the TiO_2 films. The preparation of these systems required an intensive synthetic work which will be reported here although the obtained materials have been used for spectroscopic investigation only, and have not been used for applications in DSSC yet.

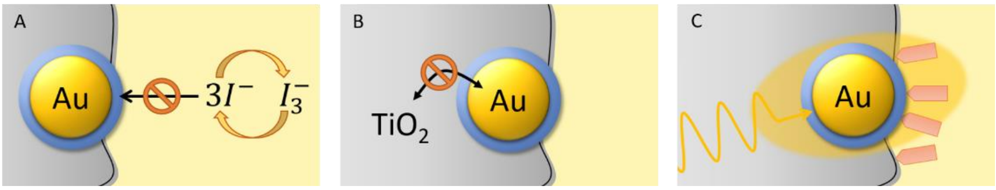

Figure 2. 4: A) ***Chemical insulation****: the shell prevent gold from being corroded by the electrolyte. B)* ***Electronic insulation****: any electron exchange between the metal and the semiconductor is avoided. C)* ***Electromagnetic interaction****: nanoparticles enhance the electromagnetic field in its surrounding, dyes in this region can experience such near field enhancement (NFE) effect with consequent absorption enhancement.*

The last section of this work is dedicated to the investigation of new materials for replacing the liquid electrolyte solution. During a period as Ph.D. visiting student at the Chalmers University of Technology (Gothenburg, SE) I had the chance to establish a collaboration with the Department of Chemistry and Chemical Engineering, to carry out a study concerning the exploitation of Ionic Liquids (ILs) as possible electrolyte media in DSSC.

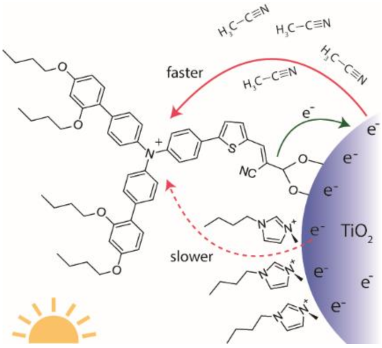

Figure 2. 5: ***Recombination kinetics with different electrolytes.*** *Ionic liquids cations were found to slow down the recombination processes probably due to electrosorption of a layer of cations compensating the injected electrons.*

As the more commonly used Lithium cations, the bulky organic cations were supposed to rearrange at the TiO_2–electrolyte interface and locally compensate the injected charge.[19] (*Figure 2.5*) This way the ILs would slow down the recombination processes and the electrolyte media evaporation would become negligible due to IL's high boiling point. To prove such theory, back electron-transfer rates for TiO_2 thin films sensitized with organic dyes were investigated using transient absorption spectroscopy.[20] The preparation of the samples was optimized and their homogeneity was assessed by preliminary electrochemical characterization. In this work great importance was given to the validation of the model proposed, therefore other measurements with reference dyes were carried out as a comparison. To ensure the applicability of ILs as redox electrolyte media in DSSCs the rate of regeneration in presence of redox couples was also tested.

References

[1] Grätzel M. Dye-sensitized solar cells. *J. Photochem. Photobiol. C Photochem. Rev.* **2003**, *4*, 145–153.

[2] Hagfeldt A., Boschloo G., Sun L., Kloo L., Pettersson H. Dye-Sensitized Solar Cells. *Chem. Rev.* **2010**, *110*, 6595–6663.

[3] Basheer B., Mathew D., George B. K., Reghunadhan Nair C. P. An overview on the spectrum of sensitizers: The heart of Dye Sensitized Solar Cells. *Sol. Energy* **2014**, *108*, 479–507.

[4] Ooyama Y., Harima Y. Photophysical and electrochemical properties, and molecular structures of organic dyes for dye-sensitized solar cells. *ChemPhysChem* **2012**, *13*, 4032–4080.

[5] Mishra A., Fischer M. K. R., Bäuerle P. Metal-Free Organic Dyes for Dye-Sensitized Solar Cells: From Structure: Property Relationships to Design Rules. *Angew. Chemie Int. Ed.* **2009**, *48*, 2474–2499.

[6] Yen Y.-S., Chou H.-H., Chen Y.-C., Hsu C.-Y., Lin J. T. Recent developments in molecule-based organic materials for dye-sensitized solar cells. *J. Mater. Chem.* **2012**, *22*, 8734.

[7] Franchi D., Calamante M., Reginato G., Zani L., Peruzzini M., Taddei M., Fabrizi De Biani F., Basosi R., Sinicropi A., Colonna D., Di Carlo A., Mordini A. Two New Dyes with Carboxypyridinium Regioisomers as Anchoring Groups for Dye-Sensitized Solar Cells. *Synlett* **2015**, *26*, 2389–2394.

[8] Franchi D., Calamante M., Reginato G., Zani L., Peruzzini M., Taddei M., Fabrizi De Biani F., Basosi R., Sinicropi A., Colonna D., Di Carlo A., Mordini A. A comparison of carboxypyridine isomers as sensitizers for dye-sensitized solar cells: assessment of device efficiency and stability. *Tetrahedron* **2014**, *70*, 6285–6295.

[9] Wu Y., Zhu W. Organic sensitizers from D-π-A to D-A-π-A: effect of the internal electron-withdrawing units on molecular absorption, energy levels and photovoltaic performances. *Chem. Soc. Rev.* **2013**, *42*, 2039–58.

[10] Wu Y., Zhu W. H., Zakeeruddin S. M., Grätzel M. Insight into D-A-π-A structured sensitizers: A promising route to highly efficient and stable dye-sensitized solar cells. *ACS Appl. Mater. Interfaces* **2015**, *7*, 9307–9318.

[11] Głowacki E. D., Voss G., Sariciftci N. S. 25th anniversary article: Progress in chemistry and applications of functional indigos for organic electronics. *Adv. Mater.* **2013**, *25*, 6783–6800.

[12] Wang J., Chen X., Cai Z., Luo H., Li Y., Liu Z., Zhang G., Zhang D. New alternating electron donor-acceptor conjugated polymers entailing (E)-[4,4′-biimidazolylidene]-5,5′(1H,1′H)-dione moieties. *Polym. Chem.* **2013**, *4*, 5283–5290.

[13] Sheehan S. W., Noh H., Brudvig G. W., Cao H., Schmuttenmaer C. A. Plasmonic Enhancement of Dye-Sensitized Solar Cells Using Core–Shell–Shell Nanostructures. *J. Phys. Chem. C* **2013**, *117*, 927–934.

[14] Brown M. D., Suteewong T., Kumar R. S. S., D’Innocenzo V., Petrozza A., Lee M. M., Wiesner U., Snaith H. J. Plasmonic dye-sensitized solar cells using core-shell metal-insulator nanoparticles. *Nano Lett.* **2011**, *11*, 438–445.

[15] Atwater H. A., Polman A. Plasmonics for improved photovoltaic devices. *Nat. Mater.* **2010**, *9*, 865–865.

[16] Kawawaki T., Takahashi Y., Tatsuma T. Enhancement of dye-sensitized photocurrents by gold nanoparticles: Effects of plasmon coupling. *J. Phys. Chem. C* **2013**, *117*, 5901–5907.

[17] Choi H., Chen W. T., Kamat P. V. Know thy nano neighbor. Plasmonic versus electron charging effects of metal nanoparticles in dye-sensitized solar cells. *ACS Nano* **2012**, *6*, 4418–4427.

[18] Qi J., Dang X., Hammond P. T., Belcher A. M. Highly Efficient Plasmon-Enhanced Dye-Sensitized Solar Cells through Metal@Oxide Core–Shell Nanostructure. *ACS Nano* **2011**, *5*, 7108–7116.

[19] Jennings J. R., Wang Q. Influence of Lithium Ion Concentration on Electron Injection, Transport, and Recombination in Dye-Sensitized Solar Cells. *J. Phys. Chem. C* **2010**, *114*, 1715–1724.

[20] Saavedra Becerril V., Franchi D., Abrahamsson M. Ionic Liquid-Induced Local Charge Compensation: Effects on Back Electron-Transfer Rates in Dye-Sensitized TiO_2 Thin Films. *J. Phys. Chem. C* **2016**, *120*, 20016–20023.

Chapter 3

DYES

Synthesis and characterization of new photoactive compounds

Franchi D., Calamante M., Reginato G., Zani L., Peruzzini M., Taddei M., Fabrizi De Biani F., Basosi R., Sinicropi A., Colonna D., Di Carlo A., Mordini A. A comparison of carboxypyridine isomers as sensitizers for dye- sensitized solar cells : assessment of device efficiency and stability. *Tetrahedron* **2014**, *70*, 6285–6295.

Franchi D., Calamante M., Reginato G., Zani L., Peruzzini M., Taddei M., Fabrizi De Biani F., Basosi R., Sinicropi A., Colonna D., Di Carlo A., Mordini A. Two New Dyes with Carboxypyridinium Regioisomers as Anchoring Groups for Dye-Sensitized Solar Cells. *Synlett* **2015**, *26*, 2389–2394.

3.1. Introduction and background

The photoactive dye is the key component of a DSSC: it is responsible for the first charge separations[1] and, to be effective in electricity generation, needs to possess some distinctive structural and electrochemical properties. The dye chemical structure has to be designed to concentrate the electron density of the excited levels (LUMO, lowest unoccupied molecular orbital) on the moiety anchored to the TiO_2 surface so that injection of such high energy electrons is favored. On the other hand, the HOMO (highest occupied molecular orbital) should be characterized by an electron density located far away from the semiconductor, exposed towards the redox mediator by means of which the regeneration of the dye takes place, so that recombination with the injected electrons is disfavored.[2,3] (*Figure 3.1 Left*) Other than the position of the anchoring moiety inside the molecule, the magnitude of the electronic coupling between dye and semiconductor plays an essential role in the injection process. This coupling is primarily determined by the spatial overlap between the LUMO orbital of the dye excited state and the conduction band states on the semiconductor. This wavefunction overlap is dependent both upon the distance of the dye LUMO orbital from the metal oxide surface, and the choice of the anchoring group.[1] Finally, the absolute position of the dye HOMO-LUMO gap needs to straddle the electrochemical potential of the regenerating redox couple and the TiO_2 conduction band (CB). (*Figure 3.1 Right*) This band gap must be large enough to provide also the needed few hundreds of mV of overpotential,[4] but still small enough to allow adsorption of a large portion of the solar spectrum.

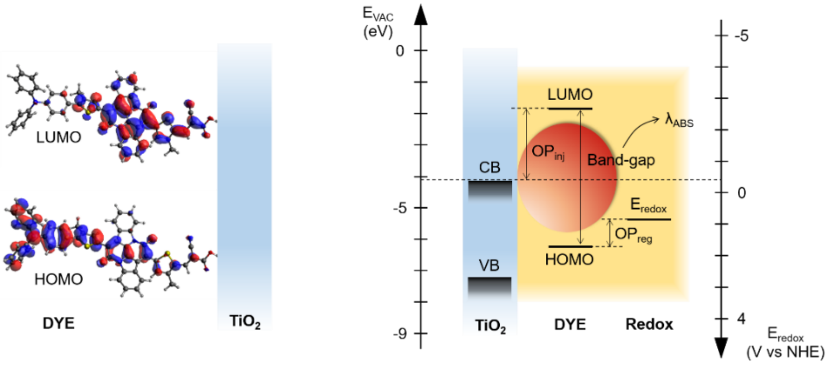

*Figure 3. 1: Left: **The electron density** of the LUMO is localized on the moiety of the dye molecule anchored to the semiconductor to promote electron injection. The HOMO one is more distant facilitating instead the dye regeneration. Right: **The position of the energy levels** of a dye straddle the potential of the redox couple and the TiO_2 CB. The overpotentials of injection (OP_{inj}) and regeneration (OP_{reg}) provided are the driving forces for this processes.*

3.1.1. Types of Dyes for DSSC

A large number of possible modification in the chemical structure of the sensitizer has made it one of the most investigated components for DSSC optimization. Nowadays large libraries of dyes are available, and the relations between chemical structure modification and electrochemical effects on the overall device have been intensively studied. The structure of the dye has undergone an evolution process driven not only by the motivation to increase the IPCE but also by the emphasis on low production costs and exploitation of abundant raw materials, thus following the same trend observed for the evolution of the other PV technologies explained in the first chapter. A brief summary of well-known dye classes is reported below, following a classification depending on the chemical structure; the various categories are reported following the chronological order in which they were first described in the literature.

3.1.1.1. Metallorganic complexes

The first type of dyes reported for DSSC application were metallorganic complexes of ruthenium, (*Figure 3.2*) designed to exploit the metal-to-ligand charge transfer transition, resulting in a wide absorption of the UV-Vis spectrum. In these dyes, the metal cation plays a central role: thanks to its *d* and *f* atomic orbitals it can set energy gaps which fit very well with the energy of the UV-Vis light, moreover the charge-transfer from the metal central core to the surrounding ligands create a dipole oscillation responsible for negligible molar extinction coefficients (ε). Other than finely shaping the photochemical properties of the complex, the ligands are also responsible for the anchoring and the electronic connection to the semiconductor substrate, which are crucial for the electron injection and are obtained using suitable anchoring groups, such as carboxylic acids.

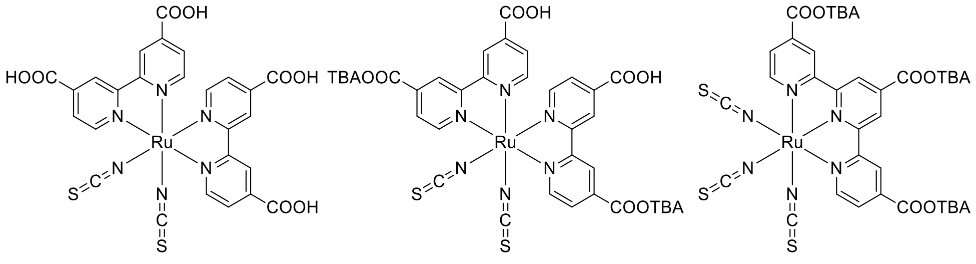

N3 **N719** **N749 (Black Dye)**

*Figure 3. 2: **Ruthenium dyes**: some of the most popular complexes are reported.*

The first compounds reported were polypyridine complexes of ruthenium,[5] which allow absorbing light over a wide region of the visible spectrum. Among the most known dyes for DSSC **N3**,[6,7] **N719**[7,8] and **N749** (also known as "black dye"),[9] (*Figure 3.2*) are still widely used as reference compounds when testing new dyes or as standard dyes when studying other components of DSSC. Many other metallorganic compounds can be found in the literature, some of which are based on other metals such as Osmium,[10,11] Iron,[12–14] Rhenium,[15,16] Platinum[17–19] and Copper[20,21] but no significant improvement compared to the Ruthenium-based dyes performances are reported.

Despite their excellent performances, this class of dyes has lost much of its interest for practical applications since the availability and cost of rare metals such as Ruthenium does not fit the mass production purpose of PV technology. In addition to availability and costs, due to their relatively low molar extinction coefficients ($\varepsilon \leq 20000$ L mol^{-1} cm^{-1}) a thick semiconductor film is usually required to achieve an effective photoactive layer when using these dyes, and their absorption spectra do not always cover the IR region, which is of great interest due to the presence of a significant solar spectrum emission in that region.

3.1.1.2. Organic dyes

Since the working mechanism of DSSC is inspired by the photosynthesis process, it makes sense to employ as photosensitizer compounds similar to chlorophyll such as porphyrins[22–24] and phtalocianines[23,25,26] in either free or complexed form. Despite the expectations, generally, the results obtained using this kind of dyes were not relevant except for some cases of particularly elaborated push-pull structures.[27,28]

Many organic dyes have been used as photosensitizers for DSSC, encompassing the most different chemical structures such as triarylamines,[29–31] squaraines,[32–34] polyenes,[35,36] indolines,[37–39] heteropolycyclics,[40–42] hemicyanines,[43] cyanines,[43–45] coumarins,[46–48] carbazoles,[49–51] and BIDIPY.[52,53]

However, in this class of miscellaneous dyes, there is no general architecture and the difference in the structures is mostly due to changes in the main core itself, selected for their photo-absorbing properties; for such reason, the dyes cannot be easily modulated in their electrochemical properties to better fit the requirements mentioned above. Moreover, even if this category of dyes does not require rare metals, the synthesis and purification of some of these compounds still require expensive procedures.

3.1.1.3. D-π-A organic dyes

Among organic dyes, D-π-A structures play a very important role. This class of compounds is characterized by a modular design of the chemical structure, which is characterized by the presence of three different portions: a donor moiety (D), a conjugated π-spacer and an acceptor (A). The modular nature of the chemical structure gives access to an enormous number of combinations that allows to obtain and tune the desired stereo-electronic and photo-physical characteristics by the variation of small molecular fragments, according to accurate structural design. (*Figure 3.3*) The donor group is constituted by an electron rich moiety, on which a high density of electrons is located in the ground state. On the other side of the molecule, an electron withdrawing moiety is introduced with the task to accept the electrons in the excited state and anchor the dye to the semiconductor substrate.

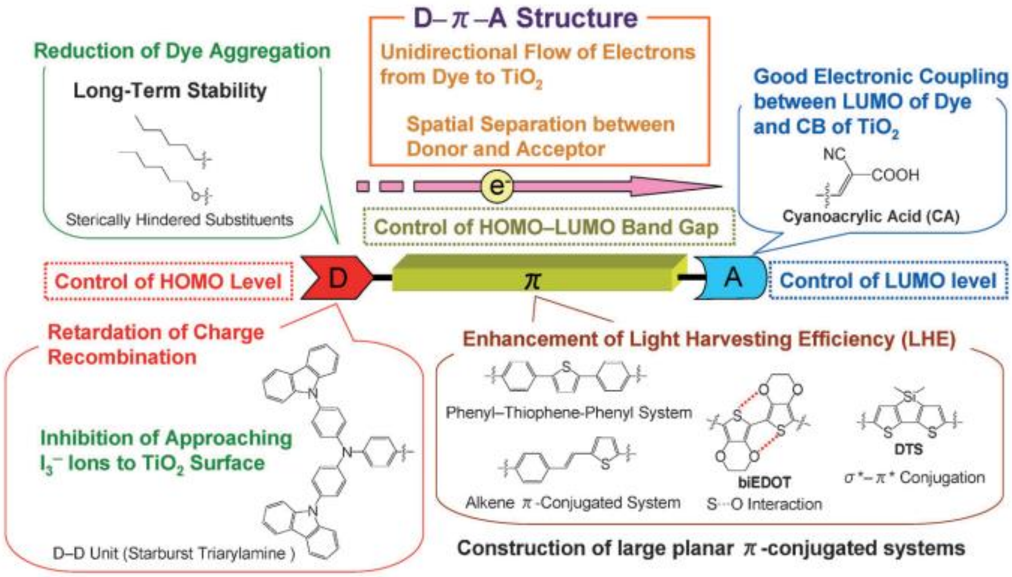

*Figure 3. 3: **D-π-A dye structure**: correlation between structure and photophysical and electrochemical properties for the donor part (D), the acceptor (A) and the conjugated bridge (π) linking this two. Reproduced from ref.*[3]

If we take into account the frontier orbitals of the dye, we can easily imagine that, due to the electron density disposition among energetic states, modification of the donor group will influence mostly the energy and shape of the HOMO level while the acceptor group will be mostly responsible for those of the LUMO. The donor and acceptor groups have to be separated to keep the donor part away from the semiconductor substrate, but at the same time, the electronic connection has to be guaranteed. Such task is carried out by the conjugated bridge (π). Variation of the length of the conjugated π-bridge can influence the width of the visible absorption spectrum of the dye, while the conformation of the conjugated system can influence its shape. In many cases, the final structure is relatively planar and therefore prone to aggregation on TiO_2 surface. Such phenomenon is known as π-π stacking and results in the enhancement of excited state non-radiative quenching and reduction of electron injection. Commonly the IPCE in organic dye-based devices is improved by addition of co-adsorbents to break up dye aggregates.[25] In D-π-A dyes such task can also be accomplished by the introduction of bulky groups, such as alkyl chains and additional aromatic units, which can minimize dye aggregation on titania. This modification can be useful to avoid the use of co-adsorbents, which on one hand reduces dye-loading on the semiconductor surface, and consequently the photocurrent and on the other hand makes the cell composition more complex. The use of metal-free organic dyes with a D-π-A-type architecture offers some other potential advantages which are characteristic of all organic dyes, such as an efficient light-harvesting due to high molar extinction coefficient[3] and absence of precious or rare metals.

3.1.1.4. D-A-π-A

The D-π–A structure has been a constant in the literature of organic dyes for DSSC for several years, and has led to the discovery of some of the most efficient dyes; for this reason, the exploration of novel designs was not systematically undertaken so far. However, recently some interesting alternatives have been suggested. In 2011, Zhu *et al.*[54] found that incorporation of an additional EWG unit into the π-bridge as an internal acceptor of electrons displays several advantages, and called such innovative structure D-A-π-A.[54] (*Figure 3.4*) The acceptor unit incorporated into the conducting bridge can be regarded as an electron trap because the electron density of the LUMO orbital is evenly localized across the A-π-A system, facilitating electron transfer from the donor to the acceptor/anchoring moiety. The internal electron-poor function was found to conveniently tune the molecular energy gap and in some cases increase the V_{OC}, as well as tailor the molecular structure creating new sites for facile introduction of modifications. Finally, the most important effect is related to the stability of the dye. The internal acceptor greatly improves the photostability of the sensitizer by trapping the electrons in the excited state immediately after photoexcitation. In other words, the energy of the LUMO level is reduced, therefore avoiding that electron-rich donor moieties, such as indoline, undergo undesired electrochemical decomposition under light irradiation.[55]

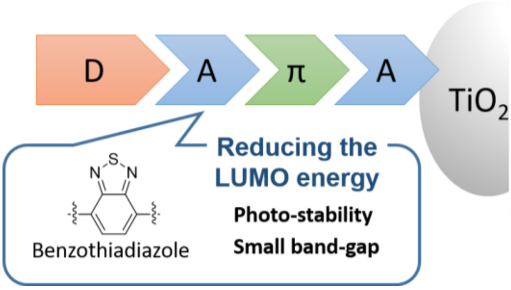

*Figure 3. 4: **D-A-π-A dye structure**. The A-π-A system withdraws electrons more efficiently than a single acceptor moiety. The dye gain photo-stability and the smaller band-gap allow a more efficient light absorption.*[56]

The functional groups that have been employed for this new structural concept include: diketopyrrolopyrrole,[57–59] benzothiadiazole,[54,55,60,61] benzotriazole[62,63] and quinoxaline.[64,65] Based on a collection of the early D-A-π-A dyes, structural and electronical correlation of the newly introduced accepting moiety were highlighted. For instance, it was found that bulky substituents on the internal acceptor can efficiently prevent π-π stacking, but on the other hand can also be responsible for twisting the dye structure, hampering electronic conjugation. This means that a careful balance of the two effects is required. Furthermore, the proximity of the donor and the internal acceptor was found to be essential to guarantee the electron trapping effect as a reverse design such as D-π-A-A would instead suffer from a rapid charge recombination. Finally, the use of an excessively strong EWG group could result in blocking the electron flow to the acceptor moiety or lowering the LUMO of the dye so much that it could no more inject into the TiO_2 CB. Therefore, optimization of the donor-acceptor couple has to be taken into account when facing this new design.

Despite the large variety of dyes tested in DSSCs throughout the years, there are still, some properties that need optimization. A good sensitizer should certainly have a high light harvesting ability and fast injection kinetics, two features which are essential to achieve high efficiency in PV devices. At the same time, long-term stability would be fundamental to make DSSC a competitive technology against Silicon PV, and some other special characteristics, such as transparency and peculiar colors, would definitely contribute to make it more attractive towards potential market applications.

3.2. Carboxy pyridinium dyes: seeking performances

Anchoring/acceptor groups of D-π-A dyes have been less investigated compared to the other sections of the molecules, but at the same time they are essential not only to provide a good binding and electronic coupling between the semiconductor and the dye, but also for the stability of the cell, which is influenced by the linkage between the sensitizer and TiO_2.[66],[29] Currently, the most used anchoring group is by far cyanoacrylic acid, which is able to ensure good electronic communication between the dye and TiO_2 by forming a strong bidentate bridging linkage with the surface.

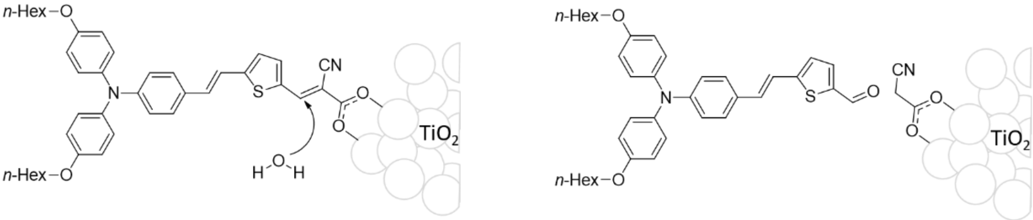

*Figure 3. 5: **Cyanoacrylic anchoring function**. Left: the strong bidentate linkage responsible for high staining of the semiconductor. Right: retro-aldol reaction results in dye detachment.*[67]

For these reasons, this moiety is present in most of the D-π-A type dyes prepared until now. However, it has been also reported that cyanoacrylic acids could undergo an undesirable retro-aldol degradation reaction within the photovoltaic cell. (*Figure 3.5*) In the presence of moisture and under UV light irradiation, the cyanoacrylic moiety can break leading to dye detachment[67] and therefore limiting the device lifetime. In order to improve the stability of the dyes, the search for new anchoring groups is a very promising approach.

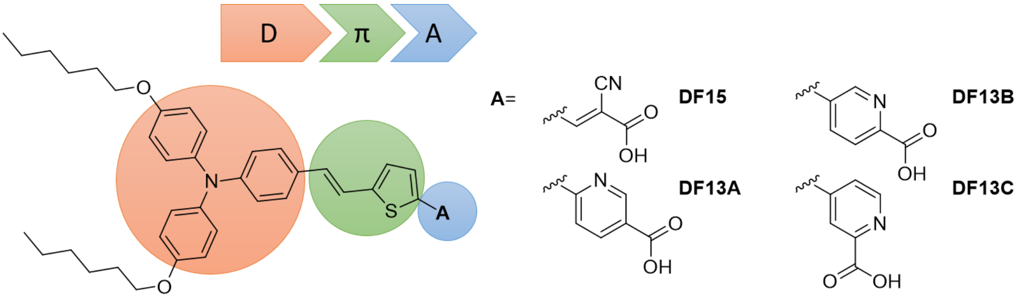

Figure 3. 6: ***Carboxy pyridine anchoring dyes****. The cyanoacrylic acceptor/anchoring function of a D-π-A dye was replaced with different isomers of carboxypyridines showing remarkable increase of dye stability.*[29]

In a precedent work[29] carried out in the group of research, carboxypyridines were selected as a suitable candidate to replace cyanoacrylic acid as the anchoring function, (*Figure 3.6*) since they present carboxylic acid moiety, essential to ensure the linkage with TiO_2, next to an electron-poor functional group included in an aromatic ring, which maintains the electronic conjugation with the dye. To evaluate the effectiveness of this new anchoring moiety, a series of sensitizers characterized by the same donor (a substituted triarylamine) and π spacer (vinyl-thiophene moiety), but with different regioisomeric carboxypyridines as acceptor groups (**DF13A-C** *Figure 3.6*) were synthesized. Test cells were built using compounds **DF13A-C** and their efficiencies measured. The results obtained in such study show that, indeed, carboxypyridines are valuable acceptor group for DSSCs. Although the starting power conversion efficiencies of cells built with **DF13A-C** were lower than that observed for the cyanoacrylic reference dye (**DF15**), they were found to be much more stable. In particular, **DF13C** was found to overcome the efficiency of the reference dye in less than 200h. (*Figure 3.7*)

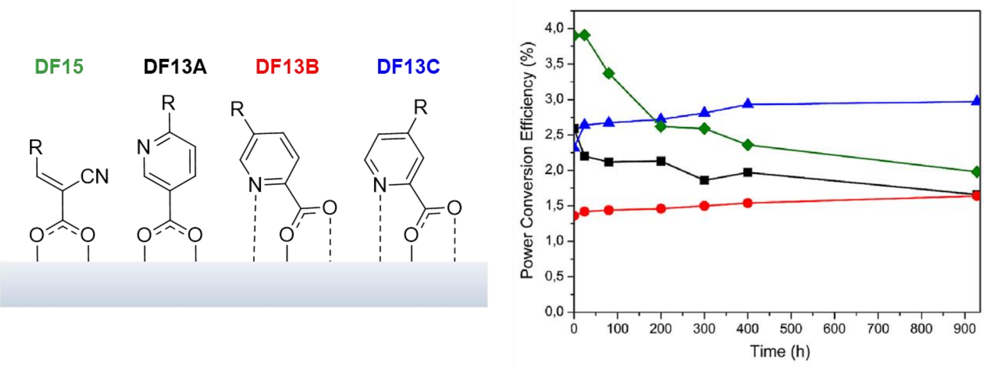

Figure 3. 7: ***Aging test and proposed anchoring mechanism*** *for dyes* ***DF13A-C*** *and* ***DF15.***[29]

Such behavior was attributed to a possible cooperative effect of the nitrogen atom and the adjacent carboxylate group on the dye binding to TiO_2, influenced by the relative position of the two functional groups. (*Figure 3.7*)

Later on, further dyes with a carboxypyridine anchoring moiety were described by other research groups, proving the effectiveness of such anchoring function.[27,68] However, although the stability of such heteroaromatic anchoring group seemed to be well assessed, its introduction caused some drawbacks such as a blue shift of the UV-Vis absorption spectra of the dyes and a lower IPCE compared to the cyanoacrylic analog **DF15,** which showed that, probably, simple carboxypyridines were not electron withdrawing enough.

Interestingly, we observed that the color of the free carboxypyridine dyes changed a lot according to the pH, probably due to protonation of the nitrogen atom. This fact suggested that alkylation of the heteroatom, transforming the carboxypyridine anchoring moiety into a methyl-carboxy pyridinium salt might have a beneficial effect due to the strengthening of the electron withdrawing ability of the pyridinium ring compared to a simple pyridine. (*Figure 3.8*) Such modification would have made impossible the synergic anchoring proposed for **DF13C** and **DF13B** but the retro-aldol decomposition typical of cyanoacrylic dyes would be still avoided. To validate this hypothesis, we decided to prepare two new dyes (**DF39A** and **DF39C**), where the relative regiochemistry of the substituents was chosen in order to maximize the electron-withdrawing effect of the pyridinium moiety by conjugation with the unsaturated backbone of the molecule (substitution in position 2- and 4- of the pyridine ring, respectively), and to study the effect of such modification both on the spectral properties of the dyes and on the performances of the corresponding DSSCs.

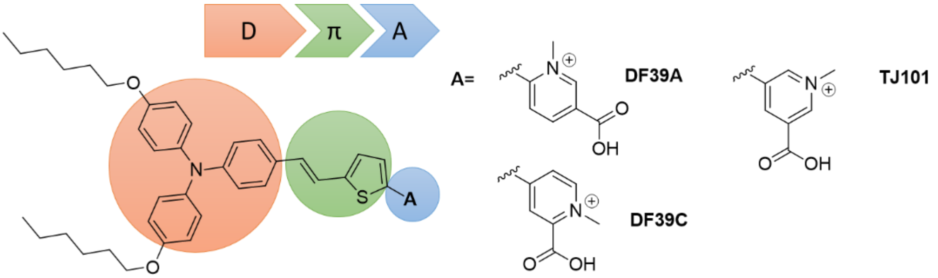

*Figure 3. 8: **Carboxy pyridinium dyes**: the proposed structure **DF39A** and **DF39C**[69] are compared to an analog compound recently reported **TJ101**[70]*

While we were working on the synthesis of compounds **DF39A** and **DF39C**, Sun *et al.*[70] published a similar compound (**TJ101**), having instead an *m*-carboxyl-*N*-methylpyridinium anchoring group linked to the same π-spacer and donor group. Interestingly, dye **TJ101** showed improved performance if compared to its non-alkylated analog, when applied as DSSC sensitizer. Such findings prompted us to continue our work, as our isomers seemed to be even more promising thanks to the conjugation of the pyridinic nitrogen with the rest of the chromophore.

3.2.1. DFT calculations

Before starting the synthetic work, the photochemical properties of the proposed molecules were modeled by means of DFT (density functional theory) calculations. This was possible thanks to a collaboration with Dr. Adalgisa Sinicropi from the University of Siena, who carried out all the theoretical computations reported in this work.

The structures of **DF39A** and **DF39C** were optimized by means of DFT calculations at the B3LYP/6-31G* level, using the Gaussian 09 package. Differently from **DF39C**, **DF39A** was found not to have a planar structure, with a tilt angle of approximately 35° between the thiophene and the pyridinium ring. This was probably due to the steric crowding derived from the *ortho*-methyl substitution. Energy, shape and electron-density distribution of the frontier orbitals were then computed for both dyes and compared with those of their non-methylated analogs. (*Figure 3.9*) An increasing spatial separation between the electron-density distribution of the HOMO and that of the LUMO was clearly observed passing from **DF13** to **DF39**. For both dyes the HOMO was mainly located on the donor triarylamine moiety, whereas the LUMO was mostly distributed on the terminal pyridinium rings, suggesting a good degree of charge separation upon photoexcitation. In addition, **DF39A** and **DF39C** were found to have very stabilized LUMOs compared to **DF13A** and **DF13C** because of the stronger EWG character of their positively charged pyridinium rings, resulting in much smaller HOMO–LUMO gaps, that was promising in view of a possible red-shift of their electronic absorption spectra.

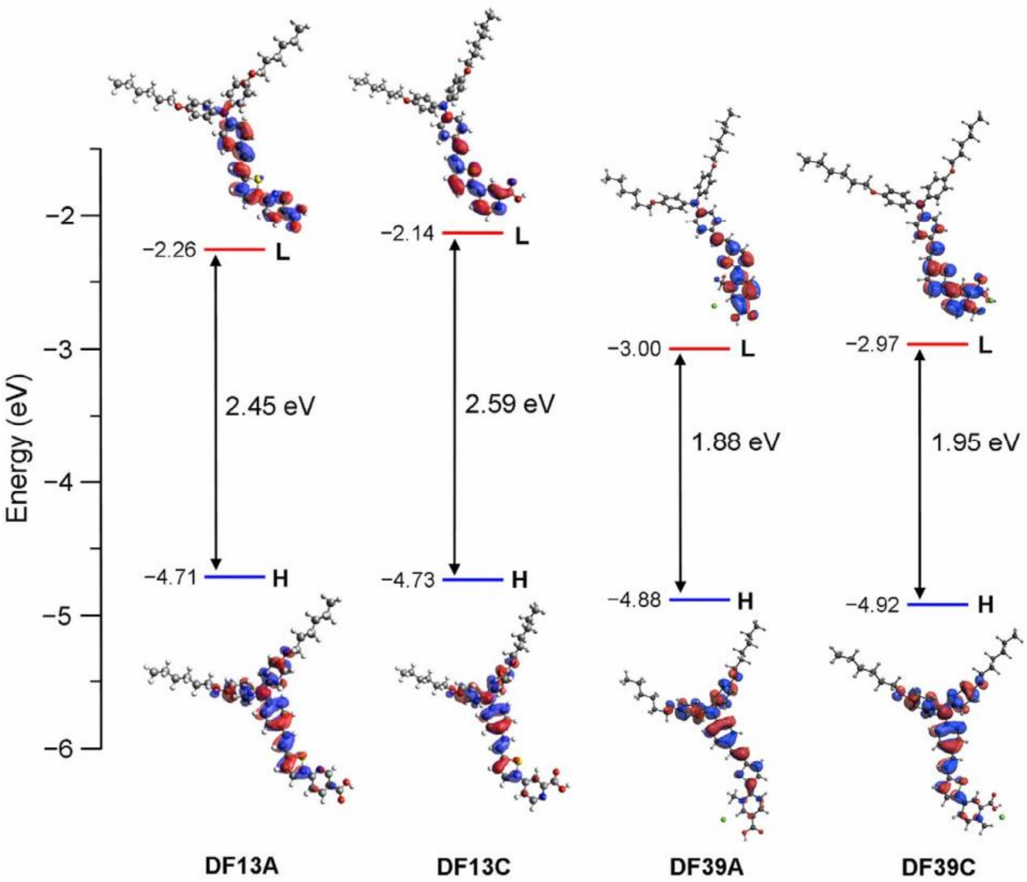

*Figure 3. 9: **DFT modeling**: wave function plots, orbital energies and frontier orbital energy gaps of compounds **DF13A**, **DF13C**, and the relative carboxylic methyl-pyridinium dyes **DF39A** and **DF39C**.*[69]

The absorption maxima (λ_{max}), oscillator strengths (f), and vertical excitation energies (E_{exc}) of compounds **DF39A** and **DF39C** were computed both at the PCM/TD-CAM-B3LYP/6-31G* and PCM/TD-MPW1K/6-31G* level[71–75]. (*Table 3.1*) As expected, with both functional, a bathochromic shift was predicted for the N-methylated compounds in comparison to **DF13A** and **DF13C**. Moreover, **DF39A** had a roughly 15–17 nm blue-shifted absorption compared to **DF39C**, which was attributed to the more planar structure of the latter, giving rise to a more extended conjugation. For both dyes, photoexcitation was calculated to occur mostly by HOMO–LUMO transitions, accounting for 74–89% of the total.

Table 3. 1: Absorption maxima (λ_{max}), oscillator strengths (f), vertical excitation energies (E_{exc}) and main electronic transitions computed by means of PCM/TD-CAM-B3LYP/6-31G and PCM/TD-MPW1K/6-31G* for dyes **DF39A, C** and **DF13A, C** and **TJ101** taken as reference. [a] value taken from reference[29]. [b] value taken from reference[70].*

Dye	Functional	λ_{max} (nm)	f	E_{exc} (eV)	Main transitions (%)
DF39A	CAMB3LYP	498	1.68	2.49	H→L 74
	MPW1K	536	1.53	2.31	H→L 89
DF39C	CAMB3LYP	513	1.69	2.42	H→L 74
	MPW1K	554	1.53	2.24	H→L 88
DF13A[a]	CAM-B3LYP	431	1.864	2.88	-
	MPW1K	454	1.757	2.73	-
DF13C[a]	CAM-B3LYP	420	1.881	2.95	-
	MPW1K	443	1.755	2.80	-
TJ101[b]	Experimental	459	-	2.70	-

3.2.2. Synthesis of the dyes

Supported by DFT calculations we decided to prepare compounds **DF39A** and **DF39C** by methylation of carboxypyridines **DF13A** and **DF13C**, which were prepared following our recently reported procedure.[29] However, direct formation of the pyridinium salt by reaction with MeI or Me_2SO_4, as reported in the case of Sun's dye **TJ101**,[70] was not trivial, and in our hands gave only the undesired esterification of the carboxylic acid moiety. Such difference in reactivity could be due to a deactivation of the nitrogen atom in **DF13A** and **DF13C** resulting from the conjugation of its lone pair with the unsaturated backbone of the molecules. Such effect, in the case of **DF13C** would also be exacerbated by electron donation to the neighboring carboxylic moiety. Consequently, we had to explore and establish a new synthetic procedure. Our approach is described in *Scheme 3.1*. Initially, we tried to react compounds **DF13A** and **DF13C** with a stronger electrophile, but, when they were directly treated with an excess of Me_3OBF_4, although the desired pyridinium salts were indeed obtained, the formation of the methyl esters also occurred. Since saponification with KOH proved to be unsuccessful, we chose to protect the carboxylic acid moiety as the corresponding allyl ester, prefiguring a possible palladium-mediated deprotection under neutral conditions. Compounds **1** and **2** were thus prepared by activation of the corresponding acids with oxalyl chloride followed by *in situ* reaction with allyl alcohol. Methylation of esters **1** and **2** using Me_3OBF_4 occurred smoothly, and acid **DF39C** was directly obtained after workup, probably because of spontaneous deprotection under the basic conditions employed. On the contrary, in the case of substrate **1**, the same conditions led to the formation of compound **3** which, after purification by flash chromatography, was deprotected with $Pd(PPh_3)_4$ to give the desired compound **DF39A** in good yield.

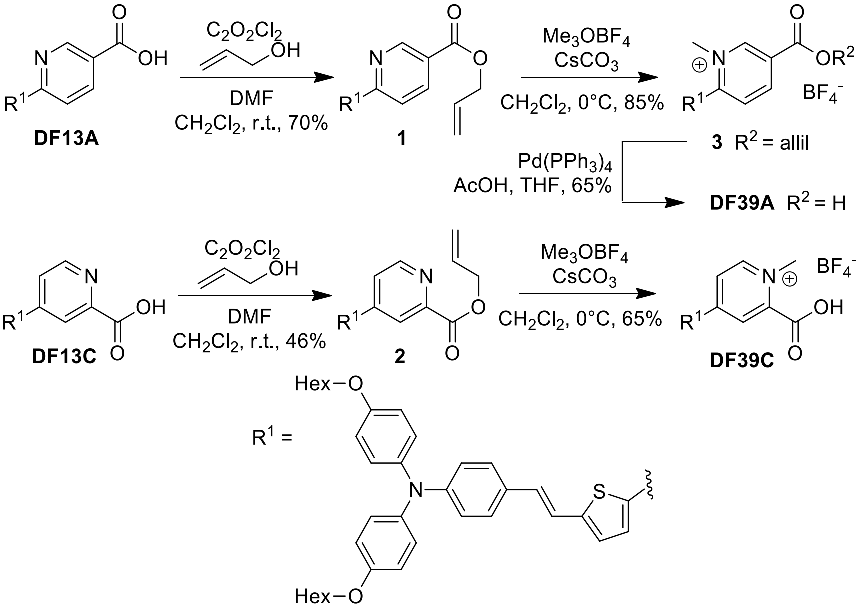

*Scheme 3. 1: **Synthetic strategy** for compounds **DF39A** and **DF39C**.*

3.2.3. Spectroscopic and Electrochemical characterization

Compounds **DF39A** and **DF39C** were purified by chromatography and their UV-Vis absorption spectra recorded both in CH_2Cl_2 and EtOH solution. (*Figure 3.10*) Absorption maxima, as well as the other optical and electrochemical data, are reported in *Table 3.2*, together with values for **TJ101** and for the carboxypyridine dyes **DF13A** and **DF13C**.

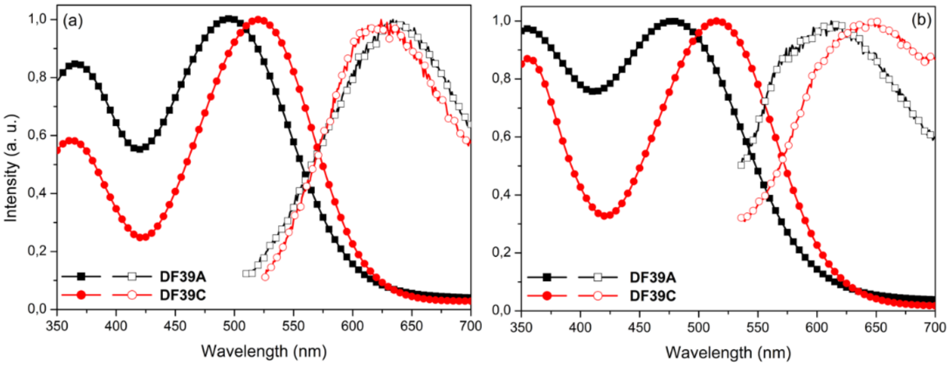

*Figure 3. 10: **UV-Vis spectra for DF39A and DF39 C** in a) CH_2Cl_2 and b) EtOH. Absorption spectra are reported in solid points and emission spectra in hollow ones.*

*Table 3. 2: Absorption maxima (λ_{max}), molar extinction coefficient (ε), emission maxima (λ_{emi}), registered in CH_2Cl_2, optical band gaps (E_{0-0}), ground-state oxidation potentials (E_{OX} vs. NHE), excited-state oxidation potential (E^*_{OX} vs. NHE, calculated as $E^*_{OX} = E_{OX} - E_{0-0}$) and absorption maxima on TiO_2 films (λ_{TiO2}) for dyes **DF39A**, C, and **DF13A**, C and **TJ101** taken as reference. [a] value taken from reference[29]. [b] values taken from reference[70].*

Dye	λ_{max} (nm)	ε (L/mol cm)	λ_{emi} (nm)	E_{0-0} (eV)	λ_{TiO2} (nm)	E_{ox} (V)	E^*_{ox} (V)
DF39A	493	1.73×10^4	634	2.21	483	0.89	-1.32
DF39C	520	1.43×10^4	624	2.17	483	0.89	-1.29
DF13A[a]	450	2.69×10^4	624	2.37	424	0.91	-1.46
DF13C[a]	445	2.03×10^4	622	2.39	423	0.93	-1.46
TJ101[b]	459	3.10×10^4	-	2.23	449	0.61	-1.62

In CH_2Cl_2 solution, compound **DF39A** had a 24 nm blue-shifted absorption maximum compared with **DF39C**, which was in agreement with the simulated data; both dyes exhibited blue-shifted absorption maxima in EtOH solution, possibly because of partial deprotonation of the carboxylic group. By measuring their fluorescence in solution, the optical band gaps (E_{0-0}) were obtained from the intersection of the normalized absorption and emission spectra in the same solvent. (*Table 3.2*) Compared with the corresponding pyridine carboxylates **DF13A** and **DF13C**, methylated dyes had largely red-shifted spectra in both solvents, showing the superior EWG ability of their positively charged pyridine rings, although their molar absorptivities were lower. In addition, they also had 37–61 nm red-shifted absorptions compared with reported regioisomeric pyridinium salt **TJ101**,[70] owing to the beneficial effect of having the alkylated nitrogen atom in conjugated position relative to the backbone of the sensitizer. When dyes **DF39A** and **DF39C** were absorbed on TiO_2, they gave very similar UV-Vis absorption spectra (*Figure 3.11*) both with a maximum at 483 nm, superior to those displayed by carboxypyridines **DF13A** and **DF13C** and pyridinium salt **TJ101**. The spectra appeared broader and slightly blue-shifted compared with those recorded in CH_2Cl_2, probably because of partial deprotonation of the dyes[76] as well as aggregation on the semiconductor surface. The hypsochromic shift observed when passing from CH_2Cl_2 solution to TiO_2 was larger for compound **DF39C** than for compound **DF39A** (37 nm vs. 13 nm). Again this can be a consequence of the more planar structure of the former, in turn resulting in a higher tendency to form blue-shifted H aggregates.[77]

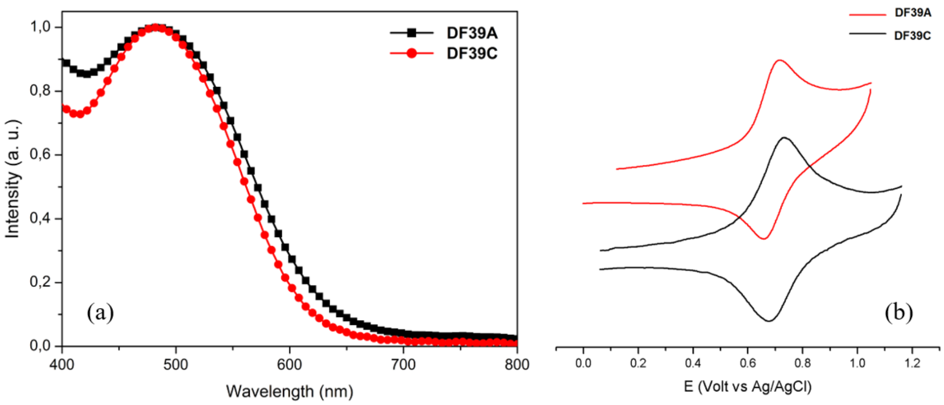

Figure 3. 11: a) ***Absorption spectra*** *recorded for the dyes adsorbed on* TiO_2 *thin films, and b)* ***Cyclic voltammetry****, for dyes* ***DF39A*** *and* ***DF39C****.*

The ground-state oxidation potentials (E_{OX}) of compounds **DF39A** and **DF39C** were measured by means of cyclic voltammetry (*Figure 3.11*, *Table 3.2*). Both dyes underwent reversible oxidation processes at the same potential (+0.89 V vs. NHE), which is more positive than the redox potential of the iodide–triiodide couple (+0.4 V vs. NHE), suggesting that regeneration of the sensitizers by the latter is possible. In addition, the excited state oxidation potentials ($E^*_{OX} = E_{OX} - E_{0\text{-}0}$) of the two dyes were found more negative than the conduction band edge of TiO_2 (–0.5 V vs. NHE), thus allowing smooth electron injection from the excited dye to titania.

3.2.4. Test on devices

Finally, the ability of the new compounds to serve as DSSC sensitizers was tested. This was done thanks to the collaboration with Prof. Aldo di Carlo and the Centre for Hybrid and Organic Solar Energy (C.H.O.S.E.) of the University of Rome "Tor Vergata". Large-area strip cells (3.6 cm^2) containing a thin nc-TiO_2 photoanode (3 μm) were built, employing a procedure characterized by simple fabrication conditions (no scattering layer, no surface treatments). The cells were completed with a platinum-based cathode and an I^-/I_3^- liquid electrolyte. Cell performances were measured under

AM 1.5G simulated solar irradiation (incident power 100 mW/cm^2) and compared with those of reference organic dye **D35**.[78]

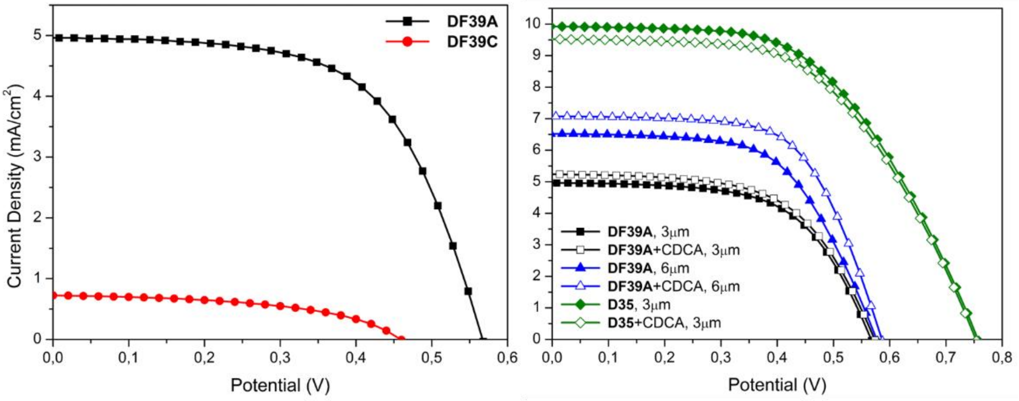

*Figure 3. 12: Left: **J/V plots** for **DF39A** and **DF39C**. Right: **optimization of DF39A performances**.*

Unfortunately, satisfactory photovoltaic parameters were obtained only for compound **DF39A**, (*Figure 3.12*) as dye **DF39C** appeared to be unstable once adsorbed on TiO_2, rapidly turning to yellow and eventually detaching from the semiconductor under irradiation, thus giving cells with very low efficiencies (<0.2%). When sensitization of the photoanodes was carried out in the absence of any co-adsorbent, dye **DF39A** provided a power conversion efficiency of 1.69%, corresponding to approximately 42% of that obtained with **D35**, mostly due to a limited value of the photocurrent (around 5.0 mA cm^{-2}). Thus, a second set of cells was prepared adding chenodeoxycholic acid (CDCA) to the dye bath in order to minimize dye aggregation, resulting in a slight improvement of efficiency. Finally, another series of **DF39A**-containing cells was built with a thicker semiconductor layer of 6 μm. Under these conditions, devices built without CDCA gave an efficiency of 2.17%, which was further improved to 2.61% by addition of the co-adsorbent. Such result showed that no general improvement of device performance resulted from alkylation of the pyridine ring of **DF13A,** since the latter gave an efficiency of 2.79% under the same conditions.[29] Moreover, this study confirms that a positive charge on the acceptor part of the dyes exerts a negative influence on V_{OC} (581–587 mV for **DF39A** as opposed to 648 mV for **DF13A**, see *Table 3.3*), possibly because of a shift in the conduction band potential of TiO_2 caused by the concentration of positive charges on its surface.[1]

Table 3. 3: Performances for DSSC sensitized with ***D35, DF13A,*** *and* ***DF39A****.*

Dye	CDCA	TiO_2 (μm)	J_{SC} (mA cm^{-2})	V_{OC} (mV)	*ff*	η (%)
D35	-	3	9.93	758	0.54	4.06
	+	3	9.52	754	0.55	3.93
DF39A	-	3	5.06	567	0.59	1.69
	+	3	5.04	572	0.59	1.72
	-	6	6.32	581	0.60	2.61
	+	6	7.19	587	0.62	2.79
DF13A	-	6	6.83	648	0.63	2.79

To understand the reason of the instability of dye **DF39C** when adsorbed on TiO_2, we prepared a red solution of the dye in slightly basic acetonitrile (ACN), obtained by the addition of an aqueous ammonia solution: half of this solution was mixed with a slurry of TiO_2, and both the clear solution and the slurry were left at room temperature under visible-light irradiation for 24 hours, after which the solution of the dye maintained its color, while the slurry became pale yellow.

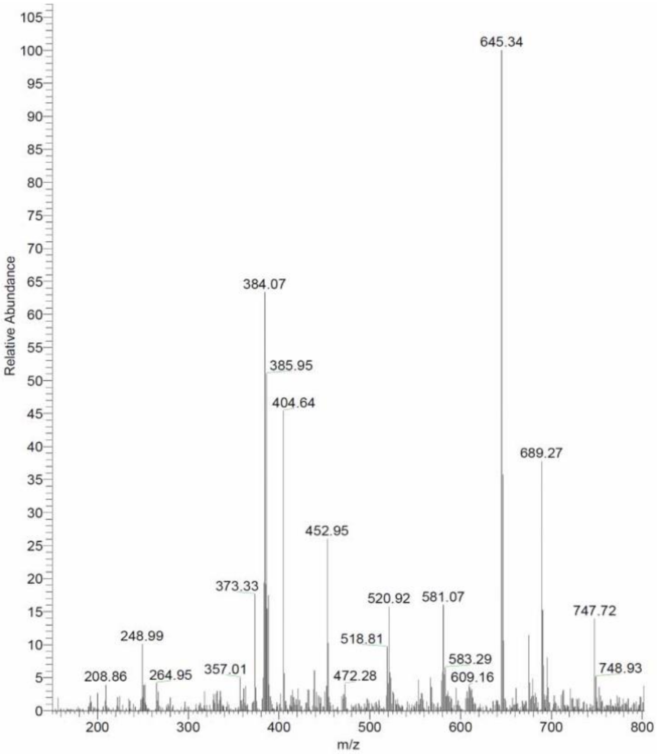

*Figure 3. 13: A****nalysis of DF39C decomposition products****. ESI-MS spectrum of the sample obtained by filtration of the* ***DF39C****/TiO_2 slurry after irradiation for 24 h in ACN/aqueous ammonia.*

The latter sample was analyzed by ESI-MS after filtration of the solids, and a main decomposition compound having *m/z* = 645, corresponding to decarboxylation of the picolinic moiety, was identified. (*Figure 3.13*) This was found in agreement with related literature works reporting that pyridine-2-carboxylic acids (i.e., 2-picolinic acids) undergo thermal decarboxylation more easily than their 3- and 4- isomers [79] and that the corresponding N-alkylated pyridinium 2-carboxylates release CO_2 more than 700 times faster than 2-picolinic acid itself.[80] This effect was enhanced in the presence of TiO_2, leading to decarboxylation even under very mild conditions, probably because of a photocatalytic reaction triggered by UV light.[81,82] Despite the improvements of the spectroscopic characteristics due to a more effective EWG in the anchoring moiety, the DSSC sensitized with the carboxy pyridinium anchoring dyes did not perform better than the starting compounds, instead, a great loss in stability was found. This is an evidence that the optimization of a single property of a complex system like DSSC may also result in negative effects in the complete devices.

3.2.5. Experimental section

Protection of carboxypyridines: general procedure

The appropriate carboxypyridine **DF13A, C** (253 mg, 0.37 mmol, 1.0 eq.) was dissolved in dry dichloromethane (2 mL) and then oxalyl chloride (38 μL, 0.45 mmol, 1.2 eq.) was added, giving rise to a blue solution. One drop of DMF was added and evolution of gas was observed. After 10 minutes, allyl alcohol (128 μL, 1.88 mmol, 5.0 eq.) was added. The reaction mixture was left under stirring for an hour, then quenched with aq. phosphate buffer (pH 7.5) and extracted with ethyl acetate (10 mL). The red organic phase was washed with water (2 × 5 mL) and brine (5 mL), then dried on Na_2SO_4. The solvent was removed under reduced pressure and the crude product purified by flash chromatography.

(*E*)-Allyl 6-(5-(4-(*bis*(4-(hexyloxy)phenyl)amino)styryl)thio-phen-2-yl)nicotinate (1)

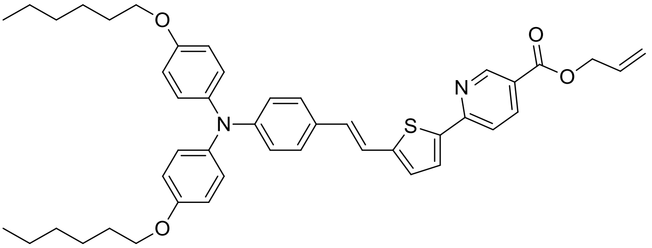

Purified by flash column chromatography (PE/EtOAc 50:1 to 5:1). Yield: 50 mg (0.07 mmol, 70%). Red amorphous solid.

(**1**): ^{1}H-NMR (200 MHz, $CDCl_3$) δ_H = 9.17 (1H, d, *J* = 1.8 Hz), 8.25 (1H, dd, *J* = 8.4, 2.2 Hz), 7.65 (1H, d, *J* = 8.4 Hz), 7.56 (1H, d, *J* = 4.0 Hz), 7.28 (2H, d, *J* = 8.4 Hz), 6.78 - 7.14 (13H, m), 5.93 - 6.16 (1H, m), 5.44 (1H, dd, *J* = 17.2, 1.5 Hz), 5.33 (1H, d, *J* = 11.4 Hz), 4.86 (2H, d, *J* = 5.5 Hz), 3.94 (4H, t, *J* = 6.6 Hz), 1.68 - 1.88 (4H, m), 1.29 - 1.58 (12H, m), 0.93 (6H, t, *J* = 6.2 Hz) ppm. ^{13}C-NMR{^{1}H} (100 MHz, $CDCl_3$) δ_C = 164.8, 155.7, 151.1, 148.8, 147.7, 140.9, 140.2, 137.5, 131.9, 130.1, 128.3, 127.9, 127.3, 127.2, 126.8, 126.3, 123.2, 119.9, 118.6, 118.5, 117.6, 115.2, 68.2, 65.7, 31.6, 29.3, 25.7, 22.6, 14.0 ppm; IR (KBr) cm^{-1} 3046, 2852, 1715, 1591. MS (ESI) *m*/*z* calculated for $C_{45}H_{50}N_2O_4S$: 714.3. Found: 715.4 $[M+1]^+$.

(*E*)-Allyl 4-(5-(4-(*bis*(4-(hexyloxy)phenyl)amino)styryl)thio-phen-2-yl)picolinate (2)

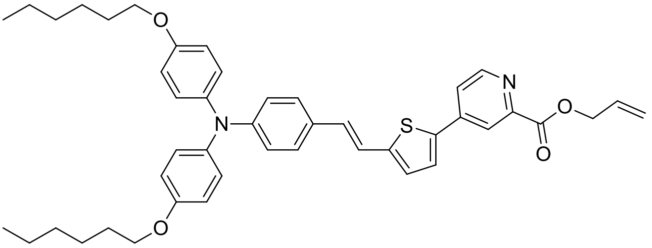

Purified by flash column chromatography (PE/EtOAc 50:1 to 5:1). Yield: 73 mg (0.10 mmol, 46%). Red-orange amorphous solid.

(**2**): ^{1}H-NMR (400 MHz, $CDCl_3$) δ_H = 8.68 (1H, d, *J* = 5.2 Hz), 8.29 (1H, d, *J* = 1.3 Hz), 7.57 (1H, dd, *J* = 5.2, 1.3 Hz), 7.47 (1H, d, *J* = 3.7 Hz), 7.28 (2H, d, *J* = 8.4 Hz), 7.11-6.79 (13H, m), 6.21- 6.01 (1H, m), 5.46 (1H, dd, *J* = 17.0, 0.9 Hz), 5.34 (1H, dd, *J* = 10.3, 0.9 Hz), 4.94 (2H, d, *J* = 5.9 Hz), 3.93 (4H, t, *J* = 6.4 Hz), 1.87-1.68 (4H, m), 1.51-1.31 (12H, m), 0.92 (6H, t, *J* = 6.2 Hz) ppm. ^{13}C-NMR{^{1}H} (100 MHz, $CDCl_3$) δ_C = 164.5, 155.4, 150.0, 148.6, 148.2, 146.2, 142.3, 139.8, 138.4, 136.8, 131.4, 129.9, 127.7, 127.0, 126.6, 126.1, 121.7, 120.4, 119.5, 119.0, 117.8, 115.0, 68.1, 66.6, 31.6, 29.3, 25.7, 22.6, 14.0 ppm. IR (KBr) cm^{-1} 3041, 2953, 2927, 1735, 1722, 1589. MS (ESI) *m/z* calculated for $C_{45}H_{50}N_2O_4S$: 714.3. Found: 715.3 [M+1]$^+$.

Synthesis of (*E*)-5-(Allyloxycarbonyl)-2-(5-(4-(*bis*(4-(hexyloxy)phenyl)amino) styryl) thiophen-2-yl)-1-methylpyridinium tetrafluoborate (3)

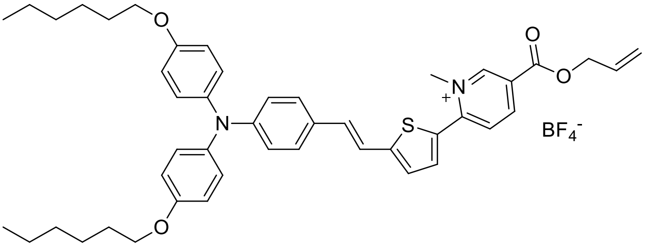

Ester **1** (40 mg, 0.06 mmol, 1.0 eq.) was dissolved in dry CH_2Cl_2 (1 mL), the solution was cooled at 0° C, then Cs_2CO_3 (73 mg, 0.22 mmol, 4.0 eq.) and trimethyloxonium tetrafluoroborate (Me_3OBF_4, 24 mg, 0.16 mmol, 3.0 eq.) were added. The solution was stirred at 0° C for 15 minutes, then warmed to room temperature and left under stirring overnight. The reaction mixture was diluted with dichloromethane (10 mL), the organic phase was washed with a cold saturated solution of NH_4Cl (10 mL) and the aqueous solution extracted with dichloromethane (2 × 10 mL). The combined organic phases were dried on Na_2SO_4. The solvent was removed under reduced pressure and the crude product purified by flash column chromatography (CH_2Cl_2/MeOH/formic acid 10:1:0.1). A red-violet amorphous solid was recovered (37 mg, 0.05 mmol, 85% yield).

(**3**): ^{1}H-NMR (200 MHz, $CDCl_3$) δ_H = 9.27 (1H, br s), 8.70 (1H, d, *J* = 7.0 Hz), 8.07 (1H, d, *J* = 7.0 Hz), 7.79 (1H, br s), 7.44-6.94 (9H, m), 6.94-6.53 (6H, m), 6.20-5.78 (1H, m), 5.65-5.22 (2H, m), 4.87 (2H, d, *J* = 4.4 Hz), 4.57 (3H, br s), 3.93 (4H, t, *J* = 12.5 Hz), 1.95-1.62 (4H, m), 1.56-1.07 (12H, m), 0.91 (6H, t, *J* = 5.5 Hz) ppm. ^{13}C-NMR{^{1}H} (100 MHz, $CDCl_3$) δ_C = 161.4, 156.4, 154.2, 152.4, 150.2, 149.1, 143.6, 140.0, 137.6, 134.2, 131.2, 129.6, 128.4, 127.5, 127.3, 127.2, 127.1, 126.8, 120.5, 119.5, 116.6, 115.7, 68.6, 67.9, 49.4, 31.9, 29.6, 26.1, 23.0, 14.4 ppm. IR (KBr) cm^{-1} 3056, 2987, 1735, 1627, 1593. MS (ESI) *m/z* calculated for $C_{46}H_{53}N_2O_4S$: 729.4. Found: 729.4 [M]$^+$

Synthesis of (E)-6-(5-(4-(bis(4-(hexyloxy)phenyl)amino)styryl)thiophen-2-yl)-1-methylpyridin-1-ium-3-carboxylate (DF39A)

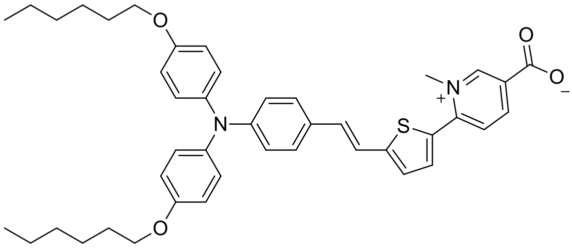

Allyl ester **3** (25 mg, 0.03 mmol, 1.0 eq.) was dissolved in dry THF (0.5 mL), then Pd(PPh_3)$_4$ (4 mg, 0.003 mmol, 0.1 eq.) and acetic acid (30 µL, 0.34 mmol, 10.0 eq.) were added. The solution was stirred at r.t. for 4 h, then the reaction mixture was diluted with Et_2O (1 mL), and washed with water (2 × 10 mL) and brine (10 mL). The organic phase was dried over Na_2SO_4, then the solvent was removed under reduced pressure, and the crude product purified by preparative TLC (CH_2Cl_2/MeOH = 10:1). A red-violet amorphous solid was recovered (15 mg, 0.02 mmol, 65% yield).

(**DF39A**): ^{1}H NMR (200 MHz, DMSO-d$_6$): δ_H = 9.35 (1 H, s), 8.70 (1 H, d, *J* = 7.3 Hz) 8.16 (1 H, d, *J* = 8.8 Hz), 7.80 (1 H, d, *J* = 3.7 Hz), 7.54–7.31 (3 H, m), 7.29–6.80 (10 H, m), 6.70 (2 H, d, *J* = 7.7 Hz), 4.40 (3 H, s), 3.91 (4 H, t, *J* = 6.2 Hz), 1.80–1.51 (16 H, m), 1.48–0.98 (6 H, m) ppm. ^{13}C NMR{^{1}H} (50 MHz, DMSO-d$_6$): δ_C = 155.9, 150.6, 149.2, 148.8, 148.4, 146.2, 144.0, 139.6, 135.7, 131.9, 130.1, 129.9, 129.2, 128.4, 128.3, 127.5, 126.8, 118.6, 117.6, 115.8, 68.0, 48.0, 31.4, 29.1, 25.4, 22.5, 14.3 ppm. IR (KBr): 3681, 3051, 2931, 1724, 1595 cm^{-1}. HRMS: *m/z* calculated for $C_{43}H_{49}N_2O_4S$: 689.3413; found: 689.3422 [M]$^+$.

Synthesis of (E)-4-(5-(4-(bis(4-(hexyloxy)phenyl)amino)styryl)thiophen-2-yl)-1-methylpyridin-1-ium-2-carboxylate (DF39C)

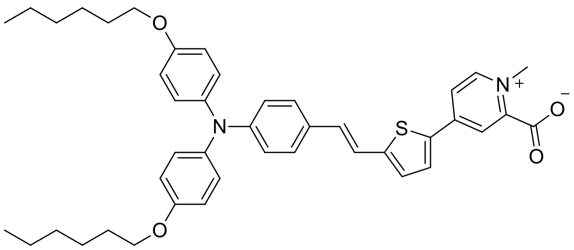

Ester **2** (73 mg, 0.10 mmol, 1.0 eq.) was dissolved in dry CH_2Cl_2 (1.7 mL), the solution was cooled to 0° C, then Cs_2CO_3 (150 mg, 0.46 mmol, 4.5 eq.), and trimethyloxonium tetrafluoroborate (Me_3OBF_4, 80 mg, 0.54 mmol, 5.4 eq.) were added. The solution was stirred at 0° C for 15 min, then warmed to r.t. and left under stirring overnight. The reaction mixture was diluted with CH_2Cl_2 (10 mL), the organic phase was washed with a cold sat. solution of NH_4Cl (10 mL), and the aqueous solution extracted with CH_2Cl_2 (2 × 10 mL). The combined organic phases were dried over Na_2SO_4. The solvent was removed under reduced pressure, and the crude product was purified by preparative TLC (CH_2Cl_2–MeOH = 10:1). A red-violet amorphous solid was recovered (59 mg, 0.08 mmol, 65% yield).

(**DF39C**): ^{1}H NMR (200 MHz, $CDCl_3$): δ_H = 8.56 (1 H, d, *J* = 6.2 Hz), 8.13 (1 H, d, *J* = 3.9 Hz), 8.02–7.98 (2 H, m), 7.41 (2 H, d, *J* = 8.6 Hz), 7.33 (1 H, d, *J* = 3.7 Hz), 7.27 (1 H, d, *J* = 16.0 Hz) 7.10 (1 H, d, *J* = 16.0 Hz), 7.02 (4 H, d, *J* = 8.9 Hz), 6.90 (4 H, d, *J* = 8.9 Hz) 6.70 (2 H, d, *J* = 8.6 Hz), 4.18 (3 H, s), 3.92 (4 H, t, *J* = 6.5 Hz), 1.77–1.57 (4 H, m), 1.52–1.34 (4 H, m), 1.34–1.25 (8 H, m), 0.86 (6 H, t, *J* = 6.8 Hz) ppm. ^{13}C NMR{^{1}H} (100 MHz, $CDCl_3$): δ_C = 156.0, 149.7, 145.1, 139.8, 138.6, 135.2, 133.4, 133.2, 128.0, 127.9, 127.2, 127.1, 127.0, 126.6, 120.1, 119.2, 117.0, 116.6, 115.6, 115.3, 68.3, 31.6, 31.5, 29.3, 25.7, 22.6, 14.0 ppm. IR (KBr): 3676, 3056, 2978, 1658, 1593 cm^{-1}. HRMS: *m/z* calculated for $C_{43}H_{49}N_2O_4S$: 689.3413; found: 689.3428 [M]$^+$.

3.3. Exploring blue-green colorations: D-A-π-A dyes

Although dyes for DSSC able to provide relatively high efficiencies have already been obtained and, as shown in the previous chapter, the path for improving the dye stability has already been undertaken, there are other issues which have been less investigated and need to be addressed.

A very important point is that most of the dyes reported so far have a coloration ranging from yellow to red. Generally, aiming for a record efficiency, dyes are designed to display a broad absorption of the solar spectrum, therefore resulting in colorations from brown to black, which narrows the range of their potential applications. In this scenario, the new challenge in the field of building integrated PV is to complete the palette of colorations available for DSSCs The development of libraries of dyes characterized not only by long-term stability and considerable high efficiency, but also by a wide choice of colors, would make the exploitation of DSSCs much more appealing from an architectural point of view.

As we have already shown, organic dyes can be an ideal solution for such purpose, since they have relatively narrow absorption bands, that allow fine tuning of the resulting coloration, compensated by high values of molar absorptivities, allowing an intense coloration of the semiconductor film even at low dye loadings.

In particular, so far, near-IR absorbing blue dyes have been less investigated compared to other classes of sensitizers, prompting us to study the synthesis and characterization of compounds with such spectral properties.

To design dyes possessing the desired features, we referred to D-A-π-A structures. With such design, a relatively small energy gap between the frontier orbitals is predicted, resulting in an absorption in the NIR wavelength range and a consequent blue coloration of the molecule. D-A-π-A dyes can be obtained by insertion of an internal acceptor moiety in the conjugate scaffold of the previously presented dye **DF15** as reported in *Figure 3.14*.

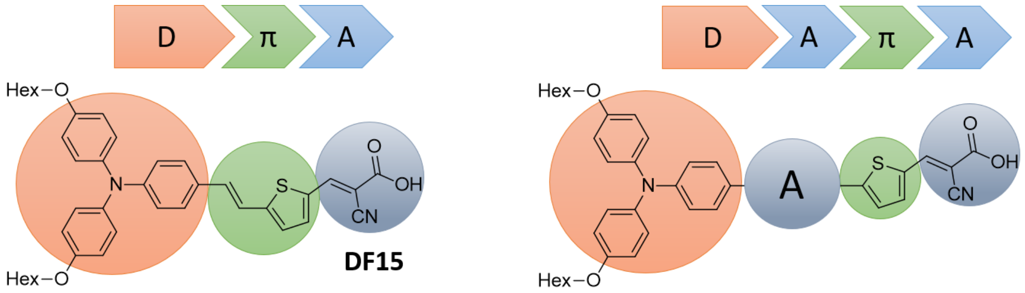

Figure 3. 14: Left: ***D-π-A dye DF15.*** *Right:* ***D-A-π-A derivatization of dye DF15*** *can be obtained by adding an internal acceptor moiety between the donor group and the π-bridge.*

In the proposed structure the modified triphenylamine and cyanoacrylic acid are used as the donor and anchoring groups and the thiophene π scaffold was coupled with different acceptors. Such choice was simply driven by our precedent experience, which provided us with readily available building blocks and a good knowledge of the assembling procedures.

In this part of the work, I will report the design of new D-A-π-A dyes featuring internal acceptor groups such as Indigo and Bis-imidazolylidene-dione (BID) within their structure. These two scaffolds are known to be electron-poor compounds and have already had some application in optoelectronics[83] but, to the best of my knowledge, they have not yet been introduced in the structure of DSSC dyes. The main reason why they were chosen for this project is their deep blue coloration. Indeed, compounds possessing both these structural units have a strong absorption peak at around 600 nm resulting in a very intense blue coloration even at low concentrations. We hoped that such feature could be maintained in the final D-A-π-A dyes as well, thus resulting advantageously in terms of their PV application.

3.3.1. Bis-imidazolylidene-dione (BID)

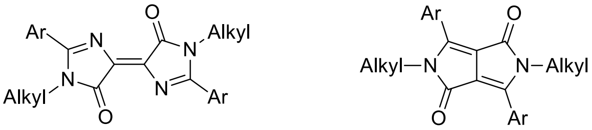

Figure 3. 15: Left: Bis-imidazolylidene-dione (BID) core Right: diketopyrrolopyrrole (DPP) core.

The BID scaffold was chosen for its structural similarity to diketopyrrolopyrrole (DPP, *Figure 3.15*), a structural motif that has been intensively studied as an electron acceptor in organic semiconductors for optoelectronic applications,[84–86] and as the internal acceptor in D-A-π-A dyes too.[57,58,87] As mentioned above, the conjugated system of BID was also employed as internal electron withdrawing group in symmetrical compounds applied to optoelectronic devices, and thus it fits all the structural and electronic requirements for its introduction in D-A-π-A dyes. BID shows strong absorptions in the range of 400–800 nm,[88] is almost planar and can be easily synthesized[88,89] from commercially available compounds. Alkyl groups can be introduced to endow the resulting dye with good solubility in organic solvents and prevent aggregation on TiO_2. Finally, derivatization *via* cross-coupling reactions using the Stille protocol has already been reported for the synthesis of symmetrical compounds[90]. In this project, a potential dye structure was designed, in which the BID core was connected on one side with a substituted triarylamine acting as the donor part, and on the other side with the anchoring cyanoacrylic moiety. (*Figure 3.16*) The intermediate thiophene rings were selected to facilitate the synthetic process, considering that the donor moiety could be inserted *via* a cross-coupling reaction and the anchoring moiety *via* a formylation of thiophene in the *α* position, followed by a Knoevenagel condensation to obtain the cyanoacrylic acid.

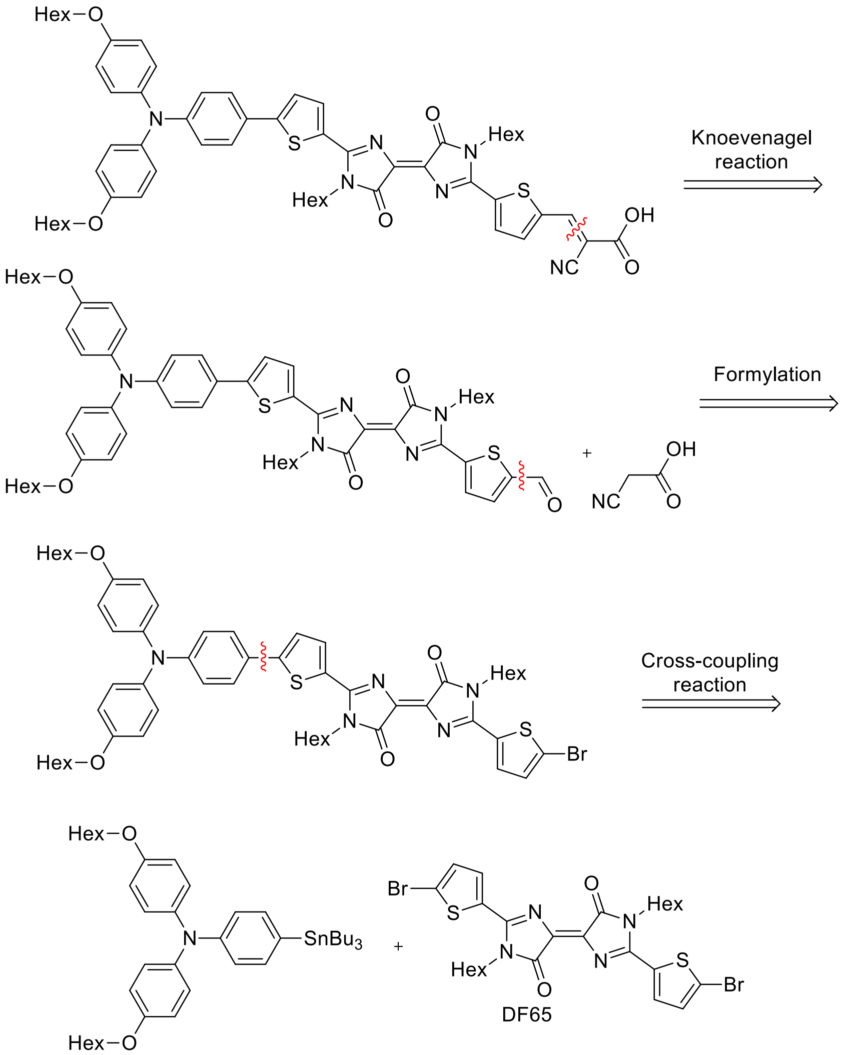

Figure 3. 16: Example of D-A-π-A dye based on BID internal acceptor moiety and proposed retrosynthesis.

3.3.1.1. Synthesis of the dyes

In view of the proposed retrosynthetic approach, we started with the synthesis of the central symmetrical bis-imidazolylidene-dione building block. In order to continue the synthesis *via* cross-coupling reactions, bromine substituted thiophene rings were selected as substituents on both sides of the BID structure, leading to intermediate **DF65**. (*Figure 3.16*)

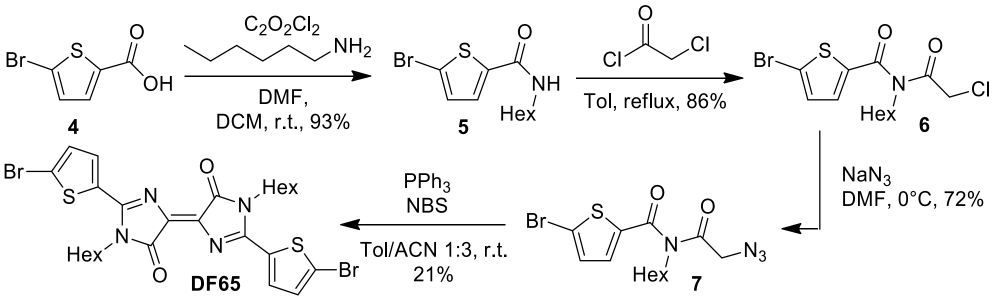

Scheme 3. 2: Synthetic path for BID core ***DF65****.*

The synthesis of precursor **7** was carried out with good yields applying some modification to the protocol reported in the literature[88]. (*Scheme 3.2*) Commercially available 5-bromothiophene-2-carboxylic acid **4** was reacted with 1-hexylamine in order to introduce a hydrophobic substituent on the nitrogen atom *via* activation as the corresponding acyl chloride. Secondary imide **6** was then obtained by reaction with chloroacetyl chloride, and the subsequent nucleophilic substitution with sodium azide afforded the BID precursor **7** in good yield. Finally, reduction of the azide by Staudinger reaction gave amine **8** that underwent intramolecular cyclization affording the intermediate imidazolidone **9**. (*Scheme 3.3*)

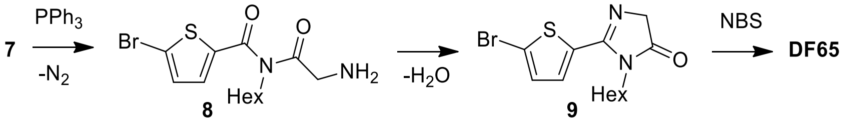

Scheme 3. 3: Synthesis of intermediate ***DF65*** *from azide* ***7****.*

Intermediate **9** was not isolated, and the progress of the reaction was monitored by the strong red opaque coloration assumed by the reaction mixture during the evolution of the process. Treatment of the crude reaction mixture with *N*-bromosuccinimide (NBS) afforded the desired product **DF65** although only in very low yield. A yellow side product was easily distinguishable from the blue BID core. Its formation was found to be promoted in aqueous basic solution and was ascribed to an intramolecular isomerization, (*Scheme 3.4*) with consequent loss of conjugation. Such behavior had already been observed for a similar scaffold. [91]

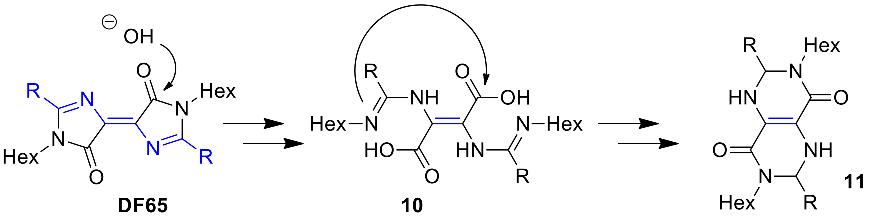

Scheme 3. 4: Isomerization of BID core to a non-conjugated structure

Efforts in reducing the formation of such side product by carrying out the last step with a catalytic amount of NBS (photochemical radical reaction) were unsuccessful. Instead, we found that the necessary amount of NBS was at least 1 equivalent, suggesting for the BID forming reaction a mechanism where bromination of imidazolidone **9** takes place before the intermolecular enol-condensation occurs (**15**), followed by the release of HBr to create the central double bond in **DF65**. (*Scheme 3.5*)

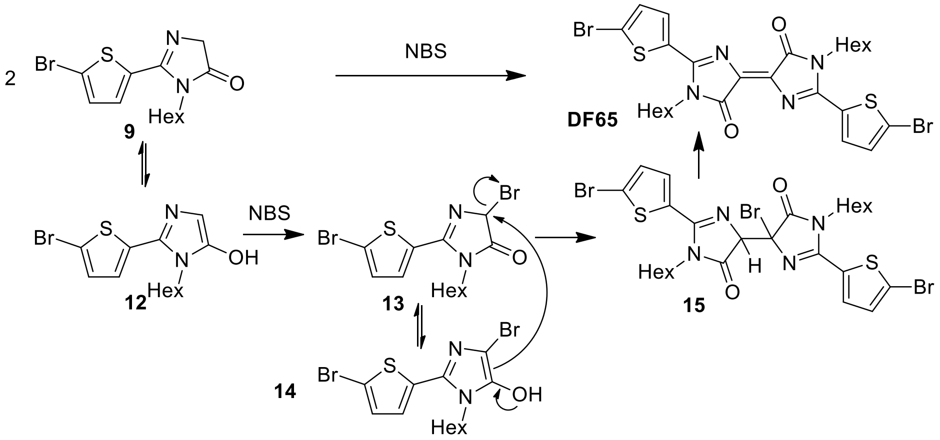

Scheme 3. 5: Mechanism of formation of the BID core in ***DF65****.*

The only improvement of the reaction outcome was obtained by conducting the reaction under anhydrous conditions and removing the triphenylphosphine oxide by precipitation with $MgCl_2$ after the formation of primary amine **8**,[92] therefore simplifying the final purification procedure. Once obtained the BID core **DF65**, we tried to couple it with the donor portion *via* Stille cross coupling. (*Scheme 3.6*) To this end, stannane **18** was synthesized starting from amine **16**, in turn, prepared as reported in previous works.[29] Compound **16** was brominated with NBS at room temperature to give bromide **17** in quantitative yield. Bromide **17** was then quantitatively converted to the desired stannane **18** *via* lithium-halogen exchange at -50° C and transmetallation with Bu_3SnCl. Complete conversion to product **18** was observed *via* NMR but impurities were generally not separated since the purification by chromatography would cause the product decomposition.

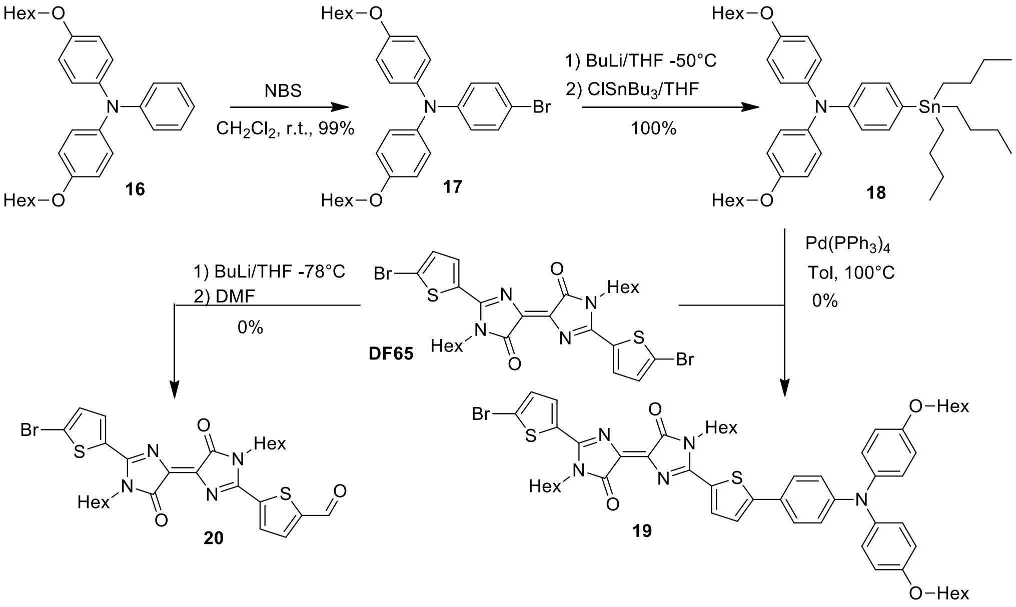

Scheme 3. 6: Attempts to derivatise the ***DF65*** *scaffold.*

Stille cross coupling between stannane **18** and bromide **DF65** was carried out under anhydrous conditions in order to preserve the BID core from isomerization using tetrakis(triphenylphosphine)palladium as catalyst and conducting the reaction at 100° C. In such conditions, the cross coupling resulted mostly in substrate decomposition, probably due to the high temperature required to start the reaction. Before trying to optimize the coupling conditions, we decided to test the formylation of **DF65** by means of metalation with *n*-BuLi and quench with DMF. Unfortunately, no better results were obtained in this case, as, not surprisingly, mostly isomerization of BID core was observed, affording **11**. Considering these results, we concluded that, even if a careful analysis of the reaction conditions could have led to an optimization of the synthetic procedure, the BID system was exceedingly sensitive to moisture, bases and high temperatures. Such characteristics do not fit the requirements for a stable DSSC dye, and therefore the project was abandoned.

3.3.1.2. Experimental section

Synthesis of 5-bromo-*N*-hexylthiophene-2-carboxamide (5)

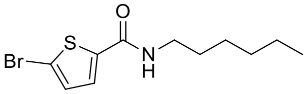

Carboxylic acid **4** (2.631 g, 12.7 mmol, 1.0 eq.) was dissolved in dry CH_2Cl_2 (44 mL), then oxalyl chloride (1.29 mL, 15.2 mmol, 1.2 eq.) and dry DMF (2 drops) were added. The solution was stirred at RT, upon which gas development was observed for 15 minutes, then the mixture was cooled down to 0° C and quenched with distilled 1-hexylamine (10.0 mL, 76.2 mmol, 6.0 eq.). The reaction mixture was stirred at r.t. overnight, then it was diluted with CH_2Cl_2 (30 mL), the organic phase was washed with a 1 M aq. solution of HCl (2 × 20 mL) and dried on Na_2SO_4. The solvent was removed under reduced pressure and the crude product purified by flash column chromatography (PE/EtOAc 40:1 to 5:1). A colorless liquid was recovered (3.421 g, 11.7 mmol, 93% yield).

(**5**): ^{1}H-NMR (200 MHz, $CDCl_3$) δ_H = 7.25 (1 H, d, *J* = 3.7 Hz), 7.02 (1 H, d, *J* = 3.7 Hz), 6.18 (1 H, br. s.), 3.38 (2 H, td, *J* = 7.1, 5.9 Hz), 1.49 - 1.68 (2 H, m), 1.26 - 1.37 (6 H, m), 0.82 - 0.93 (3 H, m) ppm. ^{13}C-NMR{^{1}H} (100 MHz, $CDCl_3$) δ_C = 160.0, 138.6, 132.3, 124.2, 140.6, 39.7, 31.4, 29.2, 26.5, 22.5, 13.9 ppm. MS (ESI) *m*/*z* calculated for $C_{11}H_{16}BrNOS$: 289.01. Found: 289.00 – 290.98 (1:1 due to the atomic mass distribution of bromine) $[M]^+$.

Synthesis of 5-bromo-*N*-(2-chloroacetyl)-*N*-hexylthiophene-2-carboxamide (6)

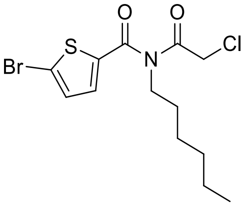

Amide **5** (2.787 g, 9.6 mmol, 1.0 eq.) was dissolved in dry toluene (30 mL) and 2-chloroacetyl chloride (1.98 mL, 26.0 mmol, 2.7 eq.) was added. The solution was stirred at reflux temperature for 2h, then the solvent was removed under reduced pressure. The reaction mixture was diluted with EtOAc (10 mL), the organic phase was washed with water (10 mL), NaOH 1M aqueous solution (10 mL) and finally brine (10 mL). The organic phase was dried on Na_2SO_4 and the solvent was removed under reduced pressure. The crude product was purified by flash column chromatography (PE/EtOAc 50:1 to 20:1). A pale yellow liquid was recovered (3.031 g, 8.26 mmol, 86% yield).

(**6**): ^{1}H-NMR (200 MHz, CDCl$_3$) δ_H = 7.38 (1 H, d, *J* = 4.0 Hz), 7.13 (1 H, d, *J* = 4.0 Hz), 4.39 (2 H, s), 3.86 (2 H, t, *J* = 7.7 Hz), 1.55 - 1.71 (2 H, m), 1.26 (6 H, s), 0.83 - 0.92 (3 H, m) ppm. ^{13}C-NMR{^{1}H} (100 MHz, CDCl$_3$) δ_C = 169.6, 165.4, 133.4, 131.0, 128.3, 122.6, 47.9, 44.3, 31.3, 28.9, 26.4, 22.4, 13.9 ppm. MS (ESI) *m/z* calculated for $C_{13}H_{17}BrClNO_2S$: 364.99. Found: 364.89 – 366.88 (1:1 due to the atomic mass distribution of bromine) $[M]^+$

Synthesis of *N*-(2-azidoacetyl)-5-bromo-*N*-hexylthiophene-2-carboxamide (7)

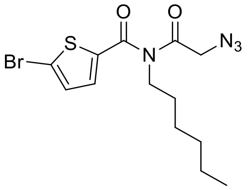

Compound **6** (3.202 g, 8.73 mmol, 1.0 eq.) was dissolved in dry DMF (13 mL), the solution was cooled to 0° C, then NaN$_3$ (1.413 mg, 21.7 mmol, 2.5 eq.) was added portionwise. The solution was warmed to room temperature and left under stirring for 1h. The reaction mixture was quenched with water (50 mL), extracted with EtOAc (30 mL), and the organic phase was washed with water (2 × 50 mL). The combined organic phases were dried over Na$_2$SO$_4$. The solvent was removed under reduced pressure to yield a red-orange oil, which was used as such in the following step (2.35 g, 6.32 mmol, 72% yield).

(**7**): ^{1}H-NMR (200 MHz, CDCl$_3$) δ_H = 7.36 (1 H, d, *J* = 4.0 Hz), 7.14 (1 H, d, *J* = 4.0 Hz), 4.17 (2 H, s), 3.88 (2 H, t, *J* = 7.3 Hz), 1.56 - 1.71 (2 H, m), 1.23 - 1.29 (6 H, m), 0.82 - 0.90 (3 H, m) ppm. ^{13}C-NMR{^{1}H} (100 MHz, CDCl$_3$) δ_C = 170.9, 165.8, 138.5, 133.2, 131.0, 122.4, 53.8, 47.4, 31.1, 28.8, 26.2, 22.3, 13.8 ppm. MS (ESI) *m/z* calculated for $C_{13}H_{17}BrN_4O_2S$: 372.03. Found: 371.97 – 373.86 (1:1 due to the atomic mass distribution of bromine) $[M]^+$.

Synthesis of 2,2'-*bis*(5-bromothiophen-2-yl)-1,1'-dihexyl-[4,4'-biimidazolylidene]-5,5'(1H,1'H)-dione (DF65)

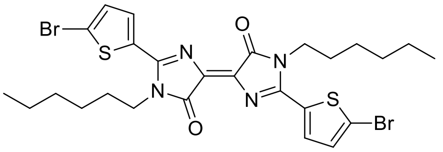

The BID core precursor **7** (1.78 g, 4.78 mmol, 1.0 eq.) was dissolved in dry toluene (20 mL), then triphenylphosphine (PPh_3, 1.38 mg, 5.26 mmol, 1.1 eq.) was added and the solution was stirred at room temperature for 1h. While releasing gas the red solution turned to lucid black, then $MgCl_2$ (1.0 g, 10.51 mmol, 2.2 eq.) was added and the solution was stirred overnight. The solid was filtered and 4Å molecular sieves were added. The solution was diluted with dry ACN (15 ml) and a solution of NBS (1.02 g, 5.74 mmol, 1.2 eq.) in dry ACN (10 mL) was added. The reaction mixture was stirred at room temperature for 4h and then filtered. The solvent was removed under reduced pressure and the crude product purified by flash column chromatography (CH_2Cl_2/PE 1:1 to 10:1, then CH_2Cl_2 then CH_2Cl_2/EtOAc 20:1 to 1:1). A dark blue amorphous solid was recovered (0.326 g, 0.50 mmol, 21% yield).

(**DF65**): ^{1}H-NMR (200 MHz, $CDCl_3$) $\delta_H = 7.62$ (2 H, d, $J = 4.0$ Hz), 7.20 (2 H, d, $J = 4.0$ Hz), 3.94 (4 H, t, $J = 7.5$ Hz), 1.61 - 1.86 (4 H, m), 1.27 - 1.47 (12 H, m), 0.81 - 0.95 (6 H, m) ppm. ^{13}C-NMR{^{1}H} (100 MHz, $CDCl_3$) $\delta_C = 167.4$, 156.4, 141.5, 130.1, 128.9, 127.4, 115.5, 47.2, 32.3, 28.5, 26.7, 22.1, 14.1 ppm. MS (ESI) *m/z* calculated for $C_{26}H_{30}Br_2N_4O_2S_2$: 652.02. Found: 652.00 – 654.01 – 655.98 (1:2:1 due to atomic mass distribution of bromine) $[M]^+$.

Synthesis of 4-bromo-*N, N-bis*(4-(hexyloxy)phenyl)aniline (17)

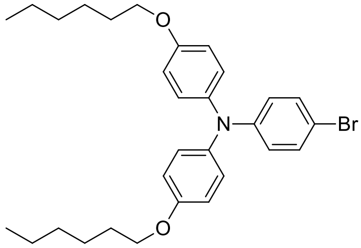

N,N-bis(4-(hexyloxy)phenyl)aniline **16** (0.82 g, 1.84 mmol, 1.0 eq.) was dissolved in dry CH_2Cl_2 (15 mL), then NBS (0.376 mg, 2.11 mmol, 1.15 eq.) was added. The solution turned black and it was stirred at room temperature in the dark for 2h. The reaction mixture was washed with water (2 × 20 mL) and the combined organic phases were dried on Na_2SO_4. The solvent was removed under reduced pressure to give a pale yellow oil (0.957 g, 1.82 mmol, 99% yield) which was used without further purification.

(**17**): ^{1}H-NMR (200 MHz, $CDCl_3$) δ_H = 7.20 – 7.27 (2 H, m), 6.98 – 7.07 (4 H, m), 6.75 – 6.85 (6 H, m,), 3.94 (4 H, t, *J* = 7.5 Hz), 1.70 – 1.86 (4 H, m), 1.32 – 1.51 (12 H, m), 0.86 – 0.98 (6 H, m) ppm. ^{13}C-NMR{^{1}H} (100 MHz, $CDCl_3$) δ_C = 155.7, 140.4, 136.3, 131.7, 131.6, 126.6, 121.9, 115.4, 68.4, 31.6, 29.3, 25.8, 22.6, 13.4 ppm.

Synthesis of 4-(tributylstannyl)-*N,N*-*bis*(4-(hexyloxy)phenyl)aniline (18)

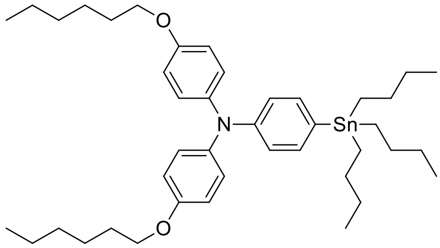

Bromide **17** (0.956 g, 1.82 mmol, 1.0 eq.) was dissolved in dry THF (9 mL), the solution was cooled at –78° C, then *n*-BuLi (1.6 M solution in hexanes, 1.35 mL, 2.16 mmol, 1.2 eq.) was added slowly. The solution was allowed to warm up slowly while stirring until it reached –50° C, then it was cooled down again to –78° C and tributyltin chloride (ClSnBu3 0.586 mL, 2.16 mmol, 1.2 eq.) was added. The solution was allowed to reach room temperature overnight, was diluted with Et_2O (10 mL), and the organic phase was washed with a saturated aq. solution of NH_4Cl (10 mL). The combined organic phases were dried on Na_2SO_4. The solvent was removed under reduced pressure and the crude reaction mixture was used as such for the following step.

(**18**): ^{1}H-NMR (200 MHz, $CDCl_3$) δ_H = 7.25 (2 H, d, *J* = 5.0 Hz), 7.08 (4 H, d, *J* = 4.2 Hz), 6.86 – 6.94 (2 H, d, *J* = 5.0 Hz), 6.69 – 6.76 (4 H, d, *J* = 4.3 Hz), 3.93 (4 H, d, *J* = 7.6 Hz), 1.68 – 1.87 (4 H, m), 1.22 – 1.60 (30 H, m), 0.81 – 1.10 (15 H, m) ppm. ^{13}C-NMR{^{1}H} (100 MHz, $CDCl_3$) δ_C = 155.5, 152.2, 140.9, 136.9, 131.8, 126.7, 120.2, 115.3, 68.4, 31.6, 29.2, 27.4, 25.8, 22.6, 14.0, 13.7, 9.6, 8.8 ppm.

3.3.2. Indigo

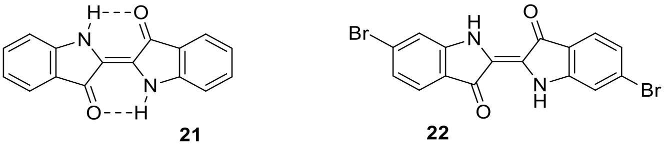

*Figure 3. 17: Blue indigo (**21**) and its derivative Tyrian Purple (**22**).*

The process of coloring fabrics with blue indigo dyes dates back to at least 2000 BC in many different civilizations. For a long time, Indigo (**21)** was the only available blue dye that could be used to color textiles, thus throughout ancient cultures clothes colored with indigo and Tyrian Purple (primary constituent: 6,6′-dibromoindigo **22**) were extremely valuable and a symbol of wealth and power.[93] Indigo's intense coloration is primarily due to the so-called "H-chromophore", a cross-conjugated system of two electron-donating functions and two acceptors. Light absorption results in the transfer of electron density from the amines to the carbonyl functions, representing the donor and acceptor groups, respectively[94]. (*Figure 3.17*)

Recently, it was found that Indigo,[83] Tyrian Purple[95] and similar molecules show interesting applications in the organic electronics field as building blocks for organic semiconductors. Indigo has an appealing symmetric ketoindole structure similar to that of DPP, is inexpensive and is characterized by elevated structural stability. For these many reasons, it was selected as a good candidate to be employed as internal acceptor moiety for D-A-π-A dyes. The most important drawback of the "H-chromophore" arrangement is the perfect planarity induced in the chemical structure, that makes indigo molecules prone to form scarcely soluble aggregates. Such problem can be solved either by protecting the amino functions with *tert*-butoxy carbonyl (Boc) protecting groups or by the introduction of appropriate solubilizing moieties in the structure. In the first case, the bulky Boc group makes the indigo structure bend around the central double bond between the indole rings,[96] causing the resulting compound to lose its characteristic blue coloration but increasing its solubility in common organic solvents. The latter modification can instead be accomplished either by using the amino- and carbonyl functions to form the so-called "bay-annulated Indigo" (BAI) form[97] (**23**) or by attachment of a branched alkyl chain onto the aromatic ring.

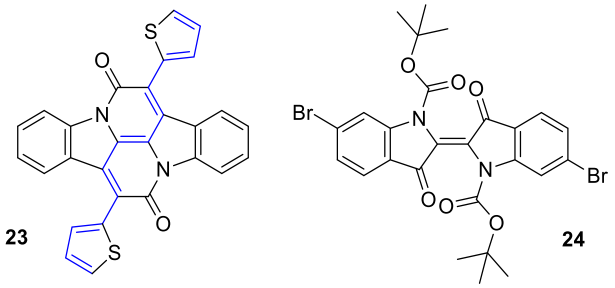
23

24

*Figure 3. 18: **Derivatives of Indigo** with relatively enhanced solubility: the bay-annulated indigo (**23**, BAI) and the Boc-protected one (**24**). The new conjugated direction is highlighted in compound **23**.*

While the original indigo "H-chromophore" can be released from its Boc-protected form simply by heating, BAI derivatization is permanent, and moreover, it creates a new direction for the possible extension of indigo structure: indeed, the conjugated system encompassing the bay-annulated chromophore (highlighted in blue in *Figure 3.18*) has already been exploited as acceptor moiety in organic semiconductors.[97]

To investigate the properties of the indigo core as internal acceptor moiety in D-A-π-A-type sensitizers, I decided to extend the conjugated scaffold in both directions: the one stretching along the BAI unsaturated system and the one passing through the two oxindole rings (structures **25** and **26** in *Figure 3.19*, respectively). In both cases, a substituted triarylamine was selected as the donor group and cyanoacrylic acid was the acceptor/anchoring moiety, which was linked to the indigo scaffold by means of a thiophene ring acting as a spacer. This way the designed structure can be studied as an adaptation to the DAPA design, of a previously studied DPA dye (**DF15**).[29]

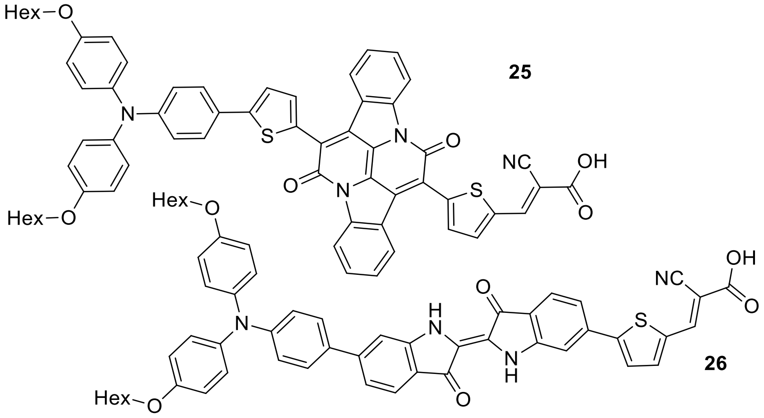
25

26

*Figure 3. 19: **D-A-π-A dyes bearing indigo derivatives as internal acceptor moiety**.*

The development of such structures has faced many synthetic obstacles that required both optimization of the reaction conditions and modifications of the synthetic pathway. The results of such studies are reported below.

3.3.2.1. Indigo-derived Dyes Synthesis

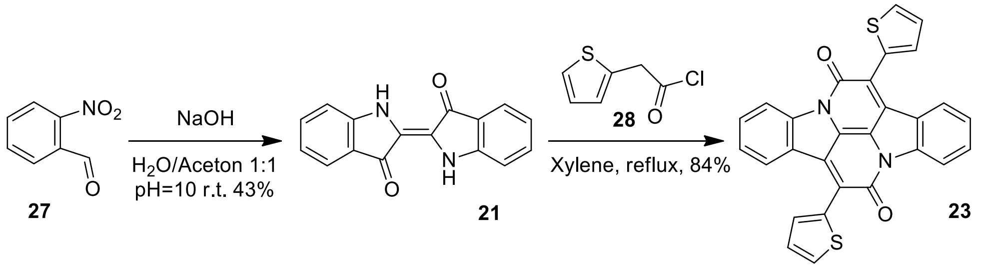

Scheme 3. 7: Synthesis of Indigo and BAI.

Indigo (**21**) was synthesized *via* a well-known protocol[98] involving basic treatment of 2-nitrobenzaldehyde (**27**) in a water/acetone solution: formation of the product was indicated by the appearance of a characteristic blue precipitate. Bay-annulation derivatization of such compound was performed with commercially available 2-thiopheneacetyl chloride (**28**) in refluxing xylene. (*Scheme 3.7*) The resulting compound **23** was found to be only sparingly soluble in organic solvents, which prompted us to prepare an analog of **23** carrying additional alkyl chains as solubilizing groups.

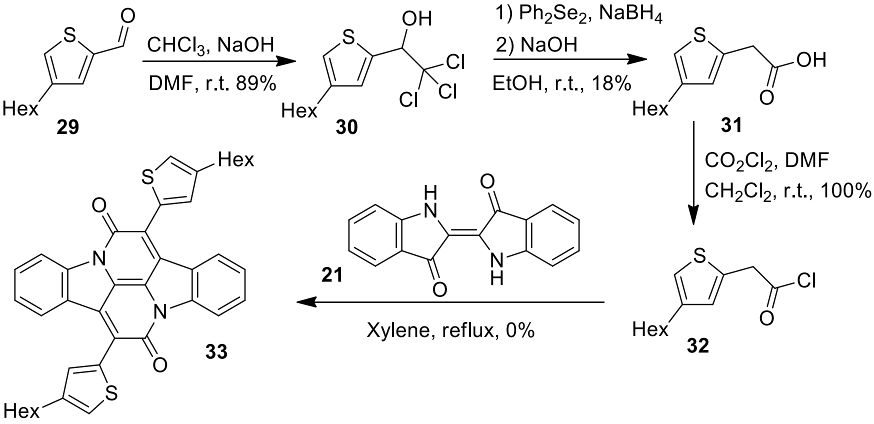

*Scheme 3. 8: Synthetic route for the hexyl functionalized BAI **33**.*

Thus, starting from commercially available 4-hexylthiophene-2-carboxaldehyde (**29**), homologation was performed through a Wyvratt reaction with chloroform,[99] followed by conversion to the carboxylic acid **31** with an *in situ*-formed phenylseleno-(triethyl)-borate complex[100]. (*Scheme 3.8*) Carboxylic acid **31** was obtained with an overall yield of 16% and was transformed in the corresponding acyl chloride **32** by treatment with oxalyl chloride right before performing the bay-annulation reaction with indigo (**21**). Unfortunately, acyl chloride **32** was not stable at the high temperature required by the annulation reaction, and oligomers were retrieved as the only products of the reaction.

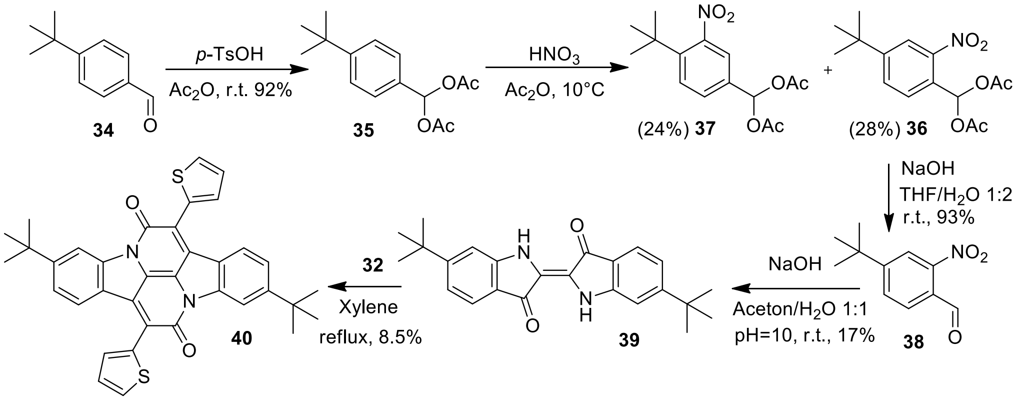

Scheme 3. 9: Synthetic route for the t-butyl functionalized BAI ***40****.*

I also explored the possibility to enhance the solubility by directly modifying the indigo structure, as reported in *Scheme 3.9*. The precursor for 6,6′ di-*tert*-butylindigo **39** was not commercially available, and therefore it needed to be synthesized from a suitable precursor. Even though nitration of 4-*tert*-butyltoluene would have probably yielded the desired 5-*tert*- butyl-2-methylnitrobenzene-regioisomer, the subsequent oxidation of a nitrotoluene derivative was considered too dangerous. For this reason, 4-*tert*-butylbenzaldehide (**34**) was instead chosen as the starting compound. In this case, direct nitration would have given the undesired isomer, and therefore the aldehyde function in **34** was transformed into the *ortho*-orienting geminal acetate **35,** which was obtained in very good yield. Nitration of **35** afforded the two isomers **36** and **37** in almost 1:1 molar ratio, which could be separated by flash column chromatography. Deprotection of compound **36** was carried out under basic conditions to give indigo precursor **38** in almost quantitative yield. The synthesis of 6,6′

di-tert-butylindigo **39** was then performed following the same procedure described above for Indigo (**21**), leading to the isolation of the desired product in 17% yield. As expected, compound **39** was perfectly soluble in organic solvents and characterized by an intense blue coloration. Probably, the low yield observed for its formation was indeed due to its increased solubility compared to indigo, since in that case the driving force of the reaction is considered to be the precipitation of the final product.

Once again, the bay-annulation reaction on compound **39** led mostly to decomposition of the substrate. A final effort was done to reduce the reaction temperature by trying to activate Indigo amino- function with strong bases. Such conditions led to the formation of a complex mixture of products in which the desired compound could not be found, demonstrating that the high temperature was needed not only to partially solve Indigo, but also to complete the bay-annulation reaction.

In view of the unsatisfying results obtained in the studies on the BAI structure, the following work was focused on the functionalization of the Indigo oxindole rings. With the aim of extending the conjugation of the Indigo structure by cross-coupling reactions, the Boc-protected, soluble derivative of the Tyrian Purple **24** was synthesized. (*Scheme 3.10*) Tyrian Purple **22** was obtained as a purple powder in 71% yield *via* the indigo-forming protocol described above, starting from commercially available 4-bromo-2-nitrobenzaldehyde (**41**). Boc protection was performed in DMF solution with (t-Boc)$_2$O giving a remarkably soluble deep red product in almost quantitative yield.

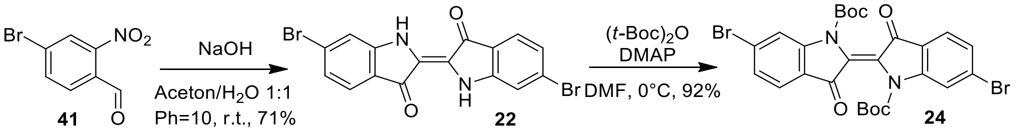

Scheme 3. 10: Synthetic route for t-Boc protected Tyrian Purple ***24****.*

Since deprotection of the Boc group was found to occur at temperatures higher than 90° C, a low-temperature protocol for the Stille cross-coupling was developed, employing $Pd_2(dba)_3$ and tri(*o*-tolyl)phosphine to generate the active catalytic species, which allowed performing several Stille reactions on compound **24** at 50° C with no Boc deprotection taking place.

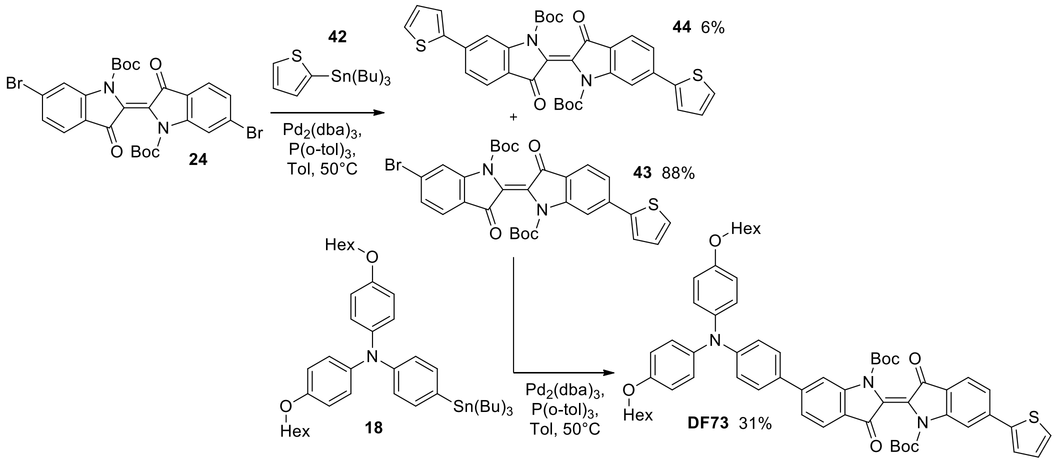

Scheme 3. 11: ***First synthetic route for the desymmetrization of the Indigo core:*** *the general procedure for low-temperature Stille cross coupling was used to introduce firstly the thiophene and secondly the triarylamine moiety.*

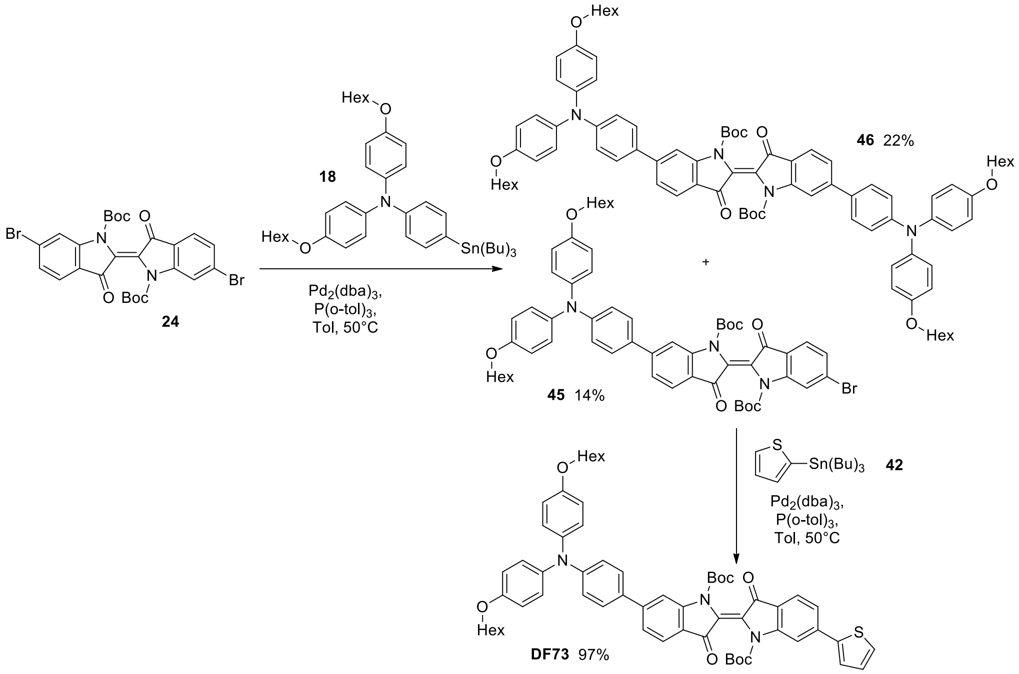

Scheme 3. 12: ***Second synthetic route for the desymmetrization of the Indigo core:*** *the general procedure for low-temperature Stille cross coupling was used to introduce firstly the triarylamine and secondly the thiophene moiety.*

In order to perform the desymmetrization of the indigo core **24** and thus control the introduction of a single triarylamine moiety on the scaffold, a careful optimization of the reaction conditions was necessary, as reported in *Scheme 3.11* and *Scheme 3.12*.

When the Stille reaction was carried out with a sub-stoichiometric amount (0.8 eq.) of commercially available thienylstannane **42**, the desired mono-substituted product **43** was obtained in 88% yield while the formation of the double cross-coupling species **44** was minimized. (*Scheme 3.11*) On the other hand, the desymmetrization carried out under the same conditions but using substituted diphenylamine stannane **18** proceeded very differently, producing a large amount of double substitution compound **46** and reducing the yield of desired product **45** to 14%. (*Scheme 3.12*) Such behavior is probably the result of the much higher solubility of mono-coupling product **45** compared both to starting material **24** and monobromide **43**, that makes it more prone to further react with the stannane in solution. In the case of compound **43**, bearing only an additional thiophene ring, the solubility was not improved very much compared to **24**, and double cross-coupling could be avoided simply by shortening the reaction time.

The second cross-coupling reaction on substrates **43** and **45** was carried out *via* an established Stille protocol, using an excess of the required stannane. Conversion of intermediate **45** took place with almost quantitative yield, (*Scheme 3.11*) while in the case of intermediate **43** the transformation appeared much less efficient. (*Scheme 3.12*) Nevertheless, combining the yields of both steps it resulted that the latter synthetic pathway was the most efficient, giving the desired final compound **DF73** with 22% yield. Furthermore, it should be mentioned that almost 12% of the starting material **24** was always recovered from the first step and could be used for further reactions.

The same synthetic pathway was also applied to the preparation of the analogous compound bearing a ProDOT (propylenedioxythiophene) spacer instead of thiophene (**DF77**, *Scheme 3.13*). Synthesis of such compound was undertaken since ProDOT was found to be an excellent building block for D-π-A dyes[101] thanks to its high electron density and its bulky substituents, efficiently preventing dye aggregation.[101,102] ProDOT (**49**) was prepared in modest yield *via* transeterification of 3,4-dimenthoxythiophene, (*Scheme 3.13*) and the corresponding stannane **50** was obtained in 66% yield simply *via* lithiation and transmetallation. In view of the results obtained in the synthesis of compound **DF73** (see above), the preparation of compound **DF77** started with the coupling with ProDOT stannane **50**, followed by the introduction of the donor moiety by reaction with stannane **18**. In both instances, reactions proceeded with low yields: in the first case, this was due to the production of a large amount of symmetric compound **52**, probably because of the increased solubility of product **51** as a consequence of the presence of the ProDOT alkyl chains; in the second step it was not possible to achieve high conversion of the reagent and the purification procedure required to resolve the complex mixture, drastically reduced the amount of product isolated.

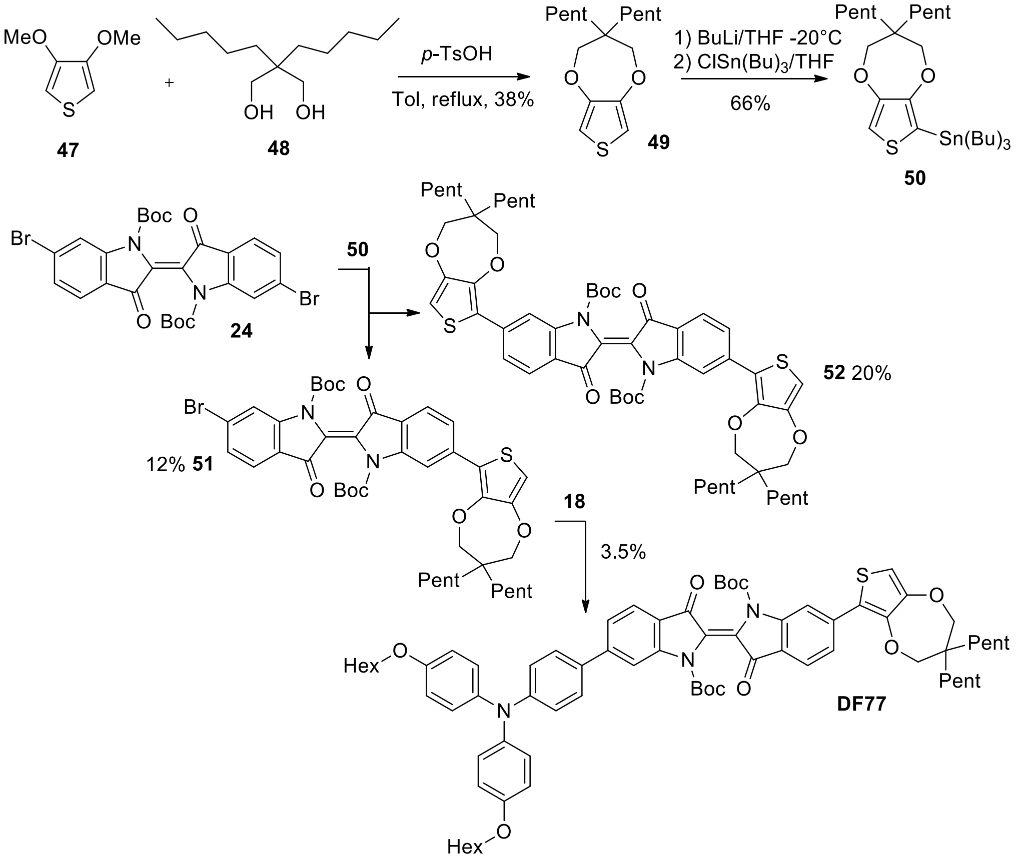

Scheme 3. 13: Synthesis of ProDOT and the corresponding stannane ***50****. Synthetic route for the desymmetrization of the indigo core with ProDOT π-spacer* ***DF77****.*

At this stage, donor-acceptor-π-bridge scaffolds **DF73** and **DF77** were subjected to formylation of the thiophene 2-position, which was required to introduce the anchoring group in a subsequent step. First, a lithiation at –50° C was attempted, followed by quench with DMF, with no success. Subsequently, activation of thiophene 2-position was investigated by means of electrophilic bromination with NBS, but that proved unsuccessful as well. Finally, formylation on the desired position was attempted *via* treatment with the Vilsmeier–Haack reagent, but the only result was Boc deprotection. (*Scheme 3.14*) Such lack of reactivity could be due to deactivation of the thiophene ring by conjugation with the indigo electron-withdrawing moiety; therefore, the synthetic pathway should be revisited towards incorporation of the formyl function on thiophene prior or during cross-coupling, for example by employing a 2-formyl-5-stannylthiophene derivative instead of stannane **42** for the functionalization of intermediate **24**.

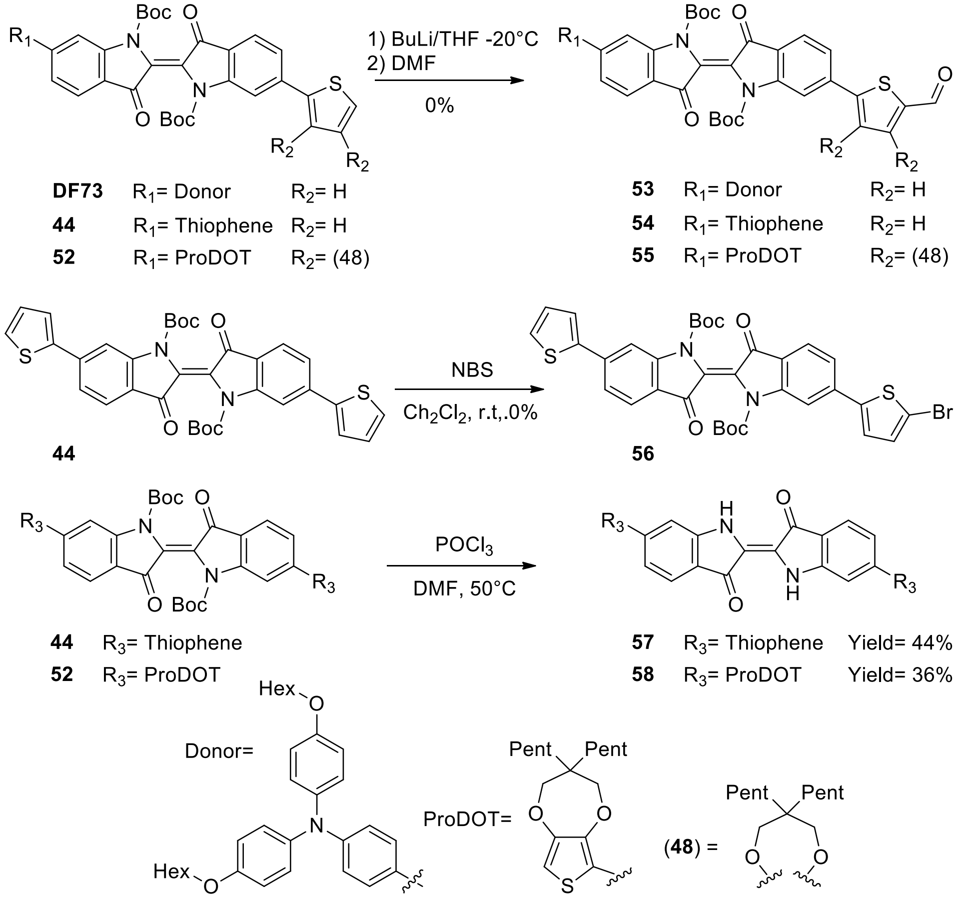

Scheme 3. 14: Attempts to perform formylation on the obtained D-A-π scaffolds.

3.3.2.2. Spectroscopic characterization

UV-Vis analysis was carried out on the synthesized compounds aiming to assign their absorption bands to specific transitions. The first category of compounds to be analyzed was that of bay-annulated derivatives. Unfortunately, Indigo **21**, BAI **23** and also Tyrian Purple **22** could not be completely dissolved in the solvent chosen for the analysis, but rather gave a suspension. Thus, the reported concentrations represent only approximate values, and an exact evaluation of molar absorptivities was not possible. Nevertheless, from *Figure 3.20* it is clear that transforming the Indigo "H-chromophore" in a new structure (**23**), the transition around 600 nm is blue-shifted and weakened, while the band in the UV region below 450 nm becomes more intense. Such structural modification is, therefore, to be considered responsible for the loss of the typical blue coloration of Indigo, making bay-annulated derivative **23** a red compound.

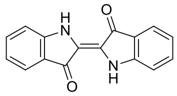

21

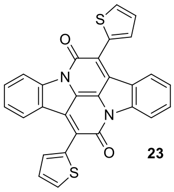

23

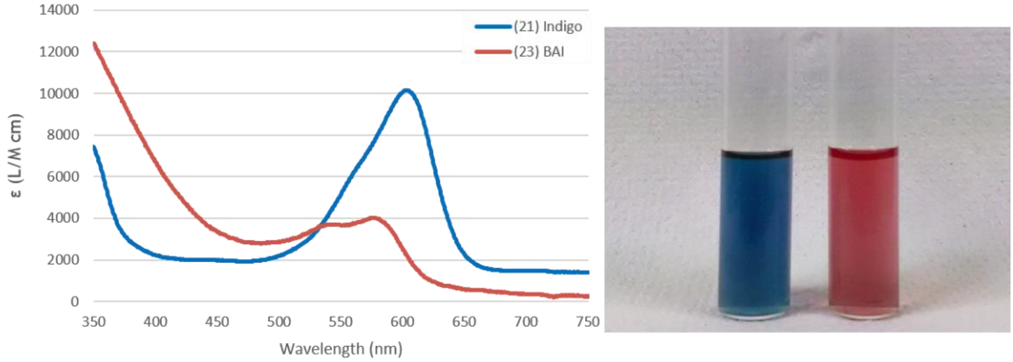

*Figure 3. 20: UV-Vis absorption spectra for Indigo (**21**) and BAI (**23**). In the picture from left to right: 6.5×10^{-4} M Indigo/CHCl$_3$ mixture and 3.0×10^{-4} M BAI/CHCl$_3$ mixture.*

Introduction of *tert*-butyl groups on the indigo core produced soluble compound **39**, and the same result was obtained by Boc protection of the amine functions, as observed for the Boc protected Tyrian Purple **24**. It's worth noting that, upon alkyl substitution of the aromatic rings, the long-wavelengths absorption responsible for the blue coloration is not lost, as long as the amine is unprotected. (*Figure 3.21*)

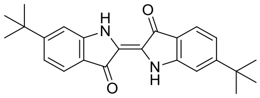

39

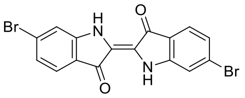

22

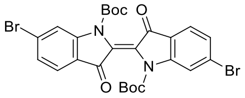

24

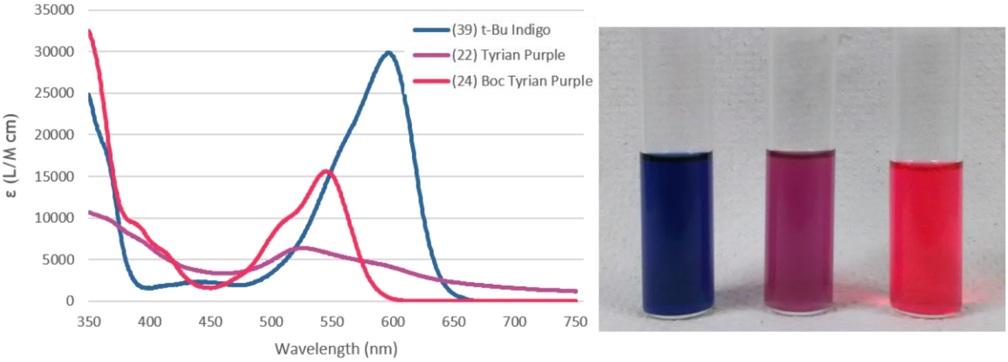

Figure 3. 21: UV-Vis absorption spectra for **39**, **24** *and Tyrian Purple (***22***). In the picture from left to right:* 4.0×10^{-4} *M* **39***/CH_2Cl_2 solution,* 4.0×10^{-4} *M Tyrian Purple/$CHCl_3$ mixture and* 4.5×10^{-4} *M* **24***/CH_2Cl_2 solution.*

Boc protected symmetric compound **44** has not any intense absorption in the yellow-red part of the spectrum; conversely, non-symmetrical D-A-π species **DF73** is characterized by a broad absorption band with the maximum around 550 nm, probably due to intramolecular charge transfer from the donor to the EWG Indigo core. (*Figure 3.22*) Release of the Boc protection from compound **44** yields elongated indigo structure **57**, that displays a good solubility and surprisingly shows an intriguing green coloration. The latter is the result of two absorption bands with similar intensity, the first around 450 nm attributable to the charge transfer from the thiophene to the EWG Indigo, and the second centered at 600 nm relative to the released "H-chromophore". A similar behavior was observed for the indigo structures modified with ProDOT. (*Figure 3.23*) As expected in this case the compounds were largely soluble thanks to their additional alkyl chains. Due to ProDOT stronger electron-donating ability compared to simple thiophene, the UV-Vis spectrum of symmetric compound **52** presents a more intense absorption than that of **44**. ProDOT-bearing non-symmetrical compound **DF77** showed only a slightly enhanced absorption intensity compared to symmetrical species **52**, as opposed to what was found for the corresponding thiophene derivatives **44** and **DF73**.

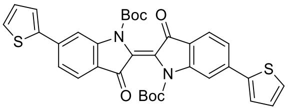

44

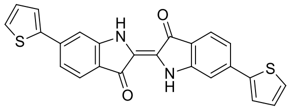

57

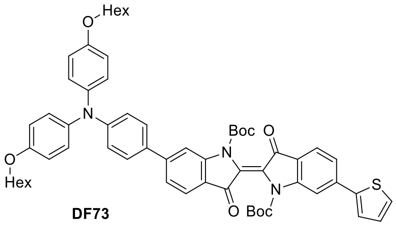

DF73

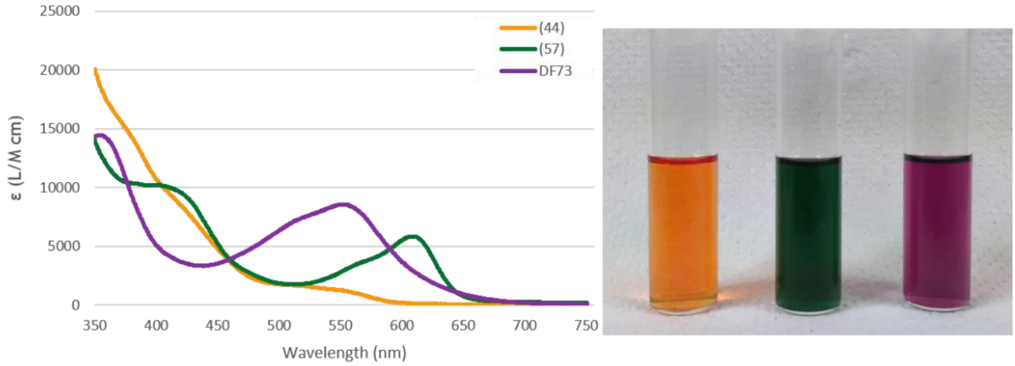

*Figure 3. 22: UV-Vis absorption spectra for **44**, **57** and **DF73**. In the picture from left to right: 5.0×10^{-4} M **44**/CH$_2$Cl$_2$ solution, 6.8×10^{-4} M **57**/CH$_2$Cl$_2$ solution and 2.3×10^{-4} M **DF73**/CH$_2$Cl$_2$ solution.*

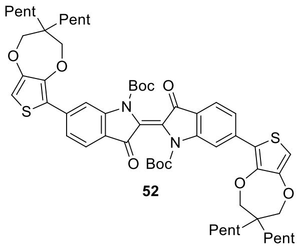

52

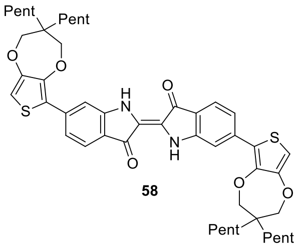

58

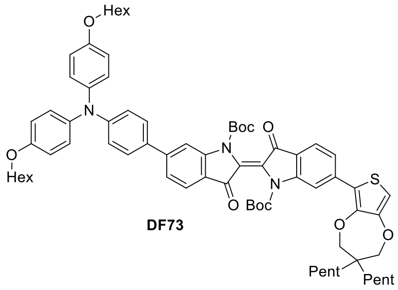

DF73

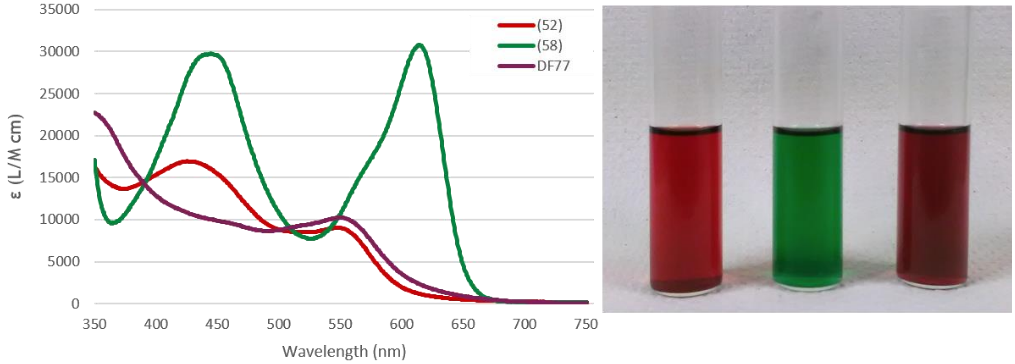

*Figure 3. 23: UV-Vis absorption spectra for **52**, **58** and **DF77**. In the picture from left to right: 5.2×10^{-4} M **52**/CH$_2$Cl$_2$ solution, 5.3×10^{-5} M **58**/CH$_2$Cl$_2$ solution and 3.5×10^{-4} M **DF77**/CH$_2$Cl$_2$ solution.*

Also, in this case, release of the free amino function in the Indigo core yielding compound **58**, restored the transition at 600 nm due to the "H-chromophore", the double intense absorption displayed by compound **58** results in intense green coloration of its solution.

These preliminary results demonstrate the possibility to reactivate an intense absorption band of the sensitizer in the long wavelength range, simply by thermal Boc deprotection. By combining the restored absorption band around 600 nm with the enhanced one at 450 nm, a brilliant green color is obtained, making Indigo derivatives good candidates for the preparation of uncommon green organic sensitizers for DSSCs.

3.3.2.3. Experimental section

General procedure A: synthesis of the indigo core[98]

The required nitro-benzaldehyde (4.52 mmol, 1.0 eq.) was dissolved in acetone (45 mL), then water (50 mL) was added slowly under vigorous stirring. A 2.0 M NaOH aqueous solution was added dropwise under vigorous stirring until the reaction mixture reached pH = 10, causing the formation of a dark precipitate. The reaction mixture was stirred at room temperature in an open flask overnight. The mixture was filtered and the resulting solid was washed with water (20 mL) and acetone (10 mL), and then dried to afford the pure product as a dark solid.

General procedure B: bay-annulation of Indigo core[97]

The appropriate indigo derivative (1.9 mmol, 1.0 eq.) was suspended in dry xylene (23.5 mL), then the solution was heated to reflux. The required thiophenyl acetyl chloride (7.6 mmol, 4 eq.) was dissolved in dry xylene (2.5 mL) and added dropwise to the boiling suspension of indigo. The reaction mixture was stirred at reflux temperature overnight. The mixture was cooled down to room temperature and filtered; the resulting solid was washed with hexane (20 mL) and recrystallized from boiling xylene to afford the pure product as a dark solid.

General procedure C: low-temperature Stille cross-coupling

The required stannane (0.08 mmol, 1.0 eq.) was dissolved in dry toluene (4 mL), previously deoxygenated by means of the "freeze-pump-thaw" procedure. The solution was further purged with nitrogen for 1h. $Pd_2(dba)_3$ (0.004 mmol, 0.05 eq.) and $P(o\text{-}Tol)_3$ (0.008 mmol, 0.1 eq.) were dissolved in dry oxygen-free toluene (4 mL), the resulting solution was left under stirring for 15 min, then the di-bromine indigo derivate (0.08 mmol, 1.0 eq.) was added and the mixture was stirred at room temperature for additional 15 min. Finally, the stannane solution was added and the reaction mixture was warmed up to 50° C and left under stirring. The reaction was monitored by TLC and lasts from 1h to 16h depending on the substrates and the degree of double substitution. The mixture was cooled down to room temperature, the solvent was removed by rotatory evaporation, and the crude was purified by flash column chromatography.

General procedure D: reaction with Vilsmeier–Haack reagent

The thiophene-containing substrate (0.08 mmol, 1.0 eq.) and $POCl_3$ (0.24 mmol, 3.0 eq.) were separately dissolved in dry DMF (0.5 mL) and the solutions were cooled down to 0° C before mixing them. The resulting reaction mixture was heated to 50° C and stirred overnight. The solution was cooled down to 0° C and quenched with 1M NaOH aq. solution (2 mL). The resulting mixture was extracted with EtOAc (2 × 10 mL) and the organic phase was washed with water (2 × 10 mL) and brine (10 mL). The combined organic phases were dried over Na_2SO_4 and the solvent was removed under reduced pressure. The crude product was purified by flash column chromatography.

Synthesis of Indigo (21)

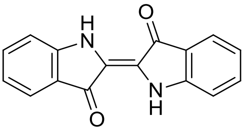

Indigo (**21**) was prepared following general procedure A, using 2-nitrobenzaldehyde (**27**, 7.0 g, 46.3 mmol). A dark blue amorphous solid was recovered (2.6 g, 9.9 mmol, 43% yield).

Synthesis of bay-annulated Indigo BAI (23)

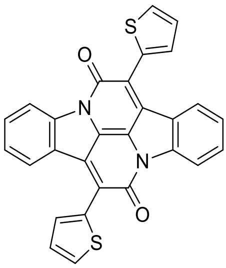

Compound **23** was prepared following general procedure B, employing Indigo (**21**, 0.500 g, 1.90 mmol) and 2-(thiophen-2-yl)acetyl chloride (**28**, 1.23g, 7.6 mmol) . A violet amorphous solid was recovered (0.758 g, 1.60 mmol, 84% yield).

(**23**): ^{1}H-NMR (200 MHz, CDCl$_3$) δ_H = 8.58 (1 H, d, *J* = 8.6 Hz), 8.18 (1 H, d, *J* = 8.2 Hz), 7.75 (1 H, d, *J* = 3.9 Hz), 7.71 (1 H, d, *J* = 4.9 Hz), 7.54 - 7.66 (1 H, m), 7.11 - 7.14 (1 H, m), 6.98 - 7.03 (1 H, m) ppm. MS (ESI) *m/z* calculated for $C_{28}H_{14}N_2O_2S_2$: 474.05. Found: 474.17 $[M]^+$

Synthesis of 2,2,2-trichloro-1-(4-hexylthiophen-2-yl)ethanol (30)[103]

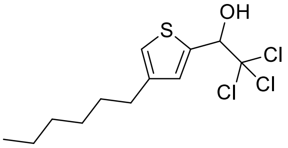

4-hexylthiophene-2-carbaldehyde (**29**, 0.502 g, 2.60 mmol, 1.0 eq.) was dissolved in DMF (1.6 mL) and $CHCl_3$ (0.464 mL, 5.81 mmol, 2.25 eq.) was added. The solution was cooled to –8° C, then a 5M NaOH solution in methanol (0.720 mL, 3.63 mmol, 1.4 eq.) was added dropwise. The resulting solution was stirred at –8° C for 15 minutes, then it was warmed to room temperature and left under stirring for an additional hour. The reaction mixture was diluted with toluene (4 mL), quenched with 1M HCl aq. solution (4 mL) and stirred overnight. The organic phase was diluted with EtOAc and washed with water (2 × 20 mL) and brine (10 mL). The organic phase was dried over Na_2SO_4, then the solvent was removed under reduced pressure and the crude product purified by flash column chromatography (PE/EtOAc 50:1 to 20:1). A colorless liquid was recovered (0.734 g, 2.32 mmol, 89% yield).

(**30**): ^{1}H-NMR (200 MHz, CDCl$_3$) δ_H = 9.87 (1 H, d, *J* = 1.1 Hz), 7.61 (1 H, d, *J* = 1.5 Hz), 7.37 (1 H, s), 2.64 (2 H, t, *J* = 7.7 Hz), 1.53 - 1.72 (2 H, m), 1.26 - 1.36 (6 H, m), 0.84 - 0.93 (3

H, m) ppm. ^{13}C-NMR{^{1}H} (100 MHz, $CDCl_3$) δ_C = 144.8, 143.7, 136.9, 130.2, 114.9, 101.0, 31.5, 30.3, 30.1, 28.8, 22.5, 14.0 ppm.

Synthesis of 2-(4-hexylthiophen-2-yl)acetic acid (31)[103]

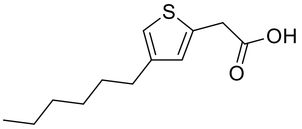

Diphenyl diselenide (Ph_2Se_2 0.752 g, 2.4 mmol, 1.05 eq.) was dissolved in dry EtOH (5 mL), previously purged with nitrogen for 1h, and $NaBH_4$ (0.186 g, 4.8 mmol, 2.1 eq.) was added slowly to the solution, causing gas release. The solution was stirred at room temperature for 15 minutes, then a solution of compound **30** (0.731 g, 2.3 mmol, 1.0 eq.) in dry and deoxygenated EtOH (2 mL) was added. Finally, a 2 M NaOH solution in dry and deoxygenated EtOH (1.9 mL, 3.8 mmol, 6.0 eq.) was added and the mixture was left under stirring at room temperature overnight. The reaction mixture was diluted with EtOAc (10 mL) and quenched by dropwise addition of a 3M HCl aq. solution until the pH of the aqueous layer was below 2. The organic phase was separated and washed with brine (20 mL) and then dried over Na_2SO_4. The solvent was removed under reduced pressure and the crude product purified by flash column chromatography (pure PE than PE/EtOAc 20:1 to 1:1 then PE/EtOAc/acetic acid 1:1:0.01). Ph_2Se_2 was partly recovered as well as starting material **30**, while the desired product **31** was obtained as a pale yellow oil (93 mg, 0.41 mmol, 18% yield).

(**31**): ^{1}H-NMR (200 MHz, $CDCl_3$) δ_H = 6.73 - 6.89 (2 H, m), 3.84 (2 H, s), 2.56 (2 H, t, *J* = 8.1 Hz), 1.50 - 1.69 (2 H, m), 1.27 - 1.39 (6 H, m), 0.84 - 0.96 (3 H, m) ppm. ^{13}C-NMR{^{1}H} (50 MHz, $CDCl_3$) δ_C = 173.5, 146.2, 143.3, 128.7, 119.7, 35.1, 31.7, 30.5, 30.3, 29.0, 22.6, 14.0 ppm.

Synthesis of 2-(4-hexylthiophen-2-yl)acetyl chloride (32)[103]

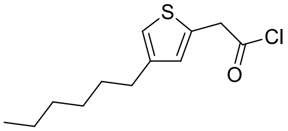

Carboxylic acid **31** (28 mg, 0.124 mmol, 1.0 eq.) was dissolved in dry CH_2Cl_2 (1 mL), and oxalyl chloride (0.012 mL, 0.149 mmol, 1.2 eq.) was added. One drop dry DMF was added to the solution and the reaction mixture was stirred at room temperature for 1h. The solvent was removed under reduced pressure to give crude product **32** as a light yellow oil (30 mg, 0.124 mmol, yield 100%), which was used as such for the following reaction.

(**32**): ^{1}H-NMR (200 MHz, CDCl$_3$) δ_H = 7.12 – 7.25 (1 H, m), 6.33 - 6.47 (1 H, m), 4.08 (2 H, s), 2.84 (2 H, t, *J* = 7.6 Hz), 1.62 - 1.76 (2 H, m), 1.37 - 1.57 (6 H, m), 0.87 – 1.02 (3 H, m) ppm.

Synthesis of (4-(*tert*-butyl)phenyl)methylene diacetate (35)

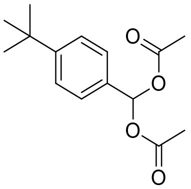

4-(*tert*-Butyl)benzaldehyde (**34**, 250 mg, 1.54 mmol, 1.0 eq.) was dissolved in distilled acetic anhydride (0.5 mL), then *p*-toluenesulfonic acid monohydrate (28 mg, 0.15 mmol, 0.1 eq.) was added. The solution was stirred at room temperature for 30 minutes then it was diluted with CH$_2$Cl$_2$ (5 mL) and washed with a saturated aq. solution of NaHCO$_3$ (10 mL), followed by water (2 × 10 mL). The combined organic phases were dried over Na$_2$SO$_4$. The solvent was removed under reduced pressure and the crude product (838 mg, 1.44 mmol, 92% yield) was used for the following step without further purification.

(**35**): ^{1}H-NMR (200 MHz, CDCl$_3$) δ_H = 7.66 (1 H, s), 7.43 – 7.45 (4 H, m), 2.12 (6 H, s), 1.32 (9 H, s) ppm. ^{13}C-NMR{^{1}H} (100 MHz, CDCl$_3$) δ_C = 168.4, 148.4, 140.1, 125.6, 126.3, 98.2, 45.2, 31.5, 21.2 ppm.

Synthesis of (4-(tert-butyl)-2-nitrophenyl)methylene diacetate (36)

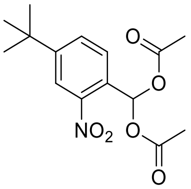

Diacetate **35** (3.251 g, 12.3 mmol, 1.0 eq.) was dissolved in distilled acetic anhydride (7.0 mL), the solution was cooled at 6° C, then white fuming HNO$_3$ 98% (3.2 mL, 73.8 mmol, 6.0 eq.) was added keeping the temperature below 10° C. The solution was stirred at 13° C overnight, then warmed to room temperature and quenched with water (150 mL). The mixture was extracted with EtOAc (2 × 50 mL) and the combined organic phases were dried over Na_2SO_4. The solvent was removed under reduced pressure and the crude product purified by flash column chromatography (PE/EtOAc 25:1 to 10:1). 1-(*tert*-butyl)-4-nitrobenzene (0.28g, 1.5 mmol) was obtained, and the desired product **36** was obtained (1.060 g, 3.43 mmol, 28% yield) in almost equal amount to its isomer (4-(*tert*-butyl)-3-nitrophenyl)methylene diacetate **37** (0.909 g, 2.94 mmol, 24% yield).

(**36**): ^{1}H-NMR (400 MHz, $CDCl_3$) δ_H = 8.15 (1 H, s), 8.04 (1 H, d, *J* = 1.9 Hz), 7.68 (1 H, d, *J* = 1.9 Hz), 7.64 (1 H, s), 2.13 (6 H, s), 1.35 (9 H, s) ppm. ^{13}C-NMR{^{1}H} (100 MHz, $CDCl_3$) δ_C = 168.3, 154.6, 147.7, 130.6, 129.0, 127.6, 122.1, 86.2, 35.1, 30.9, 20.5 ppm.

Synthesis of 4-(*tert*-butyl)-2-nitrobenzaldehyde (38)

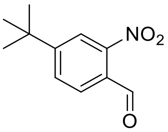

Deprotection of compound **36** (0.952 g, 3.01 mmol, 1.0 eq.) was performed by dissolving it in THF (6 mL) and adding a 1M NaOH aq. solution (12 mL, 12.00 mmol, 4.0 eq.). The solution was stirred room temperature for 2h, then was diluted with dichloromethane (10 mL) and the organic phase was extracted with water (20 mL). The organic phase was dried over Na_2SO_4. The solvent was removed under reduced pressure and the crude product (0.592 g, 2.86 mmol, 93% yield) was used as such for the subsequent reaction.

(**38**): ^{1}H-NMR (400 MHz, $CDCl_3$) δ_H = 10.39 (1 H, d, *J* = 0.8 Hz), 8.10 (1 H, d, *J* = 2.0 Hz), 7.92 (1 H, d, *J* = 8.0 Hz), 7.80 (1 H, ddd, *J* = 8.2, 2.0, 0.6 Hz), 1.41 (9 H, s) ppm. ^{13}C-NMR{^{1}H} (100 MHz, $CDCl_3$) δ_C = 189.4, 161.6, 157.8, 134.9, 130.9, 129.8, 124.8, 36.4, 30.5 ppm. MS (ESI) *m*/*z* calculated for $C_{11}H_{13}NO_3$: 207.09. Found: 208.4 [M+1]$^+$.

Synthesis of 6,6'-di-tert-butyl-indigo (39)

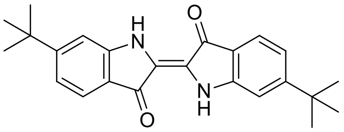

Compound **38** (0.592 g, 2.86 mmol) was treated according to general procedure A. Since no precipitation of the product occurred, the mixture was extracted with CH_2Cl_2 (2 × 30 mL) and the combined organic phases were dried over Na_2SO_4. The solvent was removed under reduced pressure and the crude product purified by flash column chromatography (CH_2Cl_2/PE 10:1). A blue amorphous solid was recovered (92 mg, 0.25 mmol, 17% yield).

(**39**): ^{1}H-NMR (200 MHz, $CDCl_3$) δ_H = 8.95 (2 H, s), 7.66 (2 H, d, *J* = 8.4 Hz), 6.96 - 7.09 (4 H, m), 1.34 (18 H, s) ppm. ^{13}C-NMR{^{1}H} (100 MHz, $CDCl_3$) δ_C = 188.2, 161.0, 152.6, 124.0, 122.0, 118.7, 109.0, 57.9, 35.8, 31.0 ppm. MS (ESI) *m/z* calculated for $C_{35}H_{39}N_3O_5$: 581.29. Found: 582.1 $[M+1]^+$

Synthesis of 3,10-di-*tert*-butyl-7,14-di(thiophen-2-yl)diindolo[3,2,1-de:3',2',1'-ij][1,5]naphthyridine-6,13-dione (40)

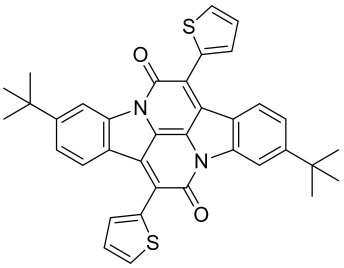

Indigo derivate **39** (30 mg, 0.08 mmol) was subjected to general procedure B with 2-(thiophen-2-yl)acetyl chloride **28** (52 mg, 0.32 mmol). Since no precipitate was recovered, the reaction mixture was extracted with EtOAc (2 × 50 mL) and the combined organic phases were dried over Na_2SO_4. The solvent was removed under reduced pressure and the crude product purified by preparative TLC (PE/EtOAc 10:1). Desired product **40** was isolated as a red-violet amorphous solid (4 mg, 0.007 mmol, 9% yield).

(**40**): ^{1}H-NMR (200 MHz, $CDCl_3$) δ_H = 8.67 (2 H, d, *J* = 1.5 Hz), 8.08 (2 H, d, *J* = 8.6 Hz), 7.67 - 7.76 (4 H, m), 7.32 - 7.47 (4 H, m), 1.41 (18 H, s) ppm. MS (ESI) *m/z* calculated for $C_{36}H_{30}N_2O_2S_2$: 586.17. Found: 587.21 $[M+1]^+$.

Synthesis of Tyrian Purple (22)

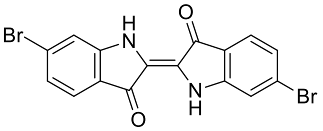

4-bromo-2-nitrobenzaldehyde (**27**, 1.00 g, 4.35 mmol) was treated according to general procedure A. Desired product **22** was obtained as a red amorphous solid (0.647 g, 1.54 mmol, 71% yield).

Synthesis of Boc-protected Tyrian Purple (24)

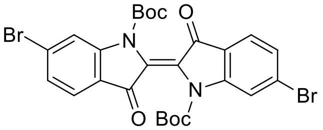

Tyrian Purple (**22**, 0.638 g, 1.52 mmol, 1.0 eq.) was suspended in DMF (12 mL) and the solution was cooled to 0° C. Di-*tert*-butyl dicarbonate (1.658 g, 7.60 mmol, 5.0 eq.) and *N,N*-dimethylpyridin-4-amine (0.111 g, 0.91 mmol, 0.6 eq.) were added. The solution was stirred at room temperature for 2h, during which it turned deep red and released gasses very smoothly. The reaction mixture was cooled down to 0° C, the product was filtered off and washed with DMF/H_2O 1:1 (5 mL), then dried under vacuum. Desired product **24** was obtained as a pink amorphous solid (0.873 g, 1.40 mmol, 92% yield) without the need of any further purification. (**24**): ^{1}H-NMR (200 MHz, $CDCl_3$) δ_H = 8.26 (2 H, br. s), 7.62 (2 H, d, *J* = 8.4 Hz), 7.37 (2 H, dd, *J* = 8.1, 1.5 Hz), 1.61 (18 H, s) ppm. ^{13}C-NMR{^{1}H} (50 MHz, $CDCl_3$) δ_C = 186.2, 148.3, 135.3, 133.2, 128.4, 125.7, 120.2, 118.8, 84.3, 28.4 ppm.

Synthesis of di-*tert*-butyl-6-bromo-3,3'-dioxo-6'-(thiophen-2-yl)-[2,2'-biindolinylidene]-1,1'-dicarboxylate (43)

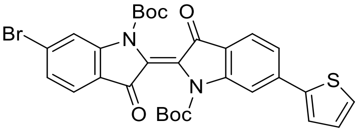

Boc-protected Tyrian Purple (**24**, 0.140 g, 0.22 mmol, 1.0 eq.) and tributyl(thiophen-2-yl)stannane (**42**, 0.066 g, 0.18 mmol 0.8 eq.) were treated according to general procedure C. The crude product was purified by flash column chromatography

(PE/EtOAc 50:1 to 10:1). The product **43** was obtained as a red amorphous solid (96 mg, 0.15 mmol, 70% yield) that was converted in red crystals by biphasic recrystallization in CH_2Cl_2 and Hex. A residual amount of reactant **43** was collected (17 mg, 0.026 mmol, 12% recovery), as well as the product of double cross coupling **44** (8 mg, 0.013 mmol, 6% recovery)

(**43**) : ^{1}H-NMR(200 MHz, $CDCl_3$) δ_H = 8.40 (1 H, d, *J* = 0.7 Hz), 8.32 (1 H, s), 7.85 (1 H, d, *J* = 7.7 Hz), 7.77 (1 H, d, *J* = 8.1 Hz), 7.39 - 7.48 (3 H, m), 7.12 - 7.18 (2 H, m), 1.54 (18 H, s) ppm. ^{13}C-NMR{^{1}H} (50 MHz, $CDCl_3$) δ_C = 182.6, 149.9, 149.7, 143.5, 141.7, 128.6, 127.2, 125.5, 124.7, 121.9, 121.7, 113.6, 84.7, 28.3 ppm. MS (ESI) *m*/*z* calculated for $C_{30}H_{27}BrN_2O_6S$: 622.08. Found: 623.25 [M+1]$^+$.

(**44**): ^{1}H-NMR (200 MHz, $CDCl_3$) δ_H = 8.32 (2 H, d, *J* = 1.1 Hz), 7.77 (2 H, d, *J* = 8.1 Hz), 7.48 (2 H, dd, *J* = 8.1, 1.5 Hz), 7.52 (2 H, dd, *J* = 3.7, 1.1 Hz), 7.42 (2 H, dd, *J* = 5.1, 1.1 Hz), 7.15 (2 H, dd, *J* = 5.1, 3.7 Hz), 1.69 (18 H, s) ppm. ^{13}C-NMR{^{1}H} (50 MHz, $CDCl_3$) δ_C = 182.6, 149.9, 149.7, 143.5, 141.7, 128.5, 127.2, 125.4, 124.7, 121.9, 121.7, 113.6, 84.6, 28.2 ppm. MS (ESI) m/z calculated for $C_{34}H_{30}N_2O_6S_2$: 626.15. Found: 1275.20 [2M+Na]$^+$.

Synthesis of di-tert-butyl 6-(4-(bis(4-(hexyloxy)phenyl)amino)phenyl)-6'-bromo-3,3'-dioxo-[2,2'-biindolinylidene]-1,1'-dicarboxylate (45)

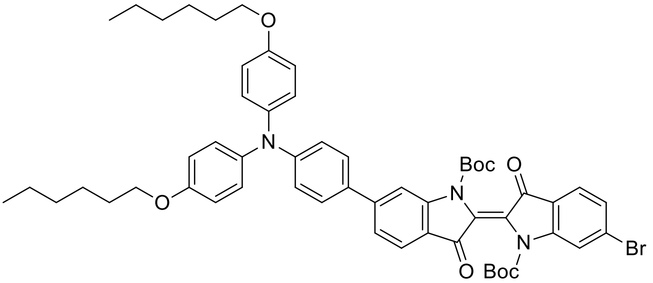

Boc protected Tyrian Purple (**24**, 0.187 g, 0.3 mmol, 1.0 eq.) and 4-tributylstannyl-*N*,*N*-bis(4-(hexyloxy)phenyl)aniline (**18**, 0.220 g, 0.3 mmol, 1.0 eq.) were treated according to general procedure C. The crude reaction mixture was enriched in the products by precipitating reagent **24** from hexanes, and was purified by flash column chromatography (PE/EtOAc 50:1 to 10:1). Product **45** was obtained as a red-purple amorphous solid (40 mg, 0.032 mmol, 14% yield). Starting material **24** was partly recovered (87 mg, 0.14 mmol, 47% recovery) as well as the product of double cross coupling **46** (89 mg, 0.066 mmol, 22% recovery)

(**45**): ^{1}H-NMR (200 MHz, CDCl$_3$) δ_H = 8.21 - 8.42 (2 H, m), 7.73 - 7.88 (1 H, m), 7.59 - 7.73 (1 H, m), 7.44 - 7.54 (2 H, m), 7.36 - 7.44 (2 H, m), 7.05 - 7.17 (4 H, m), 6.94 - 7.04 (2 H, m), 6.80 - 6.93 (4 H, m), 3.96 (4 H, t, *J* = 6.2 Hz), 1.72 - 1.84 (4 H, m), 1.62 (18 H, d, *J* = 1.8 Hz), 1.45 - 1.55 (12 H, m), 0.92 (6 H, t, *J* = 6.8 Hz) ppm. ^{13}C-NMR{^{1}H} (50 MHz, CDCl$_3$) δ_C = 156.1, 149.8, 149.5, 149.0, 140.1, 130.9, 130.7, 130.5, 129.0, 128.4, 128.0, 127.2, 124.8, 124.5, 122.5, 122.0, 120.9, 120.2, 119.6, 115.5, 113.9, 84.9, 84.5, 68.4, 31.6, 29.3, 28.2, 28.1, 25.8, 22.6, 14.0 ppm. MS (ESI) *m/z* calculated for $C_{56}H_{63}N_3O_8$: 905.46. Found: 906.56 [M+1]$^+$.

(**46**): ^{1}H-NMR (200 MHz, CDCl$_3$) δ_H = 8.23 - 8.39 (2 H, m), 7.72 - 7.91 (2 H, m), 7.44 - 7.55 (4 H, m), 7.36 - 7.43 (2 H, m), 7.06 - 7.16 (8 H, m), 6.94 - 7.03 (4 H, m), 6.82 - 6.91 (8 H, m), 3.96 (8 H, t, *J* = 6.6 Hz), 1.74 - 1.85 (8 H, m), 1.62 (18 H, s), 1.47 (24 H, s), 0.88 - 0.97 (12 H, m) ppm. MS (ESI) *m/z* calculated for $C_{86}H_{100}N_4O_{10}$: 1348.74. Found: 1349.53 [M+1]$^+$.

Synthesis of di-*tert*-butyl 6-(4-(bis(4-(hexyloxy)phenyl)amino)phenyl)-3,3'-dioxo-6'-(thiophen-2-yl)-[2,2'-biindolinylidene]-1,1'-dicarboxylate (DF73) *via* intermediate 45

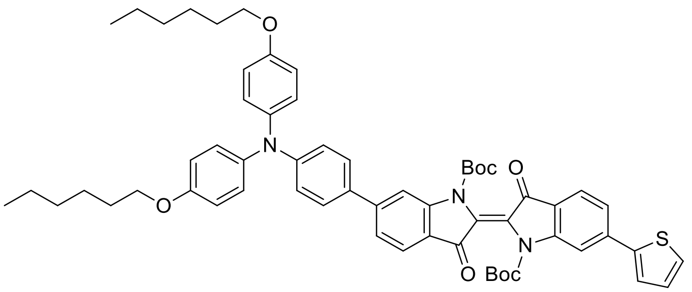

Di-*tert*-butyl-6-(4-(*bis*(4-(hexyloxy)phenyl)amino)phenyl)-6'-bromo-3,3'-dioxo-[2,2'-biindolinylidene]-1,1'-dicarboxylate (**45**, 40 mg, 0.032 mmol, 1.0 eq.) and an excess of tributyl(thiophen-2-yl)stannane (**42**, 89 mg, 0.24 mmol, 7.5 eq.) were reacted according to general procedure C. The crude product was purified by flash column chromatography (PE/EtOAc 50:1 to 10:1). Desired product **DF73** was obtained as a purple amorphous solid (30 mg, 0.031 mmol, 97% yield).

(**DF73**): ^{1}H-NMR (200 MHz, CDCl$_3$) δ_H = 8.28 (1 H, s), 7.78 (1 H, d, *J* = 8.1 Hz), 7.66 (1 H, dd, *J* = 4.8, 0.7 Hz), 7.48 - 7.55 (2 H, m), 7.43 (1 H, d, *J* = 1.5 Hz), 7.39 (1 H, d, *J* = 1.5 Hz), 7.25 - 7.31 (3 H, m), 7.21 (1 H, dd, *J* = 3.3, 0.7 Hz), 7.09 - 7.16 (4 H, m), 6.96 - 7.03 (2

H, m), 6.83 - 6.92 (4 H, m), 3.97 (4 H, t, *J* = 6.4 Hz), 1.75 - 1.86 (4 H, m), 1.64 (18 H, s), 1.48 - 1.54 (12 H, m), 0.80 - 0.85 (6 H, m) ppm. ^{13}C-NMR{^{1}H} (50 MHz, CDCl$_3$) δ_C = 156.0, 152.3, 150.2, 149.9, 149.7, 148.7, 140.2, 135.2, 131.2, 130.5, 128.0, 127.8, 127.1, 124.3, 122.3, 121.2, 119.7, 115.5, 90.6, 84.2, 77.7, 77.0, 76.4, 68.4, 31.6, 29.0, 28.2, 27.2, 25.8, 22.6, 14.0 ppm. MS (ESI) m/z calculated for $C_{60}H_{65}N_3O_8S$: 987.45. Found: 987.42 [M+1]$^+$.

Synthesis of di-*tert*-butyl-6-(4-(*bis*(4-(hexyloxy)phenyl)amino)phenyl)-3,3'-dioxo-6'-(thiophen-2-yl)-[2,2'-biindolinylidene]-1,1'-dicarboxylate (DF73) *via* intermediate 43

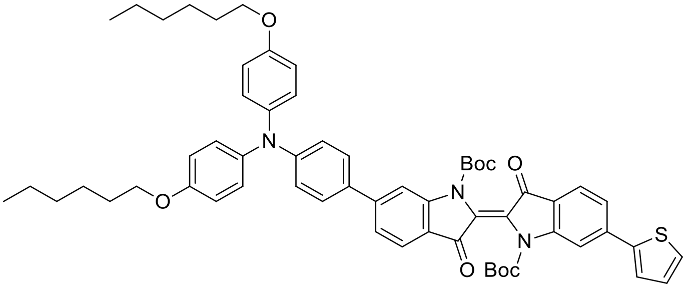

Di-*tert*-butyl-6-bromo-3,3'-dioxo-6'-(thiophen-2-yl)-[2,2'-biindolinylidene]-1,1'-dicarboxylate (**43**, 0.103 g, 0.17 mmol, 1.0 eq.) and an excess of 4-tributylstannyl-*N,N*-*bis*(4-(hexyloxy)phenyl)aniline (**18**, 0.745 g, 1.01 mmol, 6.0 eq.) were reacted according to general procedure C. The crude product was purified by flash column chromatography (PE/EtOAc 50:1 to 10:1). Desired product **DF73** was obtained as a purple amorphous solid (52 mg, 0.053 mmol, yield 31%).

Synthesis of 3,3-dipentyl-3,4-dihydro-2H-thieno[3,4-*b*][1,4]dioxepine (ProDOT, 49)[104]

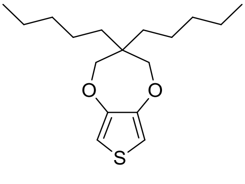

3,4-Dimethoxythiophene (**47**, 1.486 g, 11.8 mmol, 1.0 eq.) was dissolved in dry toluene (100 mL), then 2,2-dipentylpropane-1,3-diol (**48**, 5.107 g, 23.6 mmol, 2.0 eq.) and *p*-toluenesulfonic acid (0.203 g, 1.18 mmol, 0.1 eq.) were added. The solution was stirred at reflux temperature for 11h, while methanol was removed from the reaction environment by means of a Soxhlet apparatus charged with 4Å molecular sieves. After cooling down to room temperature, the solvent was removed under reduced pressure and the crude product purified by flash column chromatography (PE/EtOAc 100:1 to 5:1). Desired product **49** (1.352 g, 4.56 mmol, 38% yield) was obtained as a colorless oil. Some of the starting materials were recovered as well.

(**49**): ^{1}H-NMR (200 MHz, $CDCl_3$) δ_H = 6.42 (2 H, s), 3.86 (4 H, s), 1.22 - 1.44 (24 H, m), 0.86 - 0.94 (6 H, m) ppm. ^{13}C-NMR{^{1}H} (50 MHz, $CDCl_3$) δ_C = 149.8, 104.6, 77.5, 43.7, 32.6, 31.9, 22.5, 22.4, 14.0 ppm.

Synthesis of tributyl(3,3-dipentyl-3,4-dihydro-2H-thieno[3,4-*b*][1,4]dioxepin-6-yl)stannane (50)

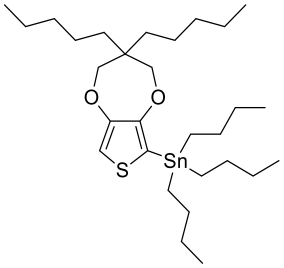

ProDOT (**49**, 1.352 g, 4.56 mmol, 1.0 eq.) was dissolved in dry THF (14 mL). The solution was cooled down to –78° C, and *n*-BuLi (1.6 M solution in hexanes, 3.2 mL, 5.5 mmol, 1.2 eq.) was added slowly. The solution was allowed to warm up to –20° C while stirring, then it was cooled down again to –78° C. Tributyltin chloride ($ClSnBu_3$ 1.778 g, 5.5 mmol, 1.2 eq.) was added and the solution was allowed to warm up to room temperature overnight while stirring. The mixture was diluted with Et_2O (20 mL) and washed with a cold saturated solution of NH_4Cl (2 × 30 mL). The solvent was removed under reduced pressure to yield crude product **50** (1.739 g, 3.0 mmol, 66% yield), which was used as such in the following transformation.

(**50**): ^{1}H-NMR (200 MHz, $CDCl_3$) δ_H = 6.67 (1 H, s), 3.75 - 3.87 (10 H, m), 1.19 - 1.74 (34 H, m), 0.76 - 1.03 (15 H, m) ppm. ^{13}C-NMR{^{1}H} (50 MHz, $CDCl_3$) δ_C = 155.7, 114.8, 111.0, 77.6, 43.8, 43.7, 32.7, 32.2, 29.0, 27.9, 27.2, 22.5, 14.0, 13.7, 10.7 ppm.

Synthesis of di-*tert*-butyl-6-bromo-6'-(3,3-dipentyl-3,4-dihydro-2H-thieno[3,4-*b*][1,4]dioxepin-6-yl)-3,3'-dioxo-[2,2'-biindolinylidene]-1,1'-dicarboxylate (51)

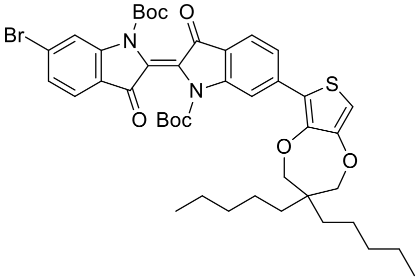

Compound **24** (0.187 g, 0.3 mmol) and tributyl(3,3-dipentyl-3,4-dihydro-2H-thieno[3,4-*b*][1,4]dioxepin-6-yl)stannane (**50**, 0.176 g, 0.3 mmol) were reacted according to general procedure C. The crude product was dissolved in hexane and the precipitated residue of compound **24** was removed. The resulting material was purified by flash column chromatography (CH_2Cl_2/PE 50:1). Desired product **51** was obtained as a red amorphous solid (28 mg, 0.037 mmol, 12% yield) along with a significant amount of double cross-coupling product **52** (64 mg, 0.06 mmol 20% yield).

(**51**): ^{1}H-NMR (200 MHz, $CDCl_3$) δ_H = 8.30 - 8.56 (1 H, m), 7.75 - 7.96 (1 H, m), 7.44 - 7.72 (2 H, m), 6.69 – 6.95 (2 H, m), 6.42 – 6.54 (1 H, m), 3.99 (2 H, s), 3.86 (2 H, s), 1.40 - 1.63 (18 H, m), 1.19 - 1.31 (16 H, m), 0.78 - 0.92 (6 H, m) ppm. MS (ESI) *m*/*z* calculated for $C_{43}H_{51}BrN_2O_8S$: 834.25. Found: 835.25 $[M+1]^+$.

(**52**): ^{1}H-NMR (200 MHz, $CDCl_3$) δ_H = 8.25 - 8.46 (2 H, m), 7.75 - 7.86 (2 H, m), 7.59 - 7.74 (2 H, m), 6.47 - 6.65 (2 H, m) , 4.03 (4 H, s), 3.95 (4 H, s), 1.43 - 1.58 (18 H, m), 1.25 - 1.37 (32 H, m), 0.88 - 0.96 (12 H, m) ppm. MS (ESI) *m*/*z* calculated for $C_{60}H_{78}N_2O_{10}S_2$: 1050.51. Found: 1051.37 $[M+1]^+$.

Synthesis of di-*tert*-butyl-6-(4-(*bis*(4-(hexyloxy)phenyl)amino)phenyl)-6'-(3,3-dipentyl-3,4-dihydro-2H-thieno[3,4-*b*][1,4]dioxepin-6-yl)-3,3'-dioxo-[2,2'-biindolinylidene]-1,1'-dicarboxylate (DF77)

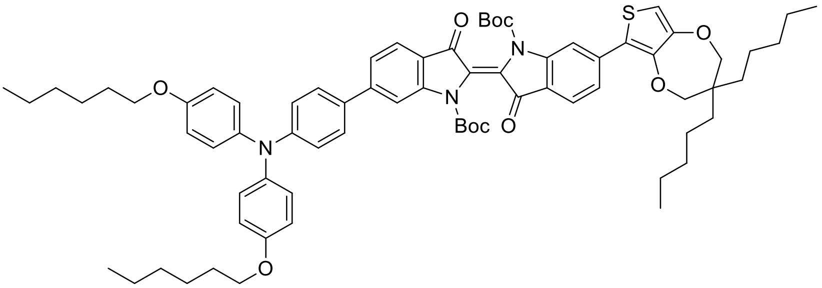

Compound **51** (52 mg, 0.07 mmol, 1 eq.) and an excess of 4-(tributylstannyl)-*N*,*N*-bis(4-(hexyloxy)phenyl)aniline (**18**, 0.334 g, 0.45 mmol, 6.5 eq.) were reacted according to general procedure C. The crude was purified by flash column chromatography (CH_2Cl_2/PE 50:1) to remove protodemetallation byproduct **16** and unreacted stannane **18**. Following preparative TLC (Tol/EtOAc 50:1) desired product **DF77** was obtained as a red amorphous solid (3 mg, 0.0025 mmol, yield 4%).

(**DF77**): ^{1}H-NMR (200 MHz, $CDCl_3$) δ_H = 8.23 - 8.32 (1 H, m), 7.69 - 7.81 (2 H, m), 7.58 - 7.66 (1 H, m), 7.45 - 7.55 (2 H, m), 7.34 - 7.43 (2 H, m), 7.06 - 7.17 (4 H, m), 6.95 - 7.03 (2 H, m), 6.81 - 6.92 (4 H, m), 6.54 (1 H, d, *J* = 1.5 Hz), 3.89 - 4.08 (8 H, m), 1.80 (4 H, dd, *J* = 7.3, 5.5 Hz), 1.58 (18 H, s), 1.29 - 1.40 (28 H, m), 0.88 - 0.96 (12 H, m) ppm. MS (ESI) *m/z* calculated for $C_{73}H_{89}N_3O_{10}S$: 1199.63. Found: 1200.46 [M+1]$^+$.

Synthesis of (*E*)-6,6'-di(thiophen-2-yl)-[2,2'-biindolinylidene]-3,3'-dione (57)

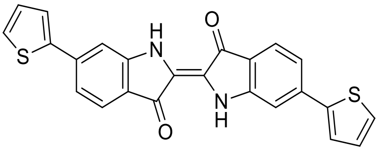

Di-*tert*-butyl-3,3'-dioxo-6,6'-di(thiophen-2-yl)-[2,2'-biindolinylidene]-1,1'-dicarboxylate (**44**, 50 mg, 0.08 mmol) was reacted according to general procedure D. The crude was purified by flash column chromatography (EP/EtOAc 35:1 to 1:1 than pure EtOAc) followed by biphasic recrystallization from $CHCl_3$ and hexane. Product **57** was obtained as a green amorphous solid (15 mg, 0.035 mmol, 44% yield).

(**57**) ^{1}H-NMR (200 MHz, $CDCl_3$) δ_H = 9.02 (2 H, br. s.), 7.61 – 7.75 (4 H, m), 7.31 – 7.48 (4 H, m), 7.13 (2 H, t, *J* = 7.9 Hz), 7.06 (2 H, s) ppm. MS (ESI) *m/z* calculated for $C_{24}H_{14}N_2O_2S_2$: 426.05. Found: 875.6 [2M+Na]$^+$.

Synthesis of 6,6'-*bis*(3,3-dipentyl-3,4-dihydro-2H-thieno[3,4-b][1,4]dioxepin-6-yl)-[2,2'-biindolinylidene]-3,3'-dione (58)

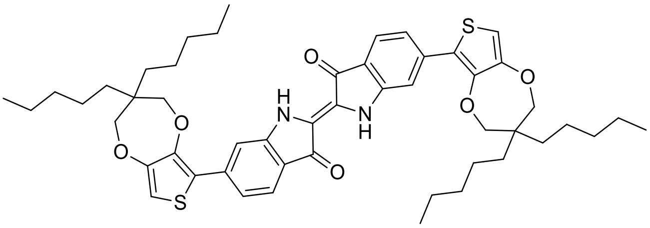

Di-*tert*-butyl-6,6'-bis(3,3-dipentyl-3,4-dihydro-2H-thieno[3,4-b][1,4]dioxepin-6-yl)-3,3'-dioxo-[2,2'-biindolinylidene]-1,1'-dicarboxylate (**52**, 31 mg, 0.026 mmol) was reacted according to general procedure D. The crude was purified by flash column chromatography (EP/EtOAc 35:1 to 1:1 than pure EtOAc) to give compound **58** as a green amorphous solid (8 mg, 0.009 mmol, yield 36%). (**58**) ^{1}H-NMR (200 MHz, $CDCl_3$) δ_H = 9.17 (2 H, br. s.), 7.61 (2 H, d, *J* = 8.1 Hz), 7.48 (2 H, s), 7.12 (2 H, d, *J* = 8.1 Hz), 6.45 (2 H, s), 3.95 (4 H, s) , 3.88 (4 H, s), 1.17 - 1.43 (32 H, m), 0.81 - 0.98 (12 H, m) ppm. ^{13}C-NMR{^{1}H} (50 MHz, $CDCl_3$) δ_C = 187.4, 152.2, 150.5, 147.9, 141.0, 124.4, 122.2, 120.6, 118.5, 118.1, 109.3, 104.6, 77.5, 65.8, 43.8, 32.7, 32.1, 22.5, 14.0 ppm. MS (ESI) m/z calculated for $C_{50}H_{62}N_2O_6S_2$: 850.40. Found: 851.78 [M+1]$^+$.

References

[1] Listorti A., O'Regan B., Durrant J. R. Electron Transfer Dynamics in Dye-Sensitized Solar Cells. *Chem. Mater.* **2011**, *23*, 3381–3399.

[2] Basheer B., Mathew D., George B. K., Reghunadhan Nair C. P. An overview on the spectrum of sensitizers: The heart of Dye Sensitized Solar Cells. *Sol. Energy* **2014**, *108*, 479–507.

[3] Ooyama Y., Harima Y. Photophysical and electrochemical properties, and molecular structures of organic dyes for dye-sensitized solar cells. *ChemPhysChem* **2012**, *13*, 4032–4080.

[4] Grätzel M. Dye-sensitized solar cells. *J. Photochem. Photobiol. C Photochem. Rev.* **2003**, *4*, 145–153.

[5] O'Regan B., Grätzel M. A low-cost, high-efficiency solar cell based on dye-sensitized colloidal TiO_2 films. *Nature* **1991**, *353*, 737–740.

[6] Nazeeruddin M. K., Kay A., Rodicio I., Humphry-Baker R., Mueller E., Liska P., Vlachopoulos N., Graetzel M. Conversion of light to electricity by cis-X_2bis(2,2'-bipyridyl-4,4'-dicarboxylate)ruthenium(II) charge-transfer sensitizers (X = Cl^-, Br^-, I^-, CN^-, and SCN^-) on nanocrystalline titanium dio. *J. Am. Chem. Soc.* **1993**, *115*, 6382–6390.

[7] Nazeeruddin M. K., Baranoff E., Grätzel M. Dye-sensitized solar cells: A brief overview. *Sol. Energy* **2011**, *85*, 1172–1178.

[8] Nazeeruddin M. K., Zakeeruddin S. M., Humphry-Baker R., Jirousek M., Liska P., Vlachopoulos N., Shklover V., Fischer C.-H., Grätzel M. Acid−Base Equilibria of (2,2'-Bipyridyl-4,4'-dicarboxylic acid)ruthenium(II) Complexes and the Effect of Protonation on Charge-Transfer Sensitization of Nanocrystalline Titania. *Inorg. Chem.* **1999**, *38*, 6298–6305.

[9] Nazeeruddin M. K., Péchy P., Renouard T., Zakeeruddin S. M., Humphry-Baker R., Cointe P., Liska P., Cevey L., Costa E., Shklover V., Spiccia L., Deacon G. B., Bignozzi C. A., Grätzel M. Engineering of efficient panchromatic sensitizers for nanocrystalline TiO_2-based solar cells. *J. Am. Chem. Soc.* **2001**, *123*, 1613–1624.

[10] Altobello S., Argazzi R., Caramori S., Contado C., Da Fré S., Rubino P., Choné C., Larramona G., Bignozzi C. A. Sensitization of Nanocrystalline TiO_2 with Black Absorbers Based on Os and Ru Polypyridine Complexes. *J. Am. Chem. Soc.* **2005**, *127*, 15342–15343.

[11] Argazzi R., Larramona G., Contado C., Bignozzi C. A. Preparation and

photoelectrochemical characterization of a red sensitive osmium complex containing 4,4′,4″-tricarboxy-2,2′:6′,2″-terpyridine and cyanide ligands. *J. Photochem. Photobiol. A Chem.* **2004**, *164*, 15–21.

[12] Ferrere S. New photosensitizers based upon [$Fe^{II}(L)_2(CN)_2$] and [$Fe^{II}L_3$], where L is substituted 2,2′-bipyridine. *Inorganica Chim. Acta* **2002**, *329*, 79–92.

[13] Jayaweera P. M., Palayangoda S. S., Tennakone K. Nanoporous TiO_2 solar cells sensitized with iron(II) complexes of bromopyrogallol red ligand. *J. Photochem. Photobiol. A Chem.* **2001**, *140*, 173–177.

[14] Ferrere S. New Photosensitizers Based upon [$Fe(L)_2 (CN)_2$] and [$Fe(L)_3$] (L = Substituted 2,2′-Bipyridine): Yields for the Photosensitization of TiO_2 and Effects on the Band Selectivity. *Chem. Mater.* **2000**, *12*, 1083–1089.

[15] Hasselmann G. M., Meyer G. J. Sensitization of Nanocrystalline TiO_2 by Re(I) Polypyridyl Compounds*. *Zeitschrift für Phys. Chemie* **1999**, *212*, 39–44.

[16] Hasselmann G. M., Meyer G. J. Diffusion-Limited Interfacial Electron Transfer with Large Apparent Driving Forces. *J. Phys. Chem. B* **1999**, *103*, 7671–7675.

[17] Geary E. A. M., McCall K. L., Turner A., Murray P. R., McInnes E. J. L., Jack L. A., Yellowlees L. J., Robertson N. Spectroscopic, electrochemical and computational study of Pt–diimine–dithiolene complexes: rationalising the properties of solar cell dyes. *Dalt. Trans.* **2008**, *118*, 3701–3708.

[18] Geary E. A. M., Yellowlees L. J., Jack L. A., Oswald I. D. H., Parsons S., Hirata N., Durrant J. R., Robertson N. Synthesis, Structure, and Properties of [Pt(II)(diimine)(dithiolate)] Dyes with 3,3′-, 4,4′-, and 5,5′-Disubstituted Bipyridyl: Applications in Dye-Sensitized Solar Cells. *Inorg. Chem.* **2005**, *44*, 242–250.

[19] Geary E. A. M., Hirata N., Clifford J., Durrant J. R., Parsons S., Dawson A., Yellowlees L. J., Robertson N. Synthesis, structure and properties of [Pt(2,2′-bipyridyl-5,5′-dicarboxylic acid)(3,4-toluenedithiolate)]: tuning molecular properties for application in dye-sensitised solar cells. *Dalt. Trans.* **2003**, *118*, 3757–3762.

[20] Alonso-Vante N., Nierengarten J.-F., Sauvage J.-P. Spectral sensitization of large-band-gap semiconductors (thin films and ceramics) by a carboxylated bis(1,10-phenanthroline)copper(I) complex. *J. Chem. Soc. Dalt. Trans.* **1994**, *97*, 1649.

[21] Bessho T., Constable E. C., Graetzel M., Hernandez Redondo A., Housecroft C. E., Kylberg W., Nazeeruddin M. K., Neuburger M., Schaffner S. An element of surprise—efficient copper-functionalized dye-sensitized solar cells. *Chem. Commun.* **2008**, *123*, 3717.

[22] Liu Y., Xiang N., Feng X., Shen P., Zhou W., Weng C., Zhao B., Tan S.

Thiophene-linked porphyrin derivatives for dye-sensitized solar cells. *Chem. Commun.* **2009**, *353*, 2499.

[23] Wang X.-F., Tamiaki H. Cyclic tetrapyrrole based molecules for dye-sensitized solar cells. *Energy Environ. Sci.* **2010**, *3*, 94–106.

[24] Lin C.-Y., Lo C.-F., Luo L., Lu H.-P., Hung C.-S., Diau E. W.-G. Design and Characterization of Novel Porphyrins with Oligo(phenylethylnyl) Links of Varied Length for Dye-Sensitized Solar Cells: Synthesis and Optical, Electrochemical, and Photovoltaic Investigation. *J. Phys. Chem. C* **2009**, *113*, 755–764.

[25] Rossi G., Zanotti G., Angelini N., Notarantonio S., Paoletti A. M., Pennesi G., Lembo A., Colonna D., Di Carlo A., Reale A., Brown T. M., Calogero G. Bridged phthalocyanine systems for sensitization of nanocrystalline TiO2 films. *Int. J. Photoenergy* **2010**, *2010*, Article ID 136807, 11 pages.

[26] Silvestri F., García-Iglesias M., Yum J.-H., Vázquez P., Victoria Martínez-Díaz M., Grätzel M., Nazeeruddin M. K., Torres T. Carboxy-1,4-phenylenevinylene- and carboxy-2, 6-naphthylene-vinylene unsymmetrical substituted zinc phthalocyanines for dye-sensitized solar cells. *J. Porphyr. Phthalocyanines* **2009**, *13*, 369–375.

[27] Xie Y., Tang Y., Wu W., Wang Y., Liu J., Li X., Tian H., Zhu W. H. Porphyrin Cosensitization for a Photovoltaic Efficiency of 11.5%: A Record for Non-Ruthenium Solar Cells Based on Iodine Electrolyte. *J. Am. Chem. Soc.* **2015**, *137*, 14055–14058.

[28] Yella A., Lee H.-W., Tsao H. N., Yi C., Chandiran A. K., Nazeeruddin M. K., Diau E. W.-G., Yeh C.-Y., Zakeeruddin S. M., Gratzel M. Porphyrin-Sensitized Solar Cells with Cobalt (II/III)-Based Redox Electrolyte Exceed 12 Percent Efficiency. *Science (80-.).* **2011**, *334*, 629–634.

[29] Franchi D., Calamante M., Reginato G., Zani L., Peruzzini M., Taddei M., Fabrizi De Biani F., Basosi R., Sinicropi A., Colonna D., Di Carlo A., Mordini A. A comparison of carboxypyridine isomers as sensitizers for dye-sensitized solar cells: assessment of device efficiency and stability. *Tetrahedron* **2014**, *70*, 6285–6295.

[30] Yang C.-H., Chen H.-L., Chuang Y.-Y., Wu C.-G., Chen C.-P., Liao S.-H., Wang T.-L. Characteristics of triphenylamine-based dyes with multiple acceptors in application of dye-sensitized solar cells. *J. Power Sources* **2009**, *188*, 627–634.

[31] ZHANG F., LUO Y., SONG J., GUO X., LIU W., MA C., HUANG Y., GE M., BO Z., MENG Q. Triphenylamine-based dyes for dye-sensitized solar cells. *Dyes Pigments* **2009**, *81*, 224–230.

[32] Rocca D., Gebauer R., De Angelis F., Nazeeruddin M. K., Baroni S. Time-

dependent density functional theory study of squaraine dye-sensitized solar cells. *Chem. Phys. Lett.* **2009**, *475*, 49–53.

[33] Yum J.-H., Walter P., Huber S., Rentsch D., Geiger T., Nüesch F., De Angelis F., Grätzel M., Nazeeruddin M. K. Efficient Far Red Sensitization of Nanocrystalline TiO_2 Films by an Unsymmetrical Squaraine Dye. *J. Am. Chem. Soc.* **2007**, *129*, 10320–10321.

[34] Burke A., Ito S., Snaith H., Bach U., Kwiatkowski J., Grätzel M. The Function of a TiO_2 Compact Layer in Dye-Sensitized Solar Cells Incorporating 'Planar' Organic Dyes. *Nano Lett.* **2008**, *8*, 977–981.

[35] Fang Z., Eshbaugh A. A., Schanze K. S. Low-Bandgap Donor−Acceptor Conjugated Polymer Sensitizers for Dye-Sensitized Solar Cells. *J. Am. Chem. Soc.* **2011**, *133*, 3063–3069.

[36] Zhang W., Fang Z., Su M., Saeys M., Liu B. A Triphenylamine-Based Conjugated Polymer with Donor-π-Acceptor Architecture as Organic Sensitizer for Dye-Sensitized Solar Cells. *Macromol. Rapid Commun.* **2009**, *30*, 1533–1537.

[37] Kim D., Song K., Kang M.-S., Lee J.-W., Kang S. O., Ko J. Efficient organic sensitizers containing benzo[cd]indole: Effect of molecular isomerization for photovoltaic properties. *J. Photochem. Photobiol. A Chem.* **2009**, *201*, 102–110.

[38] Tanaka H., Takeichi A., Higuchi K., Motohiro T., Takata M., Hirota N., Nakajima J., Toyoda T. Long-term durability and degradation mechanism of dye-sensitized solar cells sensitized with indoline dyes. *Sol. Energy Mater. Sol. Cells* **2009**, *93*, 1143–1148.

[39] Dentani T., Kubota Y., Funabiki K., Jin J., Yoshida T., Minoura H., Miura H., Matsui M. Novel thiophene-conjugated indolinedyes for zinc oxide solar cells. *New J. Chem.* **2009**, *33*, 93–101.

[40] Hattori S., Hasobe T., Ohkubo K., Urano Y., Umezawa N., Nagano T., Wada Y., Yanagida S., Fukuzumi S. Enhanced Energy and Quantum Efficiencies of a Nanocrystalline Photoelectrochemical Cell Sensitized with a Donor−Acceptor Dyad Derived from Fluorescein. *J. Phys. Chem. B* **2004**, *108*, 15200–15205.

[41] Tian H., Yang X., Chen R., Hagfeldt A., Sun L. A metal-free 'black dye' for panchromatic dye-sensitized solar cells. *Energy Environ. Sci.* **2009**, *2*, 674–677.

[42] Tian H., Yang X., Chen R., Pan Y., Li L., Hagfeldt A., Sun L. Phenothiazine derivatives for efficient organic dye-sensitized solar cells. *Chem. Commun.* **2007**, *353*, 3741–3743.

[43] Chen Y.-S., Li C., Zeng Z.-H., Wang W.-B., Wang X.-S., Zhang B.-W. Efficient electron injection due to a special adsorbing group's combination of carboxyl and hydroxyl: dye-sensitized solar cells based on new hemicyanine dyes. *J.*

Mater. Chem. **2005**, *15*, 1654–1661.

[44] Meng F. S., Yao Q. H., Shen J. G., Li F. L., Huang C. H., Chen K. C., Tian H. Novel Cyanine Dyes with Multi-carboxyl Groups and their Sensitization on Nanocrystalline TiO_2 Electrode. *Synth. Met.* **2003**, *137*, 1543–1544.

[45] Sayama K., Tsukagoshi S., Mori T., Hara K., Ohga Y., Shinpou A., Abe Y., Suga S., Arakawa H. Efficient sensitization of nanocrystalline TiO_2 films with cyanine and merocyanine organic dyes. *Sol. Energy Mater. Sol. Cells* **2003**, *80*, 47–71.

[46] Wang Z.-S., Cui Y., Dan-oh Y., Kasada C., Shinpo A., Hara K. Thiophene-Functionalized Coumarin Dye for Efficient Dye-Sensitized Solar Cells: Electron Lifetime Improved by Coadsorption of Deoxycholic Acid. *J. Phys. Chem. C* **2007**, *111*, 7224–7230.

[47] Wang Z.-S., Cui Y., Dan-oh Y., Kasada C., Shinpo A., Hara K. Molecular Design of Coumarin Dyes for Stable and Efficient Organic Dye-Sensitized Solar Cells. *J. Phys. Chem. C* **2008**, *112*, 17011–17017.

[48] Wang Z.-S., Cui Y., Hara K., Dan-oh Y., Kasada C., Shinpo A. A High-Light-Harvesting-Efficiency Coumarin Dye for Stable Dye-Sensitized Solar Cells. *Adv. Mater.* **2007**, *19*, 1138–1141.

[49] Ooyama Y., Shimada Y., Ishii A., Ito G., Kagawa Y., Imae I., Komaguchi K., Harima Y. Photovoltaic performance of dye-sensitized solar cells based on a series of new-type donor–acceptor π-conjugated sensitizer, benzofuro[2,3-c]oxazolo[4,5-a]carbazole fluorescent dyes. *J. Photochem. Photobiol. A Chem.* **2009**, *203*, 177–185.

[50] Kim D., Lee J. K., Kang S. O., Ko J. Molecular engineering of organic dyes containing N-aryl carbazole moiety for solar cell. *Tetrahedron* **2007**, *63*, 1913–1922.

[51] Ooyama Y., Ishii A., Kagawa Y., Imae I., Harima Y. Dye-sensitized solar cells based on novel donor–acceptor π-conjugated benzofuro[2,3-c]oxazolo[4,5-a]carbazole-type fluorescent dyes exhibiting solid-state fluorescence. *New J. Chem.* **2007**, *31*, 2076–2082.

[52] Erten-Ela S., Yilmaz M. D., Icli B., Dede Y., Icli S., Akkaya E. U. A Panchromatic Boradiazaindacene (BODIPY) Sensitizer for Dye-Sensitized Solar Cells. *Org. Lett.* **2008**, *10*, 3299–3302.

[53] Kumaresan D., Thummel R. P., Bura T., Ulrich G., Ziessel R. Color Tuning in New Metal-Free Organic Sensitizers (Bodipys) for Dye-Sensitized Solar Cells. *Chem. - Eur. J.* **2009**, *15*, 6335–6339.

[54] Zhu W., Wu Y., Wang S., Li W., Li X., Chen J., Wang Z., Tian H. Organic D-A-π-A Solar Cell Sensitizers with Improved Stability and Spectral Response. *Adv. Funct. Mater.* **2011**, *21*, 756–763.

[55] Velusamy M., Justin Thomas K. R., Lin J. T., Hsu Y.-C., Ho K.-C. Organic Dyes Incorporating Low-Band-Gap Chromophores for Dye-Sensitized Solar Cells. *Org. Lett.* **2005**, *7*, 1899–1902.

[56] Wu Y., Zhu W. Organic sensitizers from D-π-A to D-A-π-A: effect of the internal electron-withdrawing units on molecular absorption, energy levels and photovoltaic performances. *Chem. Soc. Rev.* **2013**, *42*, 2039–58.

[57] Yum J.-H., Holcombe T. W., Kim Y., Yoon J., Rakstys K., Nazeeruddin M. K., Grätzel M. Towards high-performance DPP-based sensitizers for DSC applications. *Chem. Commun.* **2012**, *48*, 10727–10729.

[58] Zhang F., Jiang K.-J., Huang J.-H., Yu C.-C., Li S.-G., Chen M.-G., Yang L.-M., Song Y.-L. A novel compact DPP dye with enhanced light harvesting and charge transfer properties for highly efficient DSCs. *J. Mater. Chem. A* **2013**, *1*, 4858.

[59] Holcombe T. W., Yum J.-H., Kim Y., Rakstys K., Grätzel M. Diketopyrrolopyrrole-based sensitizers for dye-sensitized solar cell applications: anchor engineering. *J. Mater. Chem. A* **2013**, *1*, 13978–13983.

[60] Kim S., Lim H., Kim K., Kim C., Kang T. Y., Ko M. J., Kim K., Park N.-G. Synthetic Strategy of Low-Bandgap Organic Sensitizers and Their Photoelectron Injection Characteristics. *IEEE J. Sel. Top. Quantum Electron.* **2010**, *16*, 1627–1634.

[61] Tang Z.-M., Lei T., Jiang K.-J., Song Y.-L., Pei J. Benzothiadiazole Containing D-π-A Conjugated Compounds for Dye-Sensitized Solar Cells: Synthesis, Properties, and Photovoltaic Performances. *Chem. - Asian J.* **2010**, *5*, 1911–1917.

[62] Cui Y., Wu Y., Lu X., Zhang X., Zhou G., Miapeh F. B., Zhu W., Wang Z.-S. Incorporating Benzotriazole Moiety to Construct D–A–π–A Organic Sensitizers for Solar Cells: Significant Enhancement of Open-Circuit Photovoltage with Long Alkyl Group. *Chem. Mater.* **2011**, *23*, 4394–4401.

[63] Mao J., Guo F., Ying W., Wu W., Li J., Hua J. Benzotriazole-Bridged Sensitizers Containing a Furan Moiety for Dye-Sensitized Solar Cells with High Open-Circuit Voltage Performance. *Chem. - Asian J.* **2012**, *7*, 982–991.

[64] Chang D. W., Lee H. J., Kim J. H., Park S. Y., Park S.-M., Dai L., Baek J.-B. Novel Quinoxaline-Based Organic Sensitizers for Dye-Sensitized Solar Cells. *Org. Lett.* **2011**, *13*, 3880–3883.

[65] Pei K., Wu Y., Wu W., Zhang Q., Chen B., Tian H., Zhu W. Constructing Organic D-A-π-A-Featured Sensitizers with a Quinoxaline Unit for High-Efficiency Solar Cells: The Effect of an Auxiliary Acceptor on the Absorption and the Energy Level Alignment. *Chem. - Eur. J.* **2012**, *18*, 8190–8200.

[66] Franchi D. Synthesis and characterization of new D-π-A organic

photosensitizers for DSSC with pyridine moiety acceptor. ('Laurea Magistrale' thesis, University of Florence, **2013**).

[67] Chen C., Yang X., Cheng M., Zhang F., Sun L. Degradation of cyanoacrylic acid-based organic sensitizers in dye-sensitized solar cells. *ChemSusChem* **2013**, *6*, 1270–1275.

[68] Gabrielsson E., Tian H. N., Eriksson S. K., Gao J. J., Chen H., Li F. S., Oscarsson J., Sun J. L., Rensmo H., Kloo L., Hagfeldt A., Sun L. C. Dipicolinic acid: a strong anchoring group with tunable redox and spectral behavior for stable dye-sensitized solar cells. *Chem. Commun.* **2015**, *51*, 3858–3861.

[69] Franchi D., Calamante M., Reginato G., Zani L., Peruzzini M., Taddei M., Fabrizi De Biani F., Basosi R., Sinicropi A., Colonna D., Di Carlo A., Mordini A. Two New Dyes with Carboxypyridinium Regioisomers as Anchoring Groups for Dye-Sensitized Solar Cells. *Synlett* **2015**, *26*, 2389–2394.

[70] Tian J., Yang X. C., Zhao J. H., Wang L., Wang W. H., Li J. J., Sun L. C. Organic D-π-A sensitizer with pyridinium as the acceptor group for dye-sensitized solar cells. *RSC Adv.* **2014**, *4*, 34644–34648.

[71] Yanai T., Tew D. P., Handy N. C. A new hybrid exchange–correlation functional using the Coulomb-attenuating method (CAM-B3LYP). *Chem. Phys. Lett.* **2004**, *393*, 51–57.

[72] Lynch B. J., Fast P. L., Harris M., Truhlar D. G. Adiabatic Connection for Kinetics. *J. Phys. Chem. A* **2000**, *104*, 4811–4815.

[73] Becke A. D. Density-functional thermochemistry. III. The role of exact exchange. *J. Chem. Phys.* **1993**, *98*, 5648–5652.

[74] Lee C., Yang W., Parr R. G. Development of the Colle-Salvetti correlation-energy formula into a functional of the electron density. *Phys. Rev. B* **1988**, *37*, 785–789.

[75] Stephens P. J., Devlin F. J., Chabalowski C. F., Frisch M. J. Ab Initio Calculation of Vibrational Absorption and Circular Dichroism Spectra Using Density Functional Force Fields. *J. Phys. Chem.* **1994**, *98*, 11623–11627.

[76] Chang Y. J., Chow T. J. Highly efficient red fluorescent dyes for organic light-emitting diodes. *J. Mater. Chem.* **2011**, *21*, 3091–3099.

[77] Zhao J., Yang X., Cheng M., Li S., Sun L. Molecular Design and Performance of Hydroxylpyridium Sensitizers for Dye-Sensitized Solar Cells. *ACS Appl. Mater. Interfaces* **2013**, *5*, 5227–5231.

[78] Hagberg D. P., Jiang X., Gabrielsson E., Linder M., Marinado T., Brinck T., Hagfeldt A., Sun L. Symmetric and unsymmetric donor functionalization. comparing structural and spectral benefits of chromophores for dye-sensitized solar cells. *J. Mater. Chem.* **2009**, *19*, 7232–7238.

[79] Dyson P., L. Hammick D. Experiments on the mechanism of decarboxylation. Part I. Decomposition of quinaldinic and isoquinaldinic acids in the presence of compounds containing carbonyl groups. *J. Chem. Soc.* **1937**, *35*, 1724.

[80] Haake P., Mantecon J. Kinetic Studies of the Decarboxylation of Some N-Substituted Pyridinecarboxylic Acids. *J. Am. Chem. Soc.* **1964**, *86*, 5230–5234.

[81] Kraeutler B., Bard A. J. Heterogeneous Photocatalytic Decomposition of Saturated Carboxylic Acids on TiO2 Powder. Decarboxylative Route to Alkanes. *J. Am. Chem. Soc.* **1978**, *100*, 5985–5992.

[82] Soja G. R., Watson D. F. TiO_2-Catalyzed photodegradation of porphyrins: Mechanistic studies and application in monolayer photolithography. *Langmuir* **2009**, *25*, 5398–5403.

[83] Irimia-Vladu M., Gåowacki E. D., Troshin P. A., Schwabegger G., Leonat L., Susarova D. K., Krystal O., Ullah M., Kanbur Y., Bodea M. A., Razumov V. F., Sitter H., Bauer S., Sariciftci N. S. Indigo - A natural pigment for high performance ambipolar organic field effect transistors and circuits. *Adv. Mater.* **2012**, *24*, 375–380.

[84] Rumer J. W., Dai S.-Y., Levick M., Kim Y., Madec M.-B., Ashraf R. S., Huang Z., Rossbauer S., Schroeder B., Biniek L., Watkins S. E., Anthopoulos T. D., Janssen R. a. J., Durrant J. R., Procter D. J., McCulloch I. Dihydropyrroloindoledione-based copolymers for organic electronics. *J. Mater. Chem. C* **2013**, *1*, 2711–2716.

[85] Son H. J., Carsten B., Jung I. H., Yu L. Overcoming efficiency challenges in organic solar cells: rational development of conjugated polymers. *Energy Environ. Sci.* **2012**, *5*, 8158–8170.

[86] Chen Z., Lee M. J., Shahid Ashraf R., Gu Y., Albert-Seifried S., Meedom Nielsen M., Schroeder B., Anthopoulos T. D., Heeney M., McCulloch I., Sirringhaus H. High-performance ambipolar diketopyrrolopyrrole-thieno[3,2-b]thiophene copolymer field-effect transistors with balanced hole and electron mobilities. *Adv. Mater.* **2012**, *24*, 647–652.

[87] Holcombe T. W., Yum J.-H., Yoon J., Gao P., Marszalek M., Censo D. Di, Rakstys K., Nazeeruddin M. K., Graetzel M. A structural study of DPP-based sensitizers for DSC applications. *Chem. Commun.* **2012**, *48*, 10724–10726.

[88] Wang J., Chen X., Cai Z., Luo H., Li Y., Liu Z., Zhang G., Zhang D. New alternating electron donor-acceptor conjugated polymers entailing (E)-[4,4′-biimidazolylidene]-5,5′(1H,1′H)-dione moieties. *Polym. Chem.* **2013**, *4*, 5283–5290.

[89] Lu S., Drees M., Yao Y., Boudinet D., Yan H., Pan H., Wang J., Li Y., Usta H., Facchetti A. 3,6-Dithiophen-2-yl-diketopyrrolo[3,2- b]pyrrole (isoDPPT) as an Acceptor Building Block for Organic Opto-Electronics. *Macromolecules* **2013**, *46*,

3895–3906.

[90] Wang J., Chen X., Zhang G., Liu Z., Zhang D., Murphy A., Fréchet J., Zaumseil J., Sirringhaus H., Anthony J., Facchetti A., Heeney M., Marder S., Zhan X., Beaujuge P., Fréchet J., Usta H., Facchetti A., Marks T. J., *et al.* Conjugated electron donor–acceptor molecules with (E)-[4,4′-biimidazolylidene]-5,5′(1H,1′H)-dione for new organic semiconductors. *J. Mater. Chem. C* **2014**, *2*, 1149–1157.

[91] Norsten T. B., Kantchev E. A. B., Sullivan M. B. Thiophene-Containing Pechmann Dye Derivatives. *Org. Lett.* **2010**, *12*, 4816–4819.

[92] Lukin K., Kishore V., Gordon T. Development of a scalable synthesis of oxadiazole based S1P1 receptor agonists. *Org. Proc. Res. Dev.* **2013**, *17*, 666–671.

[93] Seefelder M. *Indigo In Culture, Science and Technology*. *Landsberg, Germany* (Ecomed, **1994**).

[94] Amat A., Rosi F., Miliani C., Sgamellotti A., Fantacci S. Theoretical and experimental investigation on the spectroscopic properties of indigo dye. in *Journal of Molecular Structure* (**2011**). *993*, 43–51.

[95] Gowacki E. D., Leonat L., Voss G., Bodea M. A., Bozkurt Z., Ramil A. M., Irimia-Vladu M., Bauer S., Sariciftci N. S. Ambipolar organic field effect transistors and inverters with the natural material Tyrian Purple. *AIP Adv.* **2011**, *1*,

[96] Głowacki E. D., Voss G., Demirak K., Havlicek M., Sünger N., Okur A. C., Monkowius U., Gąsiorowski J., Leonat L., Sariciftci N. S. A facile protection-deprotection route for obtaining indigo pigments as thin films and their applications in organic bulk heterojunctions. *Chem. Commun. (Camb).* **2013**, *49*, 6063–5.

[97] He B., Pun A. B., Zherebetskyy D., Liu Y., Liu F., Klivansky L. M., McGough A. M., Zhang B. A., Lo K., Russell T. P., Wang L., Liu Y. New form of an old natural dye: Bay-annulated indigo (BAI) as an excellent electron accepting unit for high performance organic semiconductors. *J. Am. Chem. Soc.* **2014**, *136*, 15093–15101.

[98] McKee J. R., Zanger M. A microscale synthesis of indigo: Vat dyeing. *J. Chem. Educ.* **1991**, *68*, A242.

[99] Shih T. L., Wyvratt M. J., Mrozik H. Total synthesis of (.+-.)-5-O-methyllicoricidin. *J. Org. Chem.* **1987**, *52*, 2029–2033.

[100] Miyashita M., Suzuki T., Hoshino M., Yoshikoshi A. The organoselenium-mediated reduction of α,β-epoxy ketones, α,β-epoxy esters, and their congeners to β-hydroxy carbonyl compounds: Novel methodologies for the synthesis of aldols and their analogues. *Tetrahedron* **1997**, *53*, 12469–12486.

[101] Liang Y., Peng B., Liang J., Tao Z., Chen J. Triphenylamine-Based Dyes Bearing Functionalized 3,4-Propylenedioxythiophene Linkers with Enhanced

Performance for Dye-Sensitized Solar Cells. *Org. Lett.* **2010**, *12*, 1204–1207.

[102] Hammond S. R., Clot O., Firestone K. A., Bale D. H., Lao D., Haller M., Phelan G. D., Carlson B., Jen A. K.-Y., Reid P. J., Dalton L. R. Site-Isolated Electro-optic Chromophores Based on Substituted 2,2′-Bis(3,4-propylenedioxythiophene) π-Conjugated Bridges. *Chem. Mater.* **2008**, *20*, 3425–3434.

[103] Cafiero L. R., Snowden T. S. General and practical conversion of aldehydes to homologated carboxylic acids. *Org. Lett.* **2008**, *10*, 3853–3856.

[104] Thompson B. C., Kim Y. G., McCarley T. D., Reynolds J. R. Soluble narrow band gap and blue propylenedioxythiophene-cyanovinylene polymers as multifunctional materials for photovoltaic and electrochromic applications. *J. Am. Chem. Soc.* **2006**, *128*, 12714–12725.

Chapter 4

Gold Nanoparticles

UV-Vis estimation of the organic dye absorption enhancement due to electromagnetic interaction with core-shell gold-insulating nanoparticles.

4.1. Introduction and background

As already pointed out, a DSSC is a complex system formed by many different components: in particular, the thin semitransparent support, the sensitizer and the redox media, which interact with each other at the semiconductor/dye/electrolyte interface. While on the one hand the number of components of a DSSC makes its structure and physical properties highly tunable and improvable, on the other hand any change might have some drawback: in other words, every modification cannot be done without considering its effect on all other DSSC components. For example, the redox potential of cobalt-based electrolytes is less negative than that of the I^-/I_3^- based redox-media, therefore, the use of such Co electrolytes enhances the V_{OC} of the devices. On the other hand, the interaction with dye needs to be taken into account as well: the over-potential for the regeneration of the oxidized dye is reduced and thus, depending on its HOMO position, this could also lead to inefficient dye regeneration.

In general, it is not easy to identify a modification able to improve the performances of a DSSC without requiring a fine adaptation of the rest of the system, however, such kind of modifications would be of great utility,[1,2] being, probably, the only way to enhance the performances of those devices where the best combinations between elements was already found.

The key process in all DSSC devices is the light absorption by the dye, resulting in the first charge separation event, the photo-injection. The strategy generally applied for enhancing light absorption is to modify the chemical structure of the photosensitizer, in turn affecting a series of physico- and electrochemical properties (the potential of the frontier molecular orbitals, the dye-dye aggregation, the anchoring stability…), often unwillingly. Clearly, introduction of a component able to intensify dye light absorption without requiring any structural modification, and at the same time leaving unchanged the other properties of the final device, would be a more effective and straightforward way to enhance cell efficiency.

A promising approach showing all these characteristics is represented by the use of metal nanoparticles (NPs) to modify the semiconductor substrate. Indeed, it is known that NPs are able to trigger the local enhancement of electromagnetic field, increasing the light absorption of the dye, while avoiding electrochemical interactions with the DSSC components.

4.1.1. Metal nanoparticles and dyes: Near-Field Effect.

The conduction electrons of a metal are free to oscillate in the proximity of fixed positively charged metal atoms. The metal superficial electrons can resonate with incident light giving a collective transitions known as Surface Plasmon Resonance (SPR).[3] When the dimension of the metallic object has nanometric scale there is no more distinction between superficial and bulk electrons: therefore, they all together act as a free electron gas (plasma).[4] (*Figure 4.1*) In metal nanoparticles the dimension of the system acts as a confining agent for the oscillating plasma, and the kind of metal determines the positive nuclei restoring force acting on the moving electrons; together they regulate the resonance frequency.[5]

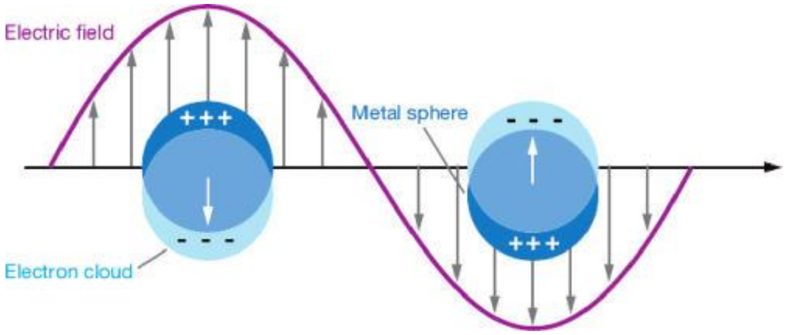

Figure 4. 1: Surface Plasmon Resonance: the electron gas of a metal NP resonating with the light electric field.

As a final consideration, we observe that metal NPs electrons are polarized by the electronic field of light and, at a certain wavelength depending on dimension ad composition, NPs can absorb light giving SPR.

One of the effects of SPR in metal NPs is the enhancement of the electromagnetic field in the proximity of the NPs surface. (*Figure 4.2*) This phenomenon is known as near-field enhancement (NFE).[6] When polarized by the electric field of light, the electron plasmon oscillates and creates itself an electromagnetic field, acting therefore as an antenna. This behavior can be seen as a way for the NPs to reemit the energy absorbed from light. In the proximity of the antenna, the electromagnetic field produced (known as near-field) is characterized by a non-radiating behavior. At greater distances, instead, the far-field dominates, which shows radiative behavior. The near-field produced by metal NPs is some order of magnitude more intense than the external one, (*Figure 4.2*) therefore a chromophore close enough to the metal surface would experience the NFE at the frequency of NPs resonance. If also the chromophore can harvest light at this frequency, then light absorption enhancement will be observed. This mechanism of interaction is the most frequent justification for the enhancement of efficiencies in DSSC resulting from metal NPs employment.[2,7–14]

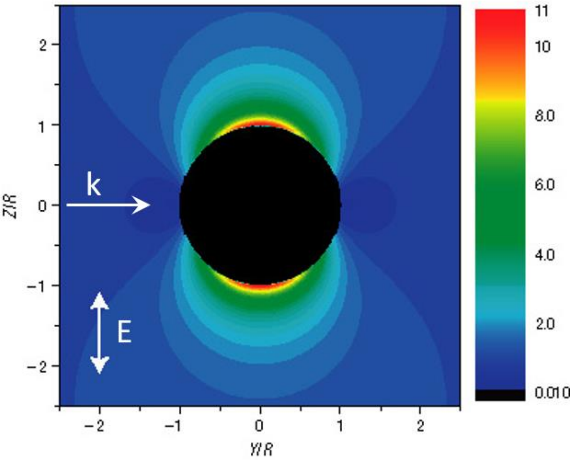

Figure 4. 2: ***Near-Field of a nanoparticle****. In the picture we report the direction of propagation (k) for the incident light; light electric field (E) oscillates in the plane. The intensity of the electric field is color-coded the relative legend is reported aside in logarithmic scale.*

In particular, it has been shown recently that the use of metal NPs-doped semiconductor was able to increase light absorption of Ruthenium-based dyes, resulting, in some cases, in excellent enhancements of PV efficiencies.[7] Using NPs to concentrate light it was also possible to reduce the thickness of the TiO_2 substrate[9] without weakening light absorption. This way, the distance that charges must travel within the semiconductor layer to reach the external circuit is reduced, together with the probability of charge recombination. The studies reported in the literature have explored the exploitation of many nanometric systems and different features such as the kind of metal employed,[8] NPs dimension,[10,11,15] shelling components[2,12] and degree of aggregation[7] were found to enhance the efficiency of DSSC to different extents. Although this field has experienced a great interest in recent years,[16] such investigations are focused mostly on the achievement of top-class efficiencies and are based on established Ru complex-sensitized DSSC,[2,7–9,15,17] and there are no reports on the use of NPs in DSSCs sensitized with purely organic dyes.

Supposing that also organic dyes can take advantage from the introduction of NPs in the solar cell structure, I decided to investigate how their light harvesting could be enhanced due to the insertion of gold nanospheres in the semiconducting substrate composition.

More in detail, I focused on demonstrating that NFE is also a possible way of interaction between NPs and organic dyes. Remarkably, NFE is one of the proposed mechanisms of efficiency enhancement that do not perturb the electronic characteristics of the rest of the system and thus would not require adaptation of the other DSSC components. Finally, it is worth mentioning that demonstration of NFE on organic dyes does not require the construction of a whole PV device. The dye absorption enhancement expected from such interactions can be observed by simply UV-Vis measurements on NPs-doped semiconductor substrates sensitized with the organic dyes.[9,13,18]

4.1.2. Interactions of NP with semiconductor substrates.

The effects of metal nanoparticles embedded in the semiconductor substrate of a DSSC are numerous: some of them, such as NFE, can be beneficial and lead to enhancements of power conversion efficiencies, but some others could hinder the DSSC functioning. For example, it has been reported that large NPs can scatter light,[19] increasing the probability of light absorption by the sensitizer molecules and thus the efficiencies of PV devices. In other studies, it has been proved that the metal could itself inject electrons[9,20] in the semiconductor, or act as fast electron conductor through the substrate.[21] On the other hand, metal surfaces are also known to act as recombination sites[8,22] for injected electrons and behave as electron trapping states.[8,23–25] One of the purposes of this study was to select only one mechanism of interaction between the NPs and the dye: the NFE effect. This can be achieved by allowing only electromagnetic interactions between the metal NPs and the environment to take place.

Nanoparticles were then synthesized considering several features. We decided to prepare gold nanospheres with a diameter smaller than 50nm in order to rule out scattering effects. Although gold and silver are equally widely reported for applications in DSSC,[9,18] we preferred to use gold for our experiments since it is known that gold nanospheres of a diameter of 50nm resonate at around 530 nm, ensuring overlap with the absorption band of many organic dyes. The shape of the NPs was chosen for the simplicity of the synthetic procedure.[26–28]

A SiO_2 shell was used to chemically insulate the gold core and protect it from corrosion,[8,13] since gold is not inert enough when reduced in NP form to prevent corrosion from the redox electrolytes normally used in DSSC.[22] Furthermore, SiO_2, being an electric insulating material, also creates a potential barrier[29] that blocks the electronic interactions of AuNPs with the semiconductor. (*Figure 4.3 Left*) In this way, only electromagnetic interactions between AuNPs and the dye are permitted, and therefore exclusively NFE on organic dyes can be studied, provided that the dye is anchored on the shell and close enough to the gold NP core.

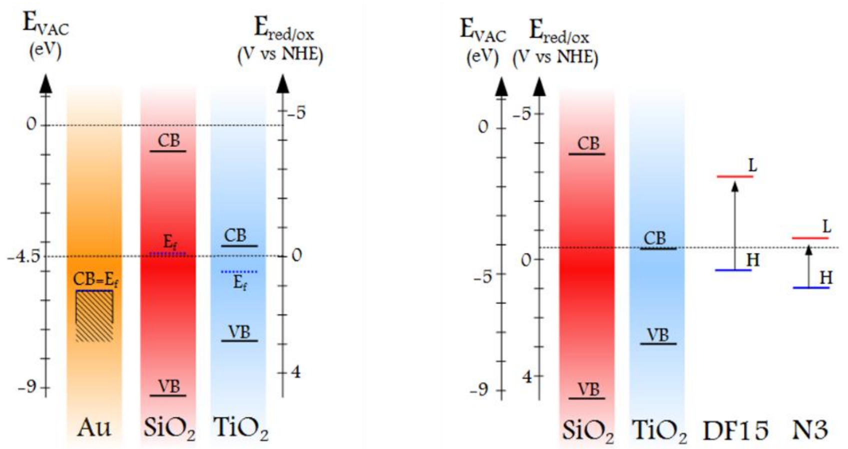

Figure 4. 3: Left: ***Conduction band and Fermi level potentials for isolated gold, silica and titania****: when metal-oxide core-shell systems are built, the high CB of SiO_2 gives rise to electronic insulation of the metal core, while the conduction bands of Au and TiO_2 are close enough to allow electronic interactions. Right:* ***Metal oxides electronic bands and dyes frontier orbitals****: the energy of an electron in the dye excited state is higher than the one of the TiO_2 CB therefore electron injection is feasible; on the contrary, the energy of the excited state electrons is not enough to allow injection in SiO_2.*

Unfortunately, the isolating feature of SiO_2 prevents also the dye molecules, possibly anchored to the shell, from injecting electrons (*Figure 4.3 Right*) in the TiO_2 semiconductor and this fact is detrimental for the potential effectiveness of the use of plasmonic particles in DSSC. An effective way to overcome this problem can be to coat the nanoparticles with TiO_2 instead. The TiO_2 layer conceals the metal NPs into the TiO_2 based photoanodes used in DSSC protecting them from corrosion,[9,18] and the dye attached to the core-shell nanocomposites surface can inject electrons in the semiconductor layer. However, the junction between Au and TiO_2 is not characterized by the rise of a potential barrier. Even if TiO_2 provides chemical insulation of the nanoparticles it does not shield them from electrical interactions, opening up the metal core to electron storing phenomena known as charging effect.[2,30,31]

The solution to both problems was found in analyzing the interaction of AuNPs with the dye by means of UV-Vis absorption on sensitized substrates, instead of electronic characterization of the whole PV devices, according to two main considerations. First, as previously explained, the absorption enhancement of the dye can be directly correlated to the performance improvement of the full device; secondly, operating on the isolated semiconductor film, the problems of (loss of) electron injection of AuNPs@SiO_2 and electron storing of AuNPs@TiO_2 could be neglected.

Before describing the details of the performed spectroscopic characterization, a few comments need to be made regarding the changes of the local environment of the metal NPs due to the presence of the oxide shell. For a metal nanoparticle in water (refractive index ≈ 1.33), the presence of a silica shell (refractive index ≈ 1.46) or a titania shell (refractive index ≈ 2.49) will result in a weak red-shift in the plasmonic response detectable by UV-Vis measurements.[7] However, such shift is supposed to be in the order of 5 nm for both thin shelling systems, and therefore its effect on the overlap of the SPR peak with the dye absorption band can be neglected.[13] It is essential to achieve a covering shell as thin as possible to allow the chromophore bound to the surface to benefit of the NFE of the metal core. In synthetizing the nanocomposites for this work, special attention was given to achieve homogenous layers and similar thickness in both AuNPs@SiO_2 and AuNPs@TiO_2 samples. The oxide layers were maximum 4 nm thick, in line with those employed in other works.

4.1.3. Elect method

Our approach to study the effect of the interactions of AuNPs with the dye has been that of analyzing the enhancement of dye absorption by UV-Vis spectroscopy on the half-cell samples built with the doped semiconductor.

This technique would make all the process simpler allowing to avoid the electronic characterization of the full cell. Thus, we decided to evaluate the enhancement of absorption of an organic dye due to different core-shell nanosystems embedded in the semiconductor substrate. The analyzed samples were semitransparent TiO_2 layers doped with AuNPs covered with SiO_2 or TiO_2 shells. The semiconducting films were sensitized with a previously synthetized organic dye (**DF15**).[32]

4.2. Samples preparation.

4.2.2. Synthesis of AuNPs.

The first methodology for preparing AuNPs was reported in 1951, when Turkevich *et al.* identified the citrate reduction synthesis method.[33] This reaction remains one of the simplest and most straightforward methods for synthesizing metal NPs, but many other strategies have also been developed, providing even more monodispersed solutions.[26,27,34]

Our choice was that of employing a two-step process yielding AuNPs stabilized by cetyl-trimethylammonium bromide (CTAB). Indeed, this is a more complicated synthetic procedure but was preferred because it allowed more consistent and successful results in the following functionalization of the AuNPs surface with respect to the citrate stabilized AuNPs obtained with Turkevich's method. The method used here to synthetize monodisperse AuNPs colloids is known as the seed-growth procedure.[26] (*Scheme 4.* 1) The first step involves the reduction of $HAuCl_4$ solution into small gold 'seeds' colloid solution by means of $NaBH_4$. In this procedure the reducing agent is not acting as stabilizer, while this role is played instead by CTAB present in high concentrations in the reaction mixture. The pre-plasmonic small nanoparticles obtained were found to have an average dimension of around 6 nm as determined by TEM. (*Figure 4.4*) This colloid solution could not be stored since, due to Oswald ripening,[35] such small NPs easily underwent aggregation to form bigger and more stable NPs. New nanoseeds solutions were prepared for each synthesis of nanocomposites, as the final dimensions of the AuNPs tend to be less controllable with the seeds ageing.

The second step of the synthesis (*Scheme 4.* 1) consisted in the growth of AuNPs to the desired dimensions starting from the nanoseeds. A growth solution was prepared by mixing gold precursor $HAuCl_4$, the stabilizer CTAB and a mild reducing agent such as ascorbic acid. With this technique the secondary nucleation in the growing solution is avoided[36,37] and the growth of gold occur only on the seeds nanocrystals resulting in more control over dimension and size dispersion of the NPs.[26]

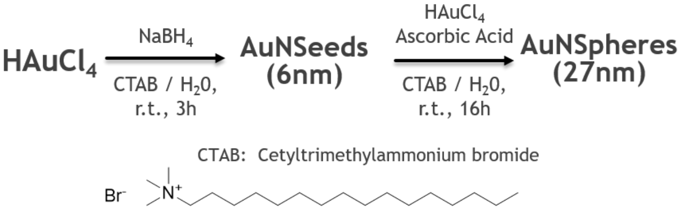

Scheme 4. 1: ***Seeds-Growth procedure for the synthesis of gold nanospheres.***

A freshly prepared solution of seeds was used to provide the growth solution of the nucleation sites. Since the reduction to Au^0 can occur only on the surface of the seeds, fine control of the dimension of AuNPs is possible by changing the amount of seed solution purged into a fix volume of growth solution. The total nanosphere volume is strongly dependent on the amount of seeds added to the growth solution (*Eq. 4.1*). Reducing the seed concentration will lead to fewer, larger spheres as the gold in the growth solution will be deposited in less seeds. Following *Eq. 4.1,* solutions of 20 nm to 200 nm diameter AuNPs could be obtained.[26] A 30 nm diameter was chosen for the AuNPs as a good compromise between low scattering effect and simplicity of synthesis and purification of the samples.

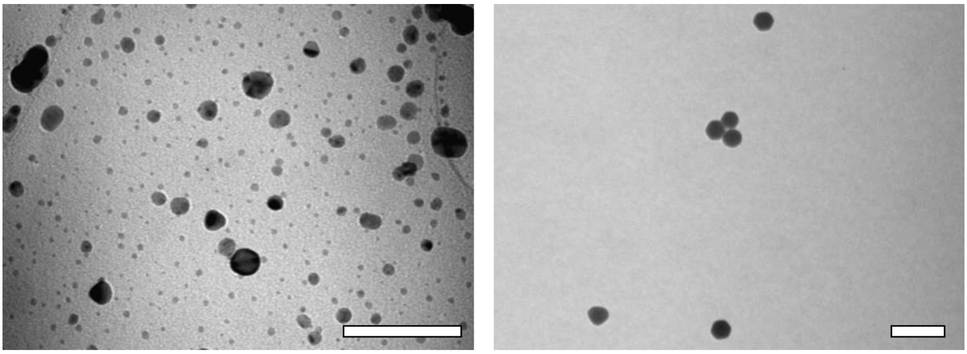

Figure 4. 4: Left: ***TEM image of gold nanoparticles and unreacted seeds:*** *seeds were found to be of ca. 6 nm. Right:* ***TEM image of bare gold nanoparticles****: after centrifuge cleaning procedure, only AuNPs of ca 27 nm are left in the colloid. – (Scale bars are both 100 nm).*

The nanoparticles were characterized by TEM technique and the images obtained are reported in. As clearly shown, immediately after the growth reaction, the colloid contains AuNPs and seeds of approx. 6 nm diameter. However, after cleaning procedure by means of centrifugation and redispersion in clean media, only AuNPs of ca 27 nm diameter are left in the colloid. (*Figure 4.4*)

$$\left(D^3 - D^3_{seeds}\right) * V = C$$ *Eq. 4.1*

In *Eq. 4.1*, D and D_{seeds} are the diameter of the desired AuNPs and the diameter of the seeds respectively, V is the volume of seeds solution that needs to be added to the growth solution, and C is an experimental constant depending on the concentration and the volume of the growth solution.

4.2.3. Functionalization of AuNPs and growth of shells.

The functionalization of the AuNPs surface with oxides such as SiO_2 is not a straightforward process. Gold has a very little affinity for SiO_2 because, unlike most other metals, it does not form a passivation oxide film,[38] thus if treated with SiO_2 precursors the process could create NPs of SiO_2 instead of coating the already existing AuNPs. In synthetizing the nanocomposites for this work, special attention was given to achieve homogenous layers, with a maximum thickness of 4 nm. This was in line with similar materials employed in other works.[7] Furthermore we took a special attention to obtain a similar thickness in both AuNPs@SiO_2 and AuNPs@TiO_2 samples.

Procedures for coating metal nanoparticles with a silica shell generally consist of two primary processes. In the first step, a silicon-containing material is attached to the surface.

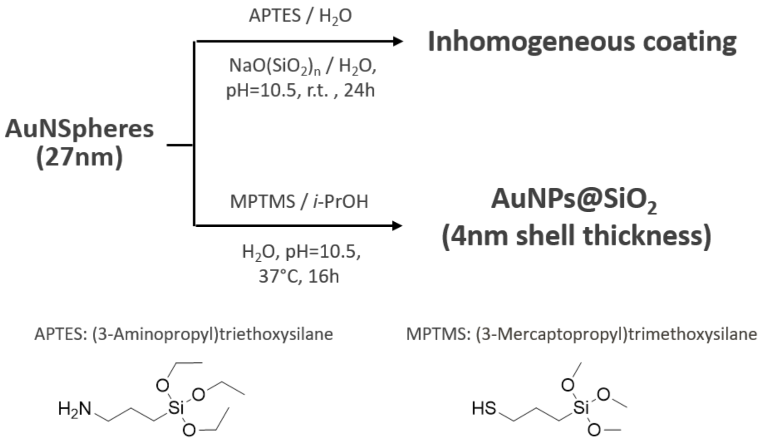

*Scheme 4. 2: **Functionalization of AuNPs and growth of a SiO_2 shell.***

In our case, (*Scheme 4.2*) functionalization of the NPs surface was accomplished using low quantities of (3-aminopropyl)triethoxysilane (APTES): the amino function is responsible for anchoring to the gold surface while, at the other end of the molecule, the silane moiety acts as a starter for the condensation of silicates.[8] When using APTES, only a monolayer can be grown effectively without causing SiO_2 condensation.[38] A second step is required to grow the silica shell on the NPs that, thanks to the functionalization, can now act as nucleation sites for SiO_2 precursors. Generally, a pH-driven precipitation of SiO_2, from a diluted silicate solution ($Na_2O(SiO_2)_n$) in water is used, but in our case this method was found to give rise to incomplete and inhomogeneous coverage of the spherical surface. We assumed that this result could probably be due to an insufficient stability of APTES functionalization of the surface, therefore another procedure was employed using (3-mercaptopropyl) trimethoxysilane (MPTMS) instead. (*Scheme 4.2*)

As the affinity of sulfur for gold gives rise to a much stronger binding between the AuNPs and MPTMS, the functionalization of the surface occurs quite quickly and, leaving the reaction mixture in adequate pH condition, the silane moiety of MPTMS starts to condensate on the NPs surface creating a SiO_2 layer (*Figure 4.5*) without the need of another silica precursor. SiO_2 NPs were obtained as side-products and removed during the cleaning procedure. Furthermore, the kinetics of condensation turned out to be suitable to allow the formation of homogenous layers, even at very low thickness.

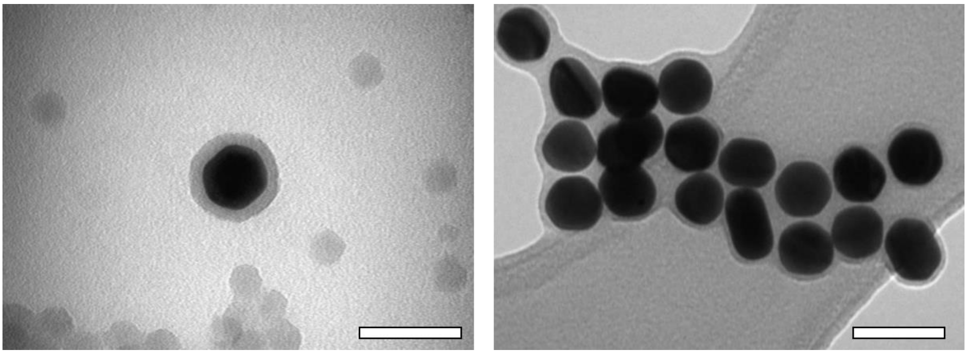

*Figure 4. 5: **TEM image of gold nanoparticles embedded in silica**. (Left) AuNP@SiO_2 obtained from condensation of MPTMS. Before washing procedure, SiO_2 NPs can be found in the colloid. (Right) AuNP@SiO_2 colloid after cleaning procedure. Gold cores have an average diameter of 27 nm and the shell is ca 4 nm thick. – (Scale bars are 50 nm).*

The obtained samples were cleaned by centrifuge precipitation and dispersion in clean CTAB solution, after that, gold nanoparticles embedded in silica were observed by TEM, (*Figure 4.5*) showing gold cores having an average diameter of 27 nm with a shell which is about 4 nm thick The procedure was optimized to obtain a reproducible and homogeneous SiO_2 layer of 4 nm around the AuNPs.

For the formation of a TiO_2 layer the same issue of incompatibility with bare gold surfaces had to be faced; moreover, there were no suitable building blocks to be used capable of anchoring to the gold surface and at the same time carrying a TiO_2 precursor.

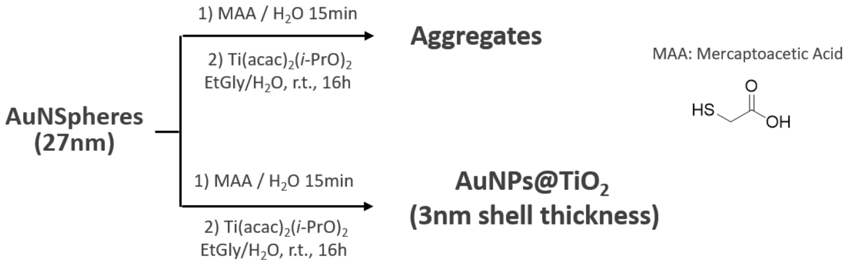

Scheme 4. 3: ***Functionalization of AuNPs and growth of a TiO_2 shell.***

Thus, we chose an approach based first on the functionalization of the gold surface, and then on the addition of a TiO_2 precursor. In view of our precedent results, we decided to use a mercapto-derivative, namely mercapto-acetic acid (MAA),[2] to functionalize the AuNPs, after which titanium diisopropoxide ($Ti(i\text{-}PrO)_4$) was used as a precursor of TiO_2[9,39] (*Scheme 4.* 3).

Even at a low concentration of Au NPs and with a very slow addition of the reactant to the reaction mixture, the kinetics of condensation were too fast, and chaotic precipitation of TiO_2 occurred mostly. After a screening of different TiO_2 precursors and different reaction conditions such as precursor concentration, the speed of addition to the colloid and the reaction solvent, we found the more stable titanium diisopropoxide bis(acetylacetonate) ($Ti(acac)_2(i\text{-}PrO)_2$) to give a more controllable reaction. Furthermore, the condensation was performed in a water mixture of ethyleneglycol (EtGly), which increased the TiO_2 precursor stability by complexing the metal cation. These changes resulted in a reduction of the hydrolysis speed of the Ti^{4+} complex, with consequent formation of thinner shells around AuNPs and of less aggregation byproducts. The obtained nanoparticles were characterized by TEM imaging, (*Figure 4.6*) and were found to have an average core diameter of 27 nm with a shell of about 3 nm thickness.

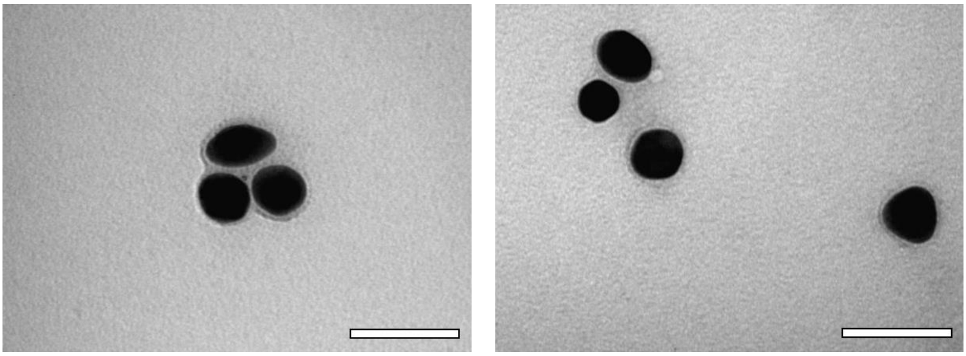

Figure 4. 6: ***TEM image of gold nanoparticles embedded in titania****. Details of AuNPs@TiO_2, gold cores were functionalized with MAA before slowly condensate the shell by means of $Ti(acac)_2(i\text{-}PrO)_2$ in EtGly. Gold cores have an average diameter of 27 nm and the shell is ca 3 nm thick. – (Scale bars are 50 nm).*

Dynamic Laser Scattering (DLS) and UV-Vis spectrometry were also used to characterize the particles. While DLS allows a direct measurement of the dimension of the nanoparticles, UV-Vis spectrometry is employed to evaluate the dimension of NPs considering also their solvation sphere. Clearly, the informations which can be obtained by the two techniques are different. Concerning NPs dimensions, Uv-Vis characterization can be used only as a comparative tool or for a qualitative evaluation. In particular, the full width at half maximum of the plasmonic band can be related to the dispersion of NP dimensions, or, in the case of functionalized colloids, the broadening of the absorption peak can be attributed to aggregation of NPs; finally, the red-shift of the wavelength of maximum absorption can be related to the growth of a shell around the NPs, constituted by a material with high refractive index. An example is reported in *Figure 4.7*, where normalized absorption spectra of our nanoparticles are shown, displaying a red-shift of the plasmonic peak (λ_{max}) upon shell growth due to increase of the refractive index around the metal core. Bare AuNPs in water ($n \approx 1.33$) had $\lambda_{max} = 528$ nm, while AuNPs@SiO_2 ($n \approx 1.46$) showed $\lambda_{max} = 531$ nm and finally AuNPs@TiO_2 ($n \approx 2.49$) presented $\lambda_{max} = 534$ nm. No significant broadening was detected accounting for the absence of nanoparticle aggregation.

For all prepared samples, a change of solvent from water to EtOH was required before employing the colloids in the preparation of the semiconductor slurry. Generally, bare AuNPs are not stable in EtOH, to prevent the aggregation of the NPs it is necessary to functionalize the metal surface or to embed the NP with an insulation shell. In our case, the observed stability in EtOH solution of both the AuNPs@SiO_2 and

AuNPs@TiO_2 colloids was considered another proof for the correct accomplishment of the insulating shell.

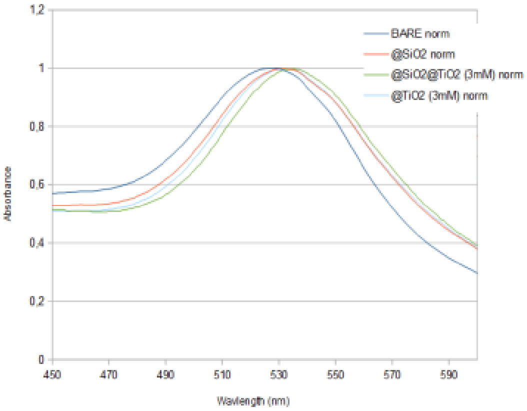

Figure 4. 7: ***Normalized absorption spectra of colloidal solutions of bare AuNPs as well as AuNPs with different shells****. A red-shift of the plasmonic peak* λ_{max} *occurs upon shell growth due to increase of the refractive index around the metal core. Bare AuNPs in water* ($n \approx 1.33$) $\lambda_{max} = 528nm$*, AuNPs@*SiO_2 ($n \approx 1.46$) $\lambda_{max} = 531nm$*, AuNPs@*TiO_2 ($n \approx 2.49$) $\lambda_{max} = 534nm$*. No broadening was detected accounting for the avoid of aggregation.*

4.2.4. AuNPs doped semiconductor substrates preparation.

As described above, the determination of the absorption enhancement of the organic sensitizer due to the presence of AuNPs, was studied by UV-Vis characterization of a dye adsorbed on a substrate of semiconductor embedding the NPs. The required sample for the UV-Vis investigation was therefore a DSSC half-cell composed only by the sensitized photoanode. The dye used for the staining of the photoanode was the organic dye **DF15** (*Figure 4.8*) that I synthetized in a previous work.[32]

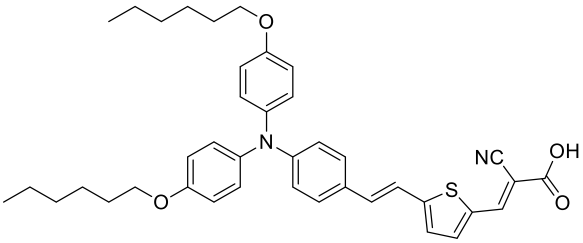

Figure 4. 8: ***DF15*** *was the organic sensitized selected for this investigation.*

The photoanode substrate is obtained by screen-printing a slurry containing TiO_2 nanoparticles, organic additives and the prepared colloids of core-shell AuNPs. For this study the general composition of the TiO_2 slurry[40] was revisited. The modification was motivated by the need to obtain films characterized by important features such as: good transparency, appreciable quantity of dye loaded and the possibility to calculate the concentration of AuNPs in the TiO_2 matrix. To achieve transparency of the thin films, special attention was given to the elimination from the slurry of micrometric aggregates responsible for light scattering. A powder of 13 nm TiO_2 NPs (P90, commercially available from Evonik Degussa) was used to prepare the slurry, after chemical and mechanical disaggregation in HNO_3/water solution by means of ultrasonication. The traded TiO_2 powder slurry was dispersed in EtOH and consistent amounts of ethylcellulose (EC) and terpineol provided the required viscosity for the slurry deposition. EtOH was used as solvent in order to prevent EC from precipitation, for the same reason, the content of water in the treated TiO_2 needed to be carefully minimized by several cycles of centrifuge sedimentation and redispersion in absolute EtOH. After homogenization of the obtained mixture of TiO_2 and organic additives, the colloids of core-shell AuNPs in EtOH were added so that the amount of gold was circa 0.1% w/w with respect to the amount of TiO_2. Finally, the volatile solvent was removed to obtain a pale pink slurry of AuNPs-doped semiconductor.

A reference sample without metal NPs was prepared using the same procedure, thus no metal NPs were added to the mixture prior to evaporation of EtOH, resulting in a bright white slurry.

Simple glass was chosen as a support for the Uv-Vis investigation. Before deposition of the semiconductor slurry, a compact layer of TiO_2 was deposited on the glass plates. To this end, titanium tetrachloride was reacted in water to obtain a titanium hydroxide solution, and the glass plates were immersed in such solution for 30′ at 70° C.[41] The obtained layer was less than 1μm thick, was completely transparent and had a relatively low surface area, so that the following dye uptake would be negligible on such substrate. On the other hand, it ensured a good connection of the semiconductor substrate with the supporting glass, giving a stable and robust sample.

The deposition of the semiconductor slurry on the treated glasses was carried out by means of a screen printer. To obtain the final semitransparent substrates, the screen printed glasses underwent an annealing procedure. During such procedure the temperature was gradually increased to obtain first, the evaporation of the solvents in the slurry, then the combustion of the EC and finally the creation of electrical connection between TiO_2 nanoparticles. The resulting substrate was found to have a micro and a macro porous structure making the active surface up to 1000 time larger than the sample area, necessary for a remarkable dye uptake. The thin films were found to be 5 μm thick and were analyzed by two-photon-induced luminescence spectroscopy to map the AuNPs distribution. (*Figure 4.9*) For this analysis the non-linear optic properties of the AuNPs were used: the films were shined with pulsed monochromatic light and the luminescence response due to two-photon absorption was detected. Moving the beam, a multidimensional map of the sample is obtained: a homogenous distribution of the AuNPs was found in all the samples, without noticeable aggregation.

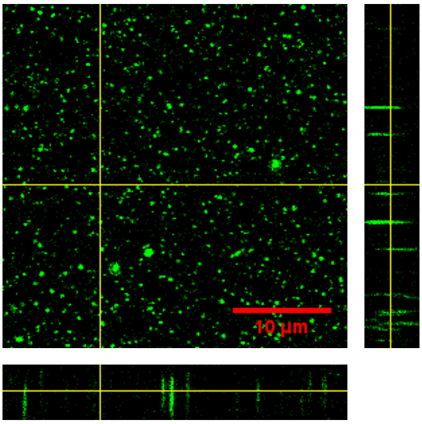

Figure 4. 9: ***2D mapping of a representative thin film sample.*** *2 photon induced luminescence spectroscopy of a 0,1% AuNPs@SiO_2-doped TiO_2 thin film of 35μm^2 Area, 256×256 pixels resolution. YZ projection is reported aside, XZ projection is reported below. The green luminescence response at 408 nm locates AuNPs cores.*

4.2.5. Dye staining

Once samples of homogenous and reproducible thickness were obtained, special care was dedicated to sensitize the films with the selected dyes. In particular, it was very important to use similar amounts of dye in each sample. This was a crucial step since, aiming to evaluate the NFE on dyes adsorbed on different supports, differences in the amount of dyes adsorbed on the films per surface unit would invalidate the comparison.

Dye **DF15**[32] (*Figure 4.8*) was used since its absorption band overlap with the plasmonic spectrum of the AuNPs, and its properties are well known in our group of research. A fixed volume of a standard EtOH solution of the dye was used for the staining process. The same freshly prepared standard solution was used for samples of the same batch of analysis. All samples were stained for 30 minutes, then the amount of dye absorbed on the film was evaluated by UV-Vis measurements.[2] As expected, a blue shift of a few nm of the maximum of absorption was observed. Indeed, the dependence of the spectroscopic features of carboxylic dyes from their degree of protonation has been already reported before.[32] The shift was attributed to deprotonation of dye molecules upon adsorption on the surface and, since it was found to be small and similar for all the samples, it was neglected. A precise quantification of the amount of dye absorbed on the film was possible from a comparison of the absorbance of the staining solution before and after the sensitization procedure. A decrease from 8% to 12% was detected for each of the staining solutions after the dying process. The calculated average amount of dye loaded on the samples was $(2.4 \pm 0.2) \times 10^{-8}$ mol cm^{-1}, such value is in agreement with the one calculated via **DF15** desorption, reported in the literature.[32]

4.3. Enhancement of light absorption

The transparency of the samples is crucial for the accuracy of the UV-Vis measurements. Indeed, if the thin semiconductor layers deposited on glass substrate were not perfectly transparent, reflection phenomena could alter the measured absorption values. In view of this, UV-Vis measurements on solid samples were performed using an integration sphere in the sample holder. Such tool allowed, for each sample, to record both the transmitted and the scattered light. It was therefore possible to calculate a corrected absorbance A^I taking into account the refracted light too (see *Eq. 4.2* where R is the reflectance and T is the transmittance, both reported in percentage). Moreover, to prove the homogeneity of the semiconductor layer the corrected absorbance was recorded three times for each sample placing the light beam in different positions on the film. Almost identical spectra for transmittance and reflectance were recorded for all the samples proving the homogeneity of the obtained surfaces; the average of three value of corrected absorbance was calculated for each sample.

$$A^I = 2 - \log(R + T) \qquad \textit{Eq. 4.2}$$

By measuring the corrected absorbance spectra before and after the staining procedure, it was possible to obtain, for each sample, the blank-corrected absorption spectra of the dye when attached to the semiconductor. The dye absorption spectra were corrected by the moles of dye adsorbed on the semiconductor, which were previously estimated from analysis on the staining solution. The obtained A^{II} value related to samples with the same type of semiconductor were averaged and plotted. as reported in *Figure 4.10.*

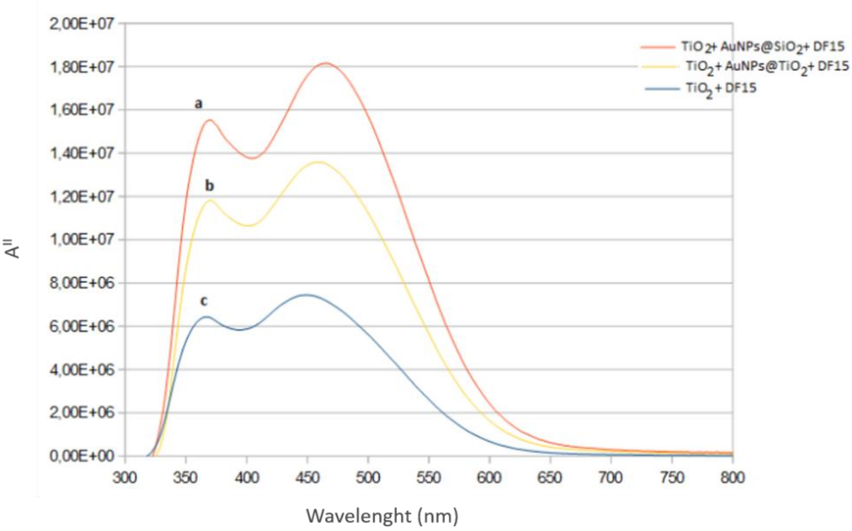

*Figure 4. 10: **UV-Vis characterization of dye DF15 adsorbed on different substrates**: a) AuNPs@SiO_2-doped TiO_2 thin layer; b) AuNPs@TiO_2-doped TiO_2 thin layer; c) pure TiO_2 thin layer. The absorbance values were divided by the number of moles of dye adsorbed on each film.*

From the results obtained it is clear that both AuNPs@SiO_2 and AuNPs@TiO_2 are capable of enhancing the light absorption of the dye adsorbed on the thin film. This result can be considered a very important proof of the effectiveness of the AuNPs to give NFE when organic dyes are used. More precisely, different enhancements of **DF15** absorption were found for the two core-shell systems: in particular, AuNPs@SiO_2 increased the absorption by 141% while AuNPs@TiO_2 improved the absorption by 81%. The reasons for this differences could be due to the nature of the shells: as described above the NFE is an electromagnetic feature, therefore dependent on physical properties of the media (such as the refractive index) and it is also directly correlated to the distance between the metal NPs surface and the chromophore. Even if the shell of the two synthetized systems is of comparable thickness the difference in refractive index of the two media (1.461 for SiO_2 and 2.488 for TiO_2)[7] could have been responsible for such differences.

Clearly, to prove how the dye response depend from the amount of AuNPs in the semiconductor, many samples of semiconductor doped with different concentrations of the same core-shell system should be compared. Therefore, by now, although we have proved that both AuNPs@SiO_2 and AuNPs@TiO_2 are capable of enhancing the light absorption of the dye adsorbed on the thin film, no correlation between the dye absorption enhancement and the amount of AuNPs in the substrate can be established.

Future investigations.

A more careful investigation on the effect that different concentrations of AuNPs in the thin layer would have on the absorbance of the dye, would be essential. At the same time, other organic dyes interacting with the NPs should be examined in order to claim a general behavior for this class of dyes. Of particular interest would be the correlation of such results with the position of the dye absorbance peak relative to the NPs plasmonic peak.

4.4. Experimental section

Preparation of AuNSeeds solution.[26]

Stock water solutions of $HAuCl_4$ (0.01 M, 0.25 mL) and CTAB (0.1 M, 9.75 mL) were mixed resulting in a dark yellow solution. Freshly prepared ice-cold $NaBH_4$ water solution (0.01 M, 0.60 mL) was added at r.t. under vigorous stirring. The mixture was stirred at r.t. for 3 hours affording a brownish solution. The NPs were not purified and the solution was used as such for the following step. TEM: Average diameter: 6.01 nm, Stnd. dev.: 1.17 nm.

Preparation of 30 nm AuNPs solution.[26]

Stock water solutions of $HAuCl_4$ (0.01 M, 10.0 mL) and CTAB (0.1 M, 24.3 mL) were mixed and diluted in water (475 mL) resulting in a yellow solution. A freshly prepared water solution of ascorbic acid (0.1 M, 37.5 mL) was added to the stirring mixture and de-coloration of the solution was observed. A freshly prepared seeds solution (0.27 mL) was added to the stirring solution, then the seeds were let grown overnight with no stirring. The obtained red solution was divided in samples for the purification procedure. Each 30 ml sample underwent centrifugation (8700 g, 30 min) and solvent replacement (CTAB 0.1 M, 30 ml), repeating this operation twice. UV-vis: λ_{max} = 528 nm, DLS: Average diameter: 42.14 nm, Stnd. dev.: 0.847 nm. TEM: Average diameter: 26.74 nm, Stnd. dev.: 3.84 nm.

Synthesis of AuNPs@SiO$_2$.

The 30 nm AuNPs solution (360 mL) was centrifuged (8700 g, 30 min) and the solvent was replaced with 0.2 mM CTAB water solution at pH = 10.5 (80 mL). A freshly prepared solution of MPTMS in dry *i*-PrOH (0.57% v/v, 0.80 mL) was added over 2 hours, the solution was gently shaked after each addition and left to set overnight at 37° C. The obtained purple-red solution was divided in samples for the purification procedure. Each 30 ml sample underwent centrifugation (3000 g, 10 min) and solvent replacement (CTAB 0.02 M, 6 ml), repeating this operation twice. UV-vis: λ_{max} = 531 nm. DLS: Average diameter: 45.40 nm, Stnd. dev.: 0.469 nm. TEM: Average core diameter: 27.40 nm, Stnd. dev.: 4.02 nm. Average shell thickness: 4.52 nm, Stnd. dev.: 0.53 nm.

Synthesis of AuNPs@TiO$_2$.

The 30 nm AuNPs solution (84 mL) was centrifuged (8700 g, 30 min) and the solvent was replaced with 0.2 mM CTAB water solution (15 mL). MAA (10.5 µL) was added under vigorous stirring. After stirring the mixture for 15 min at r.t., a solution of Ti(acac)$_2$(*i*-PrO)$_2$ in EtGly was slowly added overnight, letting the solution set at 37° C. The obtained purple-red solution was purified by centrifugation (3000 g, 5 min) and solvent replacement (CTAB 0.02 M, 6 ml), repeating this operation twice. UV-vis: λ_{max} = 534 nm. DLS: Average diameter: 61.98 nm, Stnd. dev.: 0.322 nm. TEM: Average core diameter: 30.52 nm, Stnd. dev.: 5.13 nm. Average shell thickness: 3.12 nm, Stnd. dev.: 0.41 nm.

Preparation of the semiconductor slurry.

TiO$_2$ NPs powder (P90 Evonik Degussa) (2 g) was suspended in a 0.1 M aqueous solution of HNO$_3$ (46 mL) and sonicated for 15 min. The suspension was concentrated by means of rotatory evaporation at 50° C under vacuum until only circa 20 g were left. The residue was centrifuged (2500 g, 10 min) and the solvent was replaced with EtOH (5 mL), repeating this operation tree times. The following solutions were then added to the TiO_2 suspension: EC 5-15 mPas in EtOH (10% w/w, 5.625 g) and EC 30-50 mPas in EtOH (10% w/w, 4.375 g); then terpineol (8.125 g) was added too. The mixture was homogenized alternating 15 minutes of sonication and 15 minutes of blending for tree times. If needed, the suspension of insulated AuNPs (12.6 mL) was added after changing the solvent to EtOH, then all the EtOH in the slurry was removed via rotatory evaporation.

Thin films deposition.

A set of 2.0 cm × 2.0 cm × 0.3 cm glass plates were cut to be used as supports for the films. The glasses were carefully washed and rinsed with water, acetone and EtOH. For the compact layer deposition, $TiCl_4$ (0.44 mL, 0.004 mol) was reacted in ice-cold water (100 mL) and the supports were treated with the resulting solution for 45 min at 70° C. The coated glasses were washed with water and EtOH, then a 1.0 cm × 1.0 cm spot of the semiconductor slurries was deposited in the middle of the functionalized face of each glass. The freshly spread semiconducting layer was left 5 min in a chamber saturated with EtOH fumes, then it was dried at 120° C for 30 min. The substrates were annealed in air keeping each of the following temperature steps for 30 min: 150° C, 350° C and 450° C. The samples were allowed to cool down slowly overnight. The dispersion of AuNPs on the semiconducting films was detected by 2D mapping for 2 photon induced luminescence (pump $\lambda = 817$ nm) on $35 \mu m^2$ sample area. (*Figure 4.9*)

Dye staining.

A stock staining solution of **DF15** in EtOH (2.0×10^{-4} M) was prepared. The dry thin films were sensitized with 1 mL of staining solution at r.t. for 30 min in the dark. The processed staining solution was collected, and the substrate was rinsed with EtOH to remove the excess of dye. The samples were dried and stored in the dark under nitrogen. UV-Vis measurement of the staining solutions before and after the dyeing procedure were carried out directly on the collected solution using a 0.3 cm optical path cuvette. Knowing the exact concentration of the original staining solution, the amount of dye attached to the semiconductor substrate was calculated by difference.

Solid state Uv/Vis spectroscopy.

Spectroscopic characterization of the samples was carried out before and after the staining procedure following the same protocol. The data recorded for the films before staining will be called blanks.

For the UV-Vis analysis of solid thin film the sample holder was equipped with an integration sphere. For each sample the transmittance spectrum was recorded three times for three different spots of the film and an average spectrum was calculated. The same procedure was followed for the reflectance spectrum, and then the corrected absorbance spectrum was calculated. From the difference between the corrected absorbance spectrum of the dyed thin film and the corresponding blank, the absorbance spectrum of the dye on TiO_2 substrate was obtained. The spectra were divided by a correction coefficient to account for the amount of dye loaded on the thin film, then results obtained for samples with the same kind of thin films were averaged.

References

[1] Dang X., Yi H., Ham M., Qi J., Yun D. S., Ladewski R., Strano M. S., Hammond P. T., Belcher A. M. Virus-templated self-assembled single-walled carbon nanotubes for highly efficient electron collection in photovoltaic devices. *Nat. Nanotechnol.* **2011**, *6*, 377–384.

[2] Choi H., Chen W. T., Kamat P. V. Know thy nano neighbor. Plasmonic versus electron charging effects of metal nanoparticles in dye-sensitized solar cells. *ACS Nano* **2012**, *6*, 4418–4427.

[3] Hutter E., Fendler J. H. Exploitation of localized surface plasmon resonance. *Adv. Mater.* **2004**, *16*, 1685–1706.

[4] Schuller J. A., Barnard E. S., Cai W., Jun Y. C., White J. S., Brongersma M. L. Plasmonics for extreme light concentration and manipulation. *Nat. Mater.* **2010**, *9*, 193–204.

[5] Kelly K. L., Coronado E., Zhao L. L., Schatz G. C. The Optical Properties of Metal Nanoparticles: The Influence of Size, Shape, and Dielectric Environment. *J. Phys. Chem. B* **2003**, *107*, 668–677.

[6] Mondes V., Antonsson E., Plenge J., Raschpichler C., Halfpap I., Menski A., Graf C., Kling M. F., Rühl E. Plasmonic electric near-field enhancement in self-organized gold nanoparticles in macroscopic arrays. *Appl. Phys. B* **2016**, *122*, 155.

[7] Sheehan S. W., Noh H., Brudvig G. W., Cao H., Schmuttenmaer C. A. Plasmonic Enhancement of Dye-Sensitized Solar Cells Using Core–Shell–Shell Nanostructures. *J. Phys. Chem. C* **2013**, *117*, 927–934.

[8] Brown M. D., Suteewong T., Kumar R. S. S., D'Innocenzo V., Petrozza A., Lee M. M., Wiesner U., Snaith H. J. Plasmonic dye-sensitized solar cells using core-shell metal-insulator nanoparticles. *Nano Lett.* **2011**, *11*, 438–445.

[9] Qi J., Dang X., Hammond P. T., Belcher A. M. Highly Efficient Plasmon-Enhanced Dye-Sensitized Solar Cells through Metal@Oxide Core–Shell Nanostructure. *ACS Nano* **2011**, *5*, 7108–7116.

[10] Hou W., Pavaskar P., Liu Z., Theiss J., Aykol M., Cronin S. B. Plasmon resonant enhancement of dye sensitized solar cells. *Energy Environ. Sci.* **2011**, *4*, 4650.

[11] Nahm C., Choi H., Kim J., Jung D. R., Kim C., Moon J., Lee B., Park B. The effects of 100 nm-diameter Au nanoparticles on dye-sensitized solar cells. *Appl. Phys. Lett.* **2011**, *99*,

[12] Chang S., Li Q., Xiao X., Wong K. Y., Chen T. Enhancement of low energy sunlight harvesting in dye-sensitized solar cells using plasmonic gold

nanorods. *Energy Environ. Sci.* **2012**, *5*, 9444.

[13] Standridge S. D., Schatz G. C., Hupp J. T. Toward plasmonic solar cells: protection of silver nanoparticles via atomic layer deposition of TiO_2. *Langmuir* **2009**, *25*, 2596–2600.

[14] Liu Z., Hou W., Pavaskar P., Aykol M., Cronin S. B. Plasmon resonant enhancement of photocatalytic water splitting under visible illumination. *Nano Lett.* **2011**, *11*, 1111–1116.

[15] Kawawaki T., Takahashi Y., Tatsuma T. Enhancement of dye-sensitized photocurrents by gold nanoparticles: Effects of plasmon coupling. *J. Phys. Chem. C* **2013**, *117*, 5901–5907.

[16] Kundu S., Patra A. Nanoscale Strategies for Light Harvesting. *Chem. Rev.* **2016**, acs.chemrev.6b00036. doi:10.1021/acs.chemrev.6b00036

[17] Muduli S., Game O., Dhas V., Vijayamohanan K., Bogle K. A., Valanoor N., Ogale S. B. TiO_2-Au plasmonic nanocomposite for enhanced dye-sensitized solar cell (DSSC) performance. *Sol. Energy* **2012**, *86*, 1428–1434.

[18] Standridge S. D., Schatz G. C., Hupp J. T. Distance dependence of plasmon-enhanced photocurrent in dye-sensitized solar cells. *J. Am. Chem. Soc.* **2009**, *131*, 8407–8409.

[19] Atwater H. A., Polman A. Plasmonics for improved photovoltaic devices. *Nat. Mater.* **2010**, *9*, 865–865.

[20] Kamat P. V., Shanghavi B. Interparticle Electron Transfer in Metal/Semiconductor Composites. Picosecond Dynamics of CdS-Capped Gold Nanoclusters. *J. Phys. Chem. B* **1997**, *101*, 7675–7679.

[21] Subramanian V., Wolf E., Kamat P. V. Semiconductor−Metal Composite Nanostructures. To What Extent Do Metal Nanoparticles Improve the Photocatalytic Activity of TiO 2 Films? *J. Phys. Chem. B* **2001**, *105*, 11439–11446.

[22] Peh C. K. N., KE L., Ho G. W. Modification of ZnO nanorods through Au nanoparticles surface coating for dye-sensitized solar cells applications. *Mater. Lett.* **2010**, *64*, 1372–1375.

[23] Wood A., Giersig M., Mulvaney P. Fermi level equilibration in quantum dot-metal nanojunctions. *J. Phys. Chem. B* **2001**, *105*, 8810–8815.

[24] Subramanian V., Wolf E. E., Kamat P. V. Catalysis with TiO_2/Gold Nanocomposites. Effect of Metal Particle Size on the Fermi Level Equilibration. *J. Am. Chem. Soc.* **2004**, *126*, 4943–4950.

[25] Oldfield G., Ung T., Mulvaney P. Au@SnO2 Core-Shell nanocapacitors. *Adv. Mater. (Weinheim, Ger.* **2000**, *12*, 1519–1522.

[26] Ruan Q., Shao L., Shu Y., Wang J., Wu H. Growth of Monodisperse Gold Nanospheres with Diameters from 20 nm to 220 nm and Their Core/Satellite

Nanostructures. *Adv. Opt. Mater.* **2014**, *2*, 65–73.

[27] Gao C., Vuong J., Zhang Q., Liu Y., Yin Y. One-step seeded growth of Au nanoparticles with widely tunable sizes. *Nanoscale* **2012**, *4*, 2875.

[28] Kimling J., Maier M., Okenve B., Kotaidis V., Ballot H., Plech A. Turkevich method for gold nanoparticle synthesis revisited. *J. Phys. Chem. B* **2006**, *110*, 15700–15707.

[29] Tung R. T. The physics and chemistry of the Schottky barrier height. *Appl. Phys. Rev.* **2014**, *1*,

[30] Chen S. Gold Nanoelectrodes of Varied Size: Transition to Molecule-Like Charging. *Science (80-.).* **1998**, *280*, 2098–2101.

[31] Mohamed H. H., Mendive C. B., Dillert R., Bahnemann D. W. Kinetic and mechanistic investigations of multielectron transfer reactions induced by stored electrons in TiO_2 nanoparticles: a stopped flow study. *J. Phys. Chem. A* **2011**, *115*, 2139–2147.

[32] Franchi D., Calamante M., Reginato G., Zani L., Peruzzini M., Taddei M., Fabrizi De Biani F., Basosi R., Sinicropi A., Colonna D., Di Carlo A., Mordini A. A comparison of carboxypyridine isomers as sensitizers for dye-sensitized solar cells: assessment of device efficiency and stability. *Tetrahedron* **2014**, *70*, 6285–6295.

[33] J. Turkevich; P.C. Stevenson; J. Hiller. Synthesis of Gold Nanoparticles Turkevich method. *Discuss. Faraday Soc.* **1951**, *11*, 55–75.

[34] Pileni M. P. Nanosized Particles Made in Colloidal Assemblies. *Langmuir* **1997**, *13*, 3266–3276.

[35] Noorduin W. L., Vlieg E., Kellogg R. M., Kaptein B. From Ostwald ripening to single chirality. *Angewandte Chemie - International Edition* **2009**, *48*, 9600–9606.

[36] Daniel M. C., Astruc D. Gold Nanoparticles: Assembly, Supramolecular Chemistry, Quantum-Size-Related Properties, and Applications Toward Biology, Catalysis, and Nanotechnology. *Chemical Reviews* **2004**, *104*, 293–346.

[37] Carrot G., Valmalette J. C., Plummer C. J. G., Scholz S. M., Dutta J., Hofmann H., Hilborn J. G. Gold nanoparticle synthesis in graft copolymer micelles. *Colloid Polym Sci* **1998**, *276*, 853–859.

[38] Liz-Marzán L. M., Giersig M., Mulvaney P. Synthesis of Nanosized Gold−Silica Core−Shell Particles. *Langmuir* **1996**, *12*, 4329–4335.

[39] Lee J.-W., Kong S., Kim W.-S., Kim J. Preparation and characterization of SiO_2/TiO_2 core-shell particles with controlled shell thickness. *Mater. Chem. Phys.* **2007**, *106*, 39–44.

[40] Ito S., Murakami T. N., Comte P., Liska P., Grätzel C., Nazeeruddin M. K., Grätzel M. Fabrication of thin film dye sensitized solar cells with solar to electric

power conversion efficiency over 10%. *Thin Solid Films* **2008**, *516*, 4613–4619.

[41] Choi H., Nahm C., Kim J., Moon J., Nam S., Jung D.-R., Park B. The effect of $TiCl_4$-treated TiO_2 compact layer on the performance of dye-sensitized solar cell. *Curr. Appl. Phys.* **2012**, *12*, 737–741.

Chapter 5

Ionic Liquids

Transient absorption spectroscopy for the evaluation of the reduction of recombination rate due to compensation of the injected electrons.

Saavedra Becerril, V.; Franchi, D.; Abrahamsson M. Ionic Liquid-Induced Local Charge Compensation: Effects on Back Electron-Transfer Rates in Dye-Sensitized TiO_2 Thin Films. *J. Phys. Chem. C* **120**, 20016–20023 (2016).

5.1. Introduction

The overall efficiency of DSSCs depends on the light harvesting efficiency of the photoactive components, but also on the individual efficiencies of the various interfacial charge-transfer processes that occur following light absorption.[1–3] The details of photocurrent generation and enhancement have been deeply studied,[4–7] but much insight is still needed for a better understanding of the recombination processes. Further studies are required before the back electron-transfer reaction from TiO_2 conduction band electrons to the oxidized dye can be controlled and exploited, and before we fully understand the mechanisms behind the electrostatic interactions taking place at the TiO_2–dye–electrolyte interface.[8] Understanding and controlling back electron transfer is crucial both for V_{OC} optimization.[1,9] Many successful approaches to decrease the rate of back electron transfer are based on dye structure modifications. For example, the use of sensitizers that undergo intramolecular hole-transfer reactions subsequent to electron injection typically results in long-lived charge separation; however, this often occurs at the expense of considerable losses in the free energy stored in the charge-separated state.[10,11] Another strategy that has been pursued is to increase the distance between the TiO_2 surface and the chromophore by the introduction of spacers; incorporation of phenylene-ethynylene spacers can slow back electron transfer without concomitant free energy losses; however, this sometimes occurs at the cost of low injection efficiencies.[12,13]

In this study, the simpler approach of changing the environment at the interface rather than modifying the dye structure was chosen, by introducing a pure ionic liquid (IL) electrolyte. This strategy provides the ability to modify the recombination kinetics and gain insight about the effects that large ionic liquid cations can have at the charged TiO_2 interface. Several reports on the effect of ILs on the electron-transfer processes in DSSC have been published;[14–17] however, none of them has solely focused on recombination, also known as the back electron-transfer reaction. Characterization of DSSCs with IL electrolytes has shown that electron recombination is accelerated and regeneration is slowed down compared to DSSCs with organic solvent-based electrolytes. This is the case for DSSCs using either organic dyes or ruthenium complexes as photosensitizers.[15,17,18] The origin of these effects is not yet fully understood, and speculations regarding diffusion limitations caused by increased solution viscosity have been disproven as the sole reason for the observed behavior.[17]

Clearly, there is a strong need for solid mechanistic insights of such phenomenon, especially because minimizing recombination losses is crucial not only for efficient electricity generation in DSSCs but also for applications where multiple electron transfer is required. Thus, it becomes necessary to expand our understanding of the influence of ILs on the interfacial electron-transfer processes.

The evaluation of the effects of ionic liquids on recombination processes was performed during a stay at Chalmers University of Technology (Göteborg, SE) in collaboration with Valeria Saavedra Becerril and her supervisor Maria Abrahamsson from the department of Chemistry and Chemical Engineering. In this work, we have measured recombination kinetics using single-wavelength transient absorption spectroscopy in dye–TiO_2 samples in contact with ionic liquid electrolytes. Our results show that IL electrolytes can significantly slow the back electron-transfer rate without considerably affecting electron injection efficiencies; however, this appears to be strongly dependent on the electronic structure of the dye.

5.1.1. Transient absorption spectroscopy

Time-resolved spectroscopies allow recording the evolution of an optical feature of a sample in a period of time. In this work, the variation of absorbance at a particular wavelength was measured as a function of time after excitation of the sample: such time-resolved method is called single-wavelength transient absorption spectroscopy. The analytical timeframe ranged from nanoseconds to microseconds as the light for excitation ('pump') was provided by a pulsed laser that, together with the appropriate detector, allowed to study processes occurring on time scales as short as 10^{-9} seconds. In a typical experiment, a probe light records the ground-state absorbance of the sample, then a pump pulse excites the latter. Immediately after excitation, the probe pulse striking the sample records the difference of absorbance at a specific wavelength, which is then plotted versus time to study the dynamics of decay of the excited state. The wavelength probed is chosen according to a preliminary analysis: the whole spectrum is recorded both for the ground state and for the excited one and the differential absorption spectrum is calculated with *Eq. 5.1*. In the ΔA spectrum, the probing wavelength is chosen to aim for the most intense signal and to avoid optical interferences such as dye-stimulated emission and scattered light from the pumping channel. The evolution of the system with time can be studied by measuring the absorbance decrease in correspondence of the peaks or its growth in correspondence of the bleach. While at the bleaching wavelength the absorption of the excited state occurs, the peaks refer to depleted the ground state absorption. (*Figure 5.1*)

$$\Delta A = A_{after\ pump} - A_{ground\ state} \qquad Eq. 5.1$$

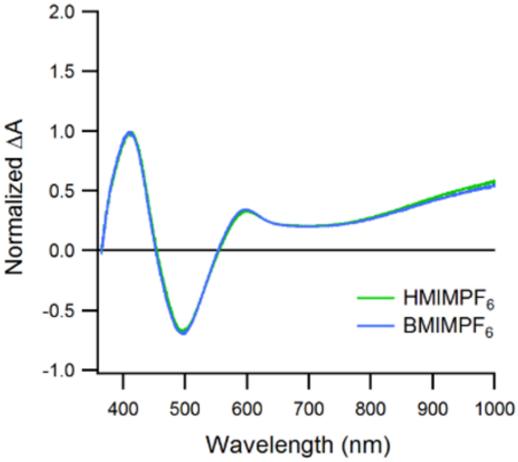

Figure 5. 1: ***Example of differential absorption spectrum****: normalized spectra of ΔA for* ***D35****/TiO$_2$, in contact with different ILs, after pulsed 425 nm excitation. The bleach is due to the absorption of the oxidized form of the dye (excited state).*

5.2. Method

The kinetics of recombination processes can be measured on dye-sensitized semiconductor thin films rather than full devices to better assess the mechanism of the back electron-transfer process. In this work we have measured back electron-transfer kinetics using transient absorption spectroscopy in dye–TiO$_2$ samples with ionic liquid electrolytes. As explained in the previous section, aiming for spectroscopic characterization of solid thin films, special attention was given to obtain high samples transparency and reproducibility. Such features of the samples were obtained using a commercially available TiO$_2$ paste. Concerning the sensitizers, we chose to work with well-known and well-characterized dyes, one organic dye (**D35**) and two Ru(II)-based dyes, **N3** and [Ru(2,2′-Bipyridine-4,4′-dicarboxy)$_3$]$^{2+}$ ([Ru(2dcb$_3$]$^{2+}$). **D35** was chosen because of its appreciable stability, good device performance, and ultrafast electron injection into TiO$_2$ conduction band within tens of femtoseconds, even under air.[19,20] **N3** was chosen for similar reasons as **D35,** while [Ru(dcb)$_3$]$^{2+}$ was employed as a model dye for all the Ru^{2+} dyes investigated as sensitizers for DSSCs.[21] Once the sensitized films were obtained, the surface coverage was evaluated *via* spectroscopic characterization of the solid samples. Kinetic studies were preceded by steady-state UV-Vis characterization of the dye-sensitized TiO_2 films in contact with the electrolytes. The ionic liquids used are three imidazolium-based ILs: 1-butyl, 1-hexyl, and 1-octyl-3-methylimidazolium hexafluorophosphate ($BMIMPF_6$, $HMIMPF_6$, and $OMIMPF_6$ respectively) (*Figure 5.2*). Neat acetonitrile (ACN) and 0.1 M $LiClO_4$ in ACN were used as reference electrolytes. Nanosecond transient absorption measurements were conducted on the dye-sensitized TiO_2 films in contact with the different electrolytes and second order exponential decay fitting of the recorded data gave the rate constants for the kinetics of recombination.

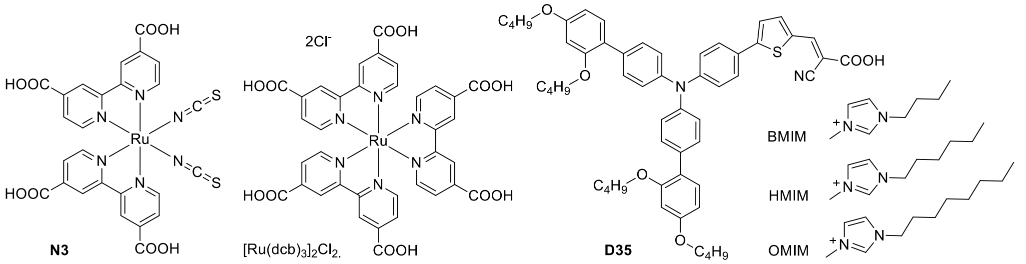

Figure 5. 2: ***Dyes and IL Cations Used in This Study****: from left to right:* ***N3****; [Ru(dcb)*$_3$*]Cl*$_2$*;* ***D35****; and the 1-butyl-3-methylimidazolium (BMIM), 1-hexyl-3-methylimidazolium (HMIM), and 1-octyl-3-methylimidazolium (OMIM) cations.*

5.2.1. Sample preparation

Transparent mesoporous nanocrystalline TiO_2 films of 1 cm^2 area, ca. 6 μm thickness and average nanoparticle diameter of 20 nm were prepared by doctor-blading technique on glass-FTO substrates using a commercially available TiO_2 paste. After paste deposition, the samples were progressively heated to 450° C in air flow. Dye baths contained either 0.3 mM **D35**, 0.1 mM **N3**, or 0.1 mM [($Ru(dcb)_3$)Cl_2] in ethanol or methanol. Prior to sensitization, the films were heated to 80° C. For spectroscopic measurements, a drop of the electrolytes was added on top of the samples and a microscope glass coverslip was placed on top of them. Surface coverages were determined by measuring the absorption spectrum of the dye bath solution before and after sensitization of the films. Using the molar absorption coefficients of the dyes, the number of molecules on the 1 cm^2 film was determined.

5.2.2. Ground-State Absorption Spectroscopy

In *Table 5.1* and *Figure 5.3* the electronic absorption data of the dye–TiO_2 assemblies in contact with the different electrolytes and solvents are summarized. For the Ru-based photosensitizers, very small spectral shifts were observed upon addition of the different solvents, with the exception of **N3** in acetonitrile, for which a more pronounced red-shift was observed. For **D35,** the absorption in neat acetonitrile is the most blue-shifted with λ_{max} of 460 nm, consistent with previously reported results.[20,22] All the other **D35**/TiO_2 samples display bathochromic shifts with respect to acetonitrile, with minor individual differences. This suggests that the ground-state interactions are similar in all electrolytes containing a significant amount of ionic species. We note that the small but significant red-shift of the **D35**/TiO_2 absorption peak upon addition of the ILs increases with the length of the alkyl chain in the alkyl-imidazolium cations.

*Table 5. 1: **Ground state characterization**: maximum absorption wavelengths (nm) of the dyes adsorbed on TiO_2 thin films and in the environments indicated. Small differences were found when samples were in contact with electrolytes with significant amounts of ionic species, suggesting similar ground-state interactions.*

Dye	Air	ACN	$LiClO_4$	$BMIMPF_6$	$HMIMPF_6$	$OMIMPF_6$
D35/TiO_2	465	460	479	471	473	478
N3/TiO_2	524	534	527	524	525	525
$[Ru(dcb)_3]^{2+}/TiO_2$	452	467	467	467	468	464

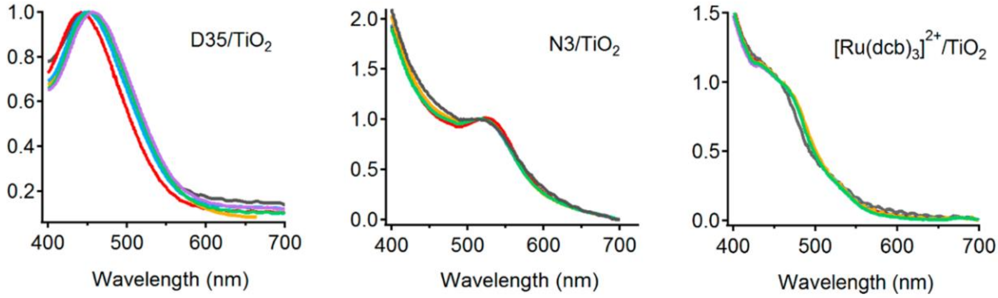

*Figure 5. 3: **Ground state characterization**: from left to right, electronic absorption spectra of **D35**/TiO_2, **N3**/TiO_2, and $[Ru(dcb)_3]^{2+}/TiO_2$ in air (gray); neat ACN (red); 0.1 M $LiClO_4$/ACN (yellow); and ILs $BMIMPF_6$ (blue), $HMIMPF_6$ (green), and $OMIMPF_6$ (purple). Spectra were normalized to a maximum absorption of 1.0 for the dye peak.*

5.2.3. Kinetic studies

The interfacial back electron-transfer kinetics were monitored with single-wavelength transient absorptions measured on the sensitized thin films. Surface coverages varied between 10^{-7} and 10^{-9} mol/cm^2 depending on the dye. The laser pulse intensity was adjusted according to the absorbance of the samples at the excitation wavelength. Also, for all dyes care was taken to measure samples having absorbance as similar as possible. Samples with absorbance variations higher than 10% against the average were not considered for measurement. This compensates for the difference in surface coverages with the purpose of obtaining comparable kinetics for all the three dyes studied. By doing this, a similar density of injected electrons in the conduction band should be obtained,[23] accounting for the strong dependence of electron dye recombination kinetics upon electron density in the conduction band of the semiconductor.[3,24]

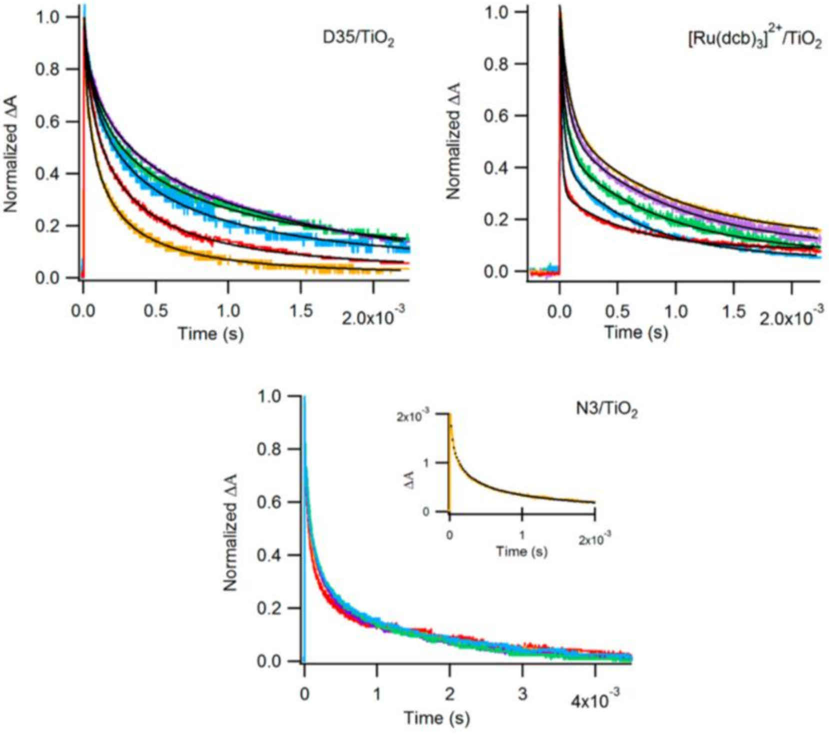

Figure 5. 4: ***Back-electron transfer kinetics****. Normalized representative individual traces and corresponding fits measured by single-wavelength transient absorption after pulsed 425 nm excitation. The traces were obtained with photodiode detection at 750 nm for* ***D35****/TiO_2, 500 nm for $[Ru(dcb)_3]^{2+}$/TiO_2, and 750 nm for* ***N3****/TiO_2 in neat ACN (red); 0.1 M $LiClO_4$/ACN (yellow); and ILs $BMIMPF_6$ (blue), $HMIMPF_6$ (green), and $OMIMPF_6$ (purple). The inset in the* ***N3****/TiO_2 graph shows the KWW fit to one of the curves.*

Figure 5.4 shows representative back electron-transfer kinetic traces with the corresponding fits. The decays of **D35** and **N3** were probed at 750 nm, where the oxidized forms of both dyes have strong positive absorption signals. A weak absorption from electrons accumulated in the conduction band could have a very small contribution[20] to this signal, but because care was taken to minimize the number of injected electrons this contribution should be negligible. The oxidized form of $[Ru(dcb)_3]^{2+}$ exhibits a very broad and weak absorption band above 600 nm; therefore, the kinetics were probed at 500 nm instead, corresponding to the ground-state bleach. Although electron injection from $[Ru(dcb)_3]^{2+}$ to TiO_2 is considerably less efficient than in **N3** and **D35**, we clearly observe the formation of oxidized $[Ru(dcb)_3]^{2+}$ based on the decay time of the ground-state bleach. (*Figure 5.4*) As can be readily seen in *Figure 5.4*, the back electron-transfer kinetics were visibly slower in all the ILs compared to acetonitrile for both **D35** and $[Ru(dcb)_3]^{2+}$. In contrast, **N3**-sensitized thin films show no appreciable differences in the kinetics observed regardless of the solvent used. We did not observe significant differences in the initial values of ΔA signals, even at the best time resolution used, in any of our samples. Therefore, we do not have reasons to believe that the presence of ionic liquids had a significant effect on the quantum yields of injection because that would typically result in easily detectable differences in ΔA amplitudes.[24]

5.2.4. Data fitting

The decay traces could not be fitted to a mono-exponential decay model; instead, a stretched exponential function, obtained by inserting a fractional power law into the exponential function (*Eq. 5.2*), was used. This fitting law is known as Kohlrausch-Williams-Watts (KWW) kinetic model,[21,22] and is often more appropriate in modeling relaxation processes. In part, this is a consequence of the fact that, because the decay curve depends on the entire spectrum of relaxation processes, its structure will be non-linear and not purely exponential. A stretched exponential model that provides for a small deviation from the pure exponential decay, is more adequate for the kinetic fit.

$$f_\beta(t) = EXP\left(-t^\beta\right) \qquad \textit{Eq. 5.2}$$

$$I = \left(I_0 - I_f\right) EXP\left[-(k_{obs}\, t)^\beta\right] + I_f \qquad \textit{Eq. 5.3}$$

$$\langle \tau_{KWW} \rangle = \frac{1}{k_{obs}\, \beta}\, \Gamma\left(\frac{1}{\beta}\right) \qquad \textit{Eq. 5.4}$$

The KWW kinetic model is described by *Eq. 5.3*, where I_0 and I_f are the initial and final amplitudes, respectively, and β is the coefficient of deviation from the mono-exponential decay, taking values between zero and unity.[12,25] Given the function $f_\beta(t)$ as a differential distribution and the argument t as a time, the area under the curve is interpreted as a mean relaxation time $\langle\tau_{KWW}\rangle$. Therefore, the first moment of the KWW function is given by *Eq. 5.4*, where Γ is the gamma function.[26] Representative back electron-transfer rate constants, k_{KWW}, were taken as the reciprocal of $\langle\tau_{KWW}\rangle$.

Another adequate description of the collected recombination data is a bi-exponential decay model. In this case, the deviation from a mono-exponential decay is explained by the conjunction of two decay processes, each one having its own probability to occur and its relaxation time. characterized by an exponential decay.

$$I = I_0 + A_1\,EXP\left[\frac{-(t-t_0)}{\tau_1}\right] + A_2\,EXP\left[\frac{-(t-t_0)}{\tau_2}\right] \qquad \textit{Eq. 5.5}$$

$$k_1 = {}^{1}/_{\tau_1}\ ,\quad k_2 = {}^{1}/_{\tau_2} \qquad \textit{Eq. 5.6}$$

The bi-exponential decay model is reported in *Eq. 5.5* where τ_1 and τ_2 are the values of the decay time constants and A_1 and A_2 their corresponding amplitudes. The extracted decay rate constants, k_1 and k_2, are calculated as the inverse of the decay time constants obtained from the fits (*Eq. 5.6*) The rate constants extracted from the various decay models are summarized in *Table 5.2* and *Table 5.3*.

Table 5. 2: ***Back electron transfer rate constants**. k_{KWW}, and β Parameters obtained from KWW model fitting of transient absorption data of **D35**/TiO_2 and **N3**/TiO_2 samples in the electrolyte indicated. The indicated uncertainties represent the standard deviation obtained from averaging individual fits of single-wavelength transient absorption decays from triplicate samples.*

	D35		N3	
Electrolytes	k_{KWW} (10^3 s^{-1})	β	k_{KWW} (10^3 s^{-1})	β
ACN	11.2 ± 1.3	0.42 ± 0.01	12.6 ± 2.4	0.24 ± 0.02
$LiClO_4$	26.1 ± 8.8	0.42 ± 0.08	20.2 ± 3.2	0.24 ± 0.02
$BMIMPF_6$	4.3 ± 2.7	0.41 ± 0.07	15.3 ± 5.4	0.29 ± 0.06
$HMIMPF_6$	7.5 ± 2.2	0.41 ± 0.06	16.8 ± 3.1	0.24 ± 0.05
$OMIMPF_6$	2.8 ± 0.7	0.48 ± 0.09	18.3 ± 5.3	0.30 ± 0.02

Table 5. 3: ***Back electron transfer rate constants****. Parameters obtained from double exponential fitting of transient absorption data of* ***D35****/TiO_2 and $[Ru(dcb)_3]^{2+}$/TiO_2 samples in the electrolyte indicated. The indicated uncertainties represent the standard deviation obtained from averaging individual fits of single-wavelength transient absorption decays from triplicate samples.*

	D35				**$[Ru(dcb)_3]^{2+}$**			
Electrolytes	A_1 (%)	A_2(%)	k_1 (10^3 s^{-1})	k_2 (10^3 s^{-1})	A_1 (%)	A_2(%)	k_1 (10^3 s^{-1})	k_2 (10^3 s^{-1})
ACN	43	57	1.4 ± 0.43	1.9 ± 0.28	68	32	4.1 ± 0.51	1.5 ± 0.18
$LiClO_4$	50	50	2.8 ± 1.0	2.8 ± 0.53	46	54	1.2 ± 0.09	0.98 ± 0.13
$BMIMPF_6$	38	62	1.3 ± 0.5	1.3 ± 0.28	58	42	3.3 ± 0.29	2.2 ± 0.73
$HMIMPF_6$	44	56	1.7 ± 0.51	1.4 ± 0.16	55	45	2.1 ± 0.2	1.3 ± 0.15
$OMIMPF_6$	37	63	0.99 ± 0.74	0.92 ± 0.44	52	48	1.6 ± 0.33	1.1 ± 0.05

5.3. Results and discussion

The **N3**/TiO_2 samples were all better described by the KWW model, and attempts to use the bi-exponential model yielded nonsensical output. In contrast, **D35**/TiO_2 decay traces could be satisfactorily fitted to both models but were better described by the KWW model. A detailed analysis of the obtained β values suggests no significant difference in the distribution of rate constants for a given dye, which makes the comparison of the obtained rate constants straightforward and provides evidence that the kinetic model is robust. However, the β-values for **N3**, around 0.25, are lower than the β-values for **D35**, indicating a slightly different distribution of rate constants and consequently different interfacial properties in the two cases. The extracted rate constants also confirm the visual inspection, that charge recombination in IL electrolytes is slowed by at least a factor of 4 and 2 compared to $LiClO_4$ and neat acetonitrile, respectively. Furthermore, the extracted rate constants confirm that the recombination is faster in **N3** compared to **D35**, in all ILs, while in acetonitrile-based electrolytes they are very similar, a clear indication that the ILs affect the recombination rates differently depending on dye structure. The small differences between the extracted rate constants for a specific dye in the different ILs provide no evidence for a clear trend with regards to back electron-transfer rate and size/bulkiness of the IL cation. However, we do note that the slowest back electron-transfer for both **D35** and $[Ru(dcb)_3]^{2+}$ is observed in the presence of the bulkiest cation, $OMIM^+$.

Fitting the $[Ru(dcb)_3]^{2+}$ decay traces with the KWW model resulted in large and nonsystematic variations in β which could not be related to differences between samples; therefore, the model was not considered robust in this case. Instead, the experimental data was well-described by the double-exponential model (*Eq. 5.5*). As mentioned above, the **D35** data could be reasonably well reproduced also by a bi-exponential model, and to enable straightforward comparisons between **D35** and $[Ru(dcb)_3]^{2+}$, the **D35** data were also fitted to this model. Small differences are found when comparing the values of the rate constants for $[Ru(dcb)_3]^{2+}/TiO_2$ in neat acetonitrile and upon addition of the ILs. The differences in the relative amplitudes of k_1 and k_2 confirm that back electron transfer is slower in the presence of ILs. (*Table 5.3)* Summarizing these data, we can conclude that slowest decay is observed with $OMIMPF_6$, for both **D35** and $[Ru(dcb)_3]^{2+}$ samples. However, the effect of Li^+ is not the same for all the dyes. The data analysis provided above confirms that charge recombination in **D35** and $[Ru(dcb)_3]Cl_2$ sensitized TiO_2 becomes slower in the presence of the ILs studied here. Given the consistency of our data, the 2- to 4-fold change in charge recombination rate constants observed here should be considered a significant change. Because the same was not observed for **N3** sensitized films, a detailed discussion about the possible reasons for the observed behavior is warranted. Some additional considerations regarding the system studied can be made.

Cations intercalation

The concentration of electrons in the conduction band is dependent not only on the irradiation power but also on the electron injection efficiencies for a specific dye. This process is known to be affected by the use of additives in the electrolyte such as Li^+ and 4-TBP by either shifting the TiO_2 conduction band energetics[24,27–30] or by surface interactions caused by adsorption of molecules at the TiO_2 surface.[28,31,32] Given the experimental conditions of our study, the differences in back electron-transfer rates observed with different IL cations cannot be attributed to a conduction band shift. To the best of our knowledge, the few reports regarding conduction band energy shifts in DSSCs with IL electrolytes either involve Li^+ [33] or are anion-correlated.[34] Moreover, a general conduction band edge shift caused by IL species should similarly affect the interfacial electron dynamics for all the dyes because the generality of this effect has been confirmed through years of observations.[24,27–32,34] The addition of Li^+ had a similar effect on both **D35** and **N3**, where approximately a 2-fold increase in k_{KWW} is observed in comparison to neat acetonitrile. Thus, a Li^+ induced conduction band edge shift could at least explain the faster kinetics observed for **D35**/TiO_2 and **N3**/TiO_2 in $LiClO_4$/ACN, assuming that the charge recombination occurs in the Marcus inverted region.[35,36] From this, it follows that a conduction band edge shift would produce an effect of similar magnitude and direction in both **D35**/TiO_2 and **N3**/TiO_2 samples. Thus, a conduction band edge shift effect cannot justify the slower recombination observed in **D35**/TiO_2 with ILs, given that the effect of ILs in the k_{KWW} of **D35**/TiO_2 and **N3**/TiO_2 is the opposite. The slower recombination kinetics in $[Ru(dcb)_3]^{2+}$/TiO_2 with ILs compared to that in neat acetonitrile suggests that the electronic structure of the dye plays an important role. However, the effect of Li^+ observed for $[Ru(dcb)_3]^{2+}$/TiO_2 is somewhat surprising.

Viscosity

The general high viscosity of IL electrolytes is directly related to changes in the electron dynamics in IL-DSSCs.[37,38] Although ionic diffusion is not a limiting process for interfacial charge recombination, we still wanted to make sure that our observations would not have any direct relationship with the general physical properties of the electrolyte. For this purpose, we also measured the back electron-transfer kinetics of **D35**/TiO_2 thin films in a polymer-based gel with a molar composition of 0.1 polyacrylonitrile (PAN), 0.41 ethyl carbonate, and 0.38 propyl carbonate. The viscosity of this gel is at least 3 orders of magnitude higher than that of the ILs.[39–41] The recombination kinetics in the polymer are very similar to those in neat acetonitrile (*Figure 5.5 Right*). Therefore, we can confirm that the rheological properties of the electrolytes do not affect charge recombination dynamics.

Dye regeneration

We also wanted to ensure that pure IL electrolytes do not generally prevent reactivity; therefore, the decay of **D35**/TiO_2 samples was measured using $BMIM^+$ with the non-innocent anions I^- and SCN^- (*Figure 5.5 Left*). Because both I^- and SCN^- are known to regenerate the oxidized dye, and I^- more efficiently than SCN^-, faster decay of the oxidized dye signal is expected.[42–44] This was indeed observed; in fact, transient absorption kinetics in BMIMI suggested that regeneration of **D35** was complete in 2 μs (*Figure 5.5 Left*). A bleaching of the ground-state absorption of the dye is observed after the regeneration reaction is finished, which Wang *et al.* have previously attributed to formation of the reduced dye formed by the reaction of the excited dye with the high concentration of iodide anions.[44]

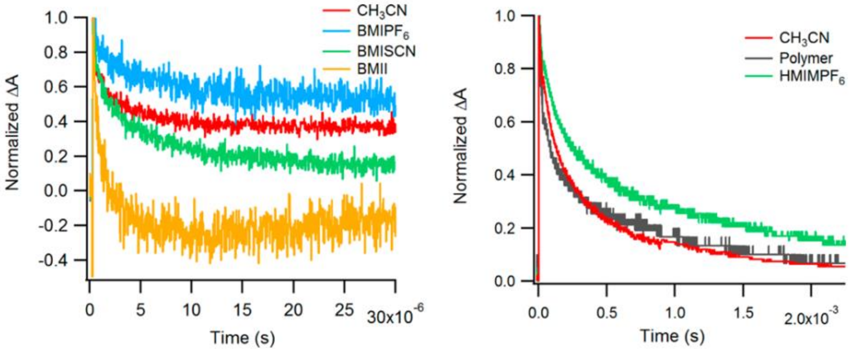

Figure 5. 5: Single-wavelength transient absorption after pulsed 425 nm excitation for ***D35****/TiO_2 thin films with the various electrolytes. Left:* ***Regeneration kinetics****: individual traces measured by at 750 nm (photodiode detection). In presence of non-innocent cations, a much faster decay is observed. Right:* ***Effect of viscosity on recombination kinetics****: individual traces measured at 600 nm (PMT detection). The high viscosity polymeric electrolyte does not affect the recombination kinetic.*

5.4. Proposed mechanism

Thus, in view of the previous discussions, it can be safely concluded that charge recombination becomes slower in the presence of the ILs studied here when innocent anions such as PF_6^- are employed. This would point to an interfacial effect where the bulky, asymmetric, and highly available cations are rearranged and electroadsorbed at the charged TiO_2 surface modifying the interaction between CB electrons and oxidized dye molecules. Considering the size of the cations and the low surface coverage of our sample, it is likely that the cations penetrate the dye layer and adsorb at free TiO_2 sites. Compared to the small, solvated lithium ions in organic solvent electrolytes, bulky cations and molecules should be more prone to form layered, compact structures at the charged interface.[45] Charge screening due to the creation of a bulky insulating network on the TiO_2 surface has been suggested before, with the use of CDCA as a surface coadsorbent.[46] As a result, a change in electronic coupling between the electrons in the conduction band and the oxidized dye molecules is expected.[28] This affects the dynamics of back electron transfer. (*Figure 5.6*) When Meyer and collaborators first demonstrated Stark effects at dye-sensitized TiO_2, they predicted that screening of electric fields by chemical species should have an influence on the lifetime of the charge-separated state.[47] Our results are in agreement with this statement. Ionic rearrangement in DSSCs has been suggested to take place on time scales ranging from 10^{-6} to 10^{-5} seconds[48] and has been experimentally confirmed by Stark effect dynamic studies.[49] Thus, a correlation between back electron-transfer dynamics and local charge compensation effect is a reasonable way to explain the observed results.

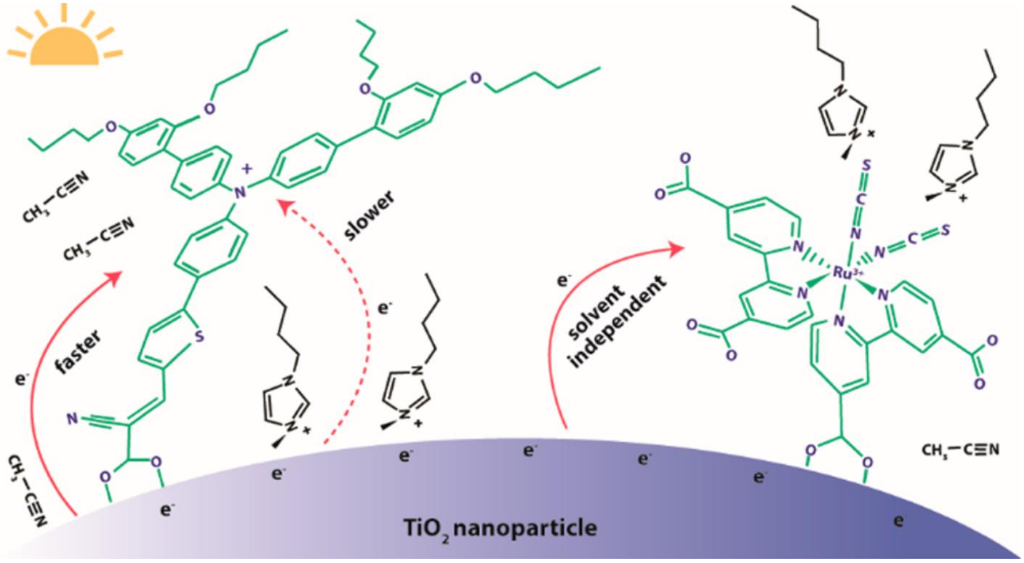

Figure 5. 6: ***Graphical representation of the proposed mechanism****: IL cations electrosorbed on TiO_2 surface can provide local charge compensation for the injected electrons. This affects the kinetics of recombination process in the case of* ***D35****/TiO_2 and $[Ru(bcb)_3]^{2+}$/TiO_2 but does not have effects on the* ***N3****/TiO_2 system. In this case, a stronger interaction of the IL cations with the SCN^- ligands is proposed.*

Electrosorption of cations at the TiO_2 surface to compensate the charge of injected electrons has been reported before, and although the exact time that cations take to locally reorganize at the charged TiO_2 surface is unknown, it is reported that they can remain for a time longer than typical interfacial recombination times before the electrical field is reversed.[8] Possible steric and/or electrostatic effects of the IL cations at the TiO_2 surface might be very similar for the **D35** and $[Ru(dcb)_3]^{2+}$ compounds, neither of which contain charged ligands; therefore, smaller interactions with the IL could be expected. However, in **N3**, it is possible that the IL cations will have stronger interactions with the SCN^- ligands rather than at the charged TiO_2 interface, making the accumulation of cations at the TiO_2 surface less efficient. To explain the behavior for **N3**/TiO_2 samples, a deeper analysis is needed. The structure of the dye as well as how it arranges at the TiO_2 surface can possibly prevent the IL cations from penetrating the surface. Therefore, aggregation and π-stacking effects should be taken into consideration. It is known that planar dyes, and specifically D−π−A systems such as **D35**, are much more susceptible to aggregate and form π-stacks than pseudo-octahedral dyes such as **N3**.[50–52] Therefore, aggregation effects are more likely to take place in **D35** rather than **N3** samples, considering also the higher surface coverage obtained in **D35**/TiO_2 samples. Thus, aggregation is not likely to be the reason why we did not observe the same effect in **D35** and **N3** samples with ILs. Both **N3** and $[Ru(dcb)_3]^{2+}$ are pseudo-octahedral complexes, but their ligands have very different electronic properties, and a detailed comparison might provide useful insight. The observed behavior could be due to the presence of negatively charged SCN^- ligands in **N3**, which would be in agreement with the hypothesis of an electrostatic effect at the dye−TiO_2−electrolyte interface being the main reason for the observed behavior.

In the above analysis, we have provided arguments to explain the unexpected dye-structure-dependent dynamics of charge recombination observed in this study. Effects from differences in injection efficiency, aggregation, viscosity, dye geometry, and secondary chemical reactions are dismissed both from our experimental observations and literature findings. Thus, an electrostatic effect at the interface is considered to explain our observations.

References

[1] Hagfeldt A., Boschloo G., Sun L., Kloo L., Pettersson H. Dye-Sensitized Solar Cells. *Chem. Rev.* **2010**, *110*, 6595–6663.

[2] O'Regan B. C., Durrant J. R. Kinetic and Energetic Paradigms for Dye-Sensitized Solar Cells: Moving from the Ideal to the Real. *Acc. Chem. Res.* **2009**, *42*, 1799–1808.

[3] Listorti A., O'Regan B., Durrant J. R. Electron Transfer Dynamics in Dye-Sensitized Solar Cells. *Chem. Mater.* **2011**, *23*, 3381–3399.

[4] Liu Y., Fire A. Z., Boyd S., Olshen R. A. Estimating Clonality. *Proc. Natl. Acad. Sci. U. S. A.* **2014**, *1*, 2–7.

[5] Albero J., Atienzar P., Corma A., Garcia H. Efficiency Records in Mesoscopic Dye-Sensitized Solar Cells. *Chem. Rec.* **2015**, *15*, 803–828.

[6] Qi J., Dang X., Hammond P. T., Belcher A. M. Highly Efficient Plasmon-Enhanced Dye-Sensitized Solar Cells through Metal@Oxide Core–Shell Nanostructure. *ACS Nano* **2011**, *5*, 7108–7116.

[7] Wang H., Wang B., Yu J., Hu Y., Xia C., Zhang J., Liu R. Significant enhancement of power conversion efficiency for dye sensitized solar cell using 1D/3D network nanostructures as photoanodes. *Sci. Rep.* **2015**, *5*, 9305.

[8] Yang W., Pazoki M., Eriksson A. I. K., Hao Y., Boschloo G. A key discovery at the TiO_2 /dye/electrolyte interface: slow local charge compensation and a reversible electric field. *Phys. Chem. Chem. Phys.* **2015**, *17*, 16744–16751.

[9] Hammarström L. Accumulative Charge Separation for Solar Fuels Production: Coupling Light-Induced Single Electron Transfer to Multielectron Catalysis. *Acc. Chem. Res.* **2015**, *48*, 840–850.

[10] Abrahamsson M., Hedberg J. H. J., Becker H.-C., Staniszewski A., Pearson W. H., Heuer W. B., Meyer G. J. High Extinction Coefficient Ru-Sensitizers that Promote Hole Transfer on Nanocrystalline TiO_2. *ChemPhysChem* **2014**, *15*, 1154–1163.

[11] Argazzi R., Bignozzi C. A., Heimer T. A., Castellano F. N., Meyer G. J. Long-Lived Photoinduced Charge Separation across Nanocrystalline TiO_2 Interfaces. *J. Am. Chem. Soc.* **1995**, *117*, 11815–11816.

[12] Abrahamsson M., Johansson P. G., Ardo S., Kopecky A., Galoppini E., Meyer G. J. Decreased Interfacial Charge Recombination Rate Constants with N3-Type Sensitizers. *J. Phys. Chem. Lett.* **2010**, *1*, 1725–1728.

[13] Johansson P. G., Zhang Y., Meyer G. J., Galoppini E. Homoleptic 'Star' Ru(II)

Polypyridyl Complexes: Shielded Chromophores to Study Charge-Transfer at the Sensitizer-TiO_2 Interface. *Inorg. Chem.* **2013**, *52*, 7947–7957.

[14] Paulsson H., Kloo L., Hagfeldt A., Boschloo G. Electron transport and recombination in dye-sensitized solar cells with ionic liquid electrolytes. *J. Electroanal. Chem.* **2006**, *586*, 56–61.

[15] Gorlov M., Kloo L. Ionic liquid electrolytes for dye-sensitized solar cells. *Dalt. Trans.* **2008**, 2655. doi:10.1039/b716419j

[16] Mahanta S., Furube A., Matsuzaki H., Murakami T. N., Matsumoto H. Electron Injection Efficiency in Ru-Dye Sensitized TiO_2 in the Presence of Room Temperature Ionic Liquid Solvents Probed by Femtosecond Transient Absorption Spectroscopy: Effect of Varying Anions. *J. Phys. Chem. C* **2012**, *116*, 20213–20219.

[17] Li F., Jennings J. R., Wang X., Fan L., Koh Z. Y., Yu H., Yan L., Wang Q. Influence of Ionic Liquid on Recombination and Regeneration Kinetics in Dye-Sensitized Solar Cells. *J. Phys. Chem. C* **2014**, *118*, 17153–17159.

[18] Fabregat-Santiago F., Bisquert J., Palomares E., Otero L., Kuang D., Zakeeruddin S. M., Grätzel M. Correlation between Photovoltaic Performance and Impedance Spectroscopy of Dye-Sensitized Solar Cells Based on Ionic Liquids. *J. Phys. Chem. C* **2007**, *111*, 6550–6560.

[19] Feldt S. M., Lohse P. W., Kessler F., Nazeeruddin M. K., Grätzel M., Boschloo G., Hagfeldt A. Regeneration and recombination kinetics in cobalt polypyridine based dye-sensitized solar cells, explained using Marcus theory. *Phys. Chem. Chem. Phys.* **2013**, *15*, 7087.

[20] Oum K., Lohse P. W., Klein J. R., Flender O., Scholz M., Hagfeldt A., Boschloo G., Lenzer T. Photoinduced ultrafast dynamics of the triphenylamine-based organic sensitizer D35 on TiO_2, ZrO_2 and in acetonitrile. *Phys. Chem. Chem. Phys.* **2013**, *15*, 3906.

[21] Ardo S., Meyer G. J. Photodriven heterogeneous charge transfer with transition-metal compounds anchored to TiO_2 semiconductor surfaces. *Chem. Soc. Rev.* **2009**, *38*, 115–164.

[22] Pazoki M., Lohse P. W., Taghavinia N., Hagfeldt A., Boschloo G. The effect of dye coverage on the performance of dye-sensitized solar cells with a cobalt-based electrolyte. *Phys. Chem. Chem. Phys.* **2014**, *16*, 8503.

[23] Reddy P. Y., Giribabu L., Lyness C., Snaith H. J., Vijaykumar C., Chandrasekharam M., Lakshmikantam M., Yum J.-H., Kalyanasundaram K., Grätzel M., Nazeeruddin M. K. Efficient Sensitization of Nanocrystalline TiO_2 Films by a Near-IR-Absorbing Unsymmetrical Zinc Phthalocyanine. *Angew. Chemie Int. Ed.* **2007**, *46*, 373–376.

[24] Kelly C. A., Farzad F., Thompson D. W., Stipkala J. M., Meyer G. J. Cation-Controlled Interfacial Charge Injection in Sensitized Nanocrystalline TiO_2. *Langmuir* **1999**, *15*, 7047–7054.

[25] Williams G., Watts D. C. Non-symmetrical dielectric relaxation behaviour arising from a simple empirical decay function. *Trans. Faraday Soc.* **1970**, *66*, 80.

[26] Lindsey C. P., Patterson G. D. Detailed comparison of the Williams–Watts and Cole–Davidson functions. *J. Chem. Phys.* **1980**, *73*, 3348.

[27] Nakade S., Kanzaki T., Kubo W., Kitamura T., Wada Y., Yanagida S. Role of Electrolytes on Charge Recombination in Dye-Sensitized TiO_2 Solar Cell (1): The Case of Solar Cells Using the I^-/I_3^- Redox Couple. *J. Phys. Chem. B* **2005**, *109*, 3480–3487.

[28] Katoh R., Kasuya M., Kodate S., Furube A., Fuke N., Koide N. Effects of 4- tert -Butylpyridine and Li Ions on Photoinduced Electron Injection Efficiency in Black-Dye-Sensitized Nanocrystalline TiO 2 Films. *J. Phys. Chem. C* **2009**, *113*, 20738–20744.

[29] Yu Q., Wang Y., Yi Z., Zu N., Zhang J., Zhang M., Wang P. High-Efficiency Dye-Sensitized Solar Cells: The Influence of Lithium Ions on Exciton Dissociation, Charge Recombination, and Surface States. *ACS Nano* **2010**, *4*, 6032–6038.

[30] Koops S. E., O'Regan B. C., Barnes P. R. F., Durrant J. R. Parameters Influencing the Efficiency of Electron Injection in Dye-Sensitized Solar Cells. *J. Am. Chem. Soc.* **2009**, *131*, 4808–4818.

[31] Boschloo G., Häggman L., Hagfeldt A. Quantification of the Effect of 4- tert -Butylpyridine Addition to I^-/I_3^- Redox Electrolytes in Dye-Sensitized Nanostructured TiO_2 Solar Cells. *J. Phys. Chem. B* **2006**, *110*, 13144–13150.

[32] Göthelid M., Yu S., Ahmadi S., Sun C., Zuleta M. Structure-Dependent 4-Tert-Butyl Pyridine-Induced Band Bending at TiO_2 Surfaces. *Int. J. Photoenergy* **2011**, *2011*, 1–6.

[33] Bai Y., Zhang J., Wang Y., Zhang M., Wang P. Lithium-modulated conduction band edge shifts and charge-transfer dynamics in dye-sensitized solar cells based on a dicyanamide ionic liquid. *Langmuir* **2011**, *27*, 4749–4755.

[34] Zhang M., Zhang J., Bai Y., Wang Y., Su M., Wang P. Anion-correlated conduction band edge shifts and charge transfer kinetics in dye-sensitized solar cells with ionic liquid electrolytes. *Phys. Chem. Chem. Phys.* **2011**, *13*, 3788–3794.

[35] Moser J. E., Grätzel M. Observation of temperature independent heterogeneous electron transfer reactions in the inverted Marcus region. *Chem. Phys.* **1993**, *176*, 493–500.

[36] Kuciauskas D., Freund M. S., Gray H. B., Winkler J. R., Lewis N. S. Electron Transfer Dynamics in Nanocrystalline Titanium Dioxide Solar Cells Sensitized

with Ruthenium or Osmium Polypyridyl Complexes. *J. Phys. Chem. B* **2001**, *105*, 392–403.

[37] Cao Y., Zhang J., Bai Y., Li R., Zakeeruddin S. M., Grätzel M., Wang P. Dye-Sensitized Solar Cells with Solvent-Free Ionic Liquid Electrolytes. *J. Phys. Chem. C* **2008**, *112*, 13775–13781.

[38] Jennings J. R., Wang Q. Influence of Lithium Ion Concentration on Electron Injection, Transport, and Recombination in Dye-Sensitized Solar Cells. *J. Phys. Chem. C* **2010**, *114*, 1715–1724.

[39] Harris K. R., Kanakubo M., Woolf L. a. Temperature and Pressure Dependence of the Viscosity of the Ionic Liquids 1-Hexyl-3-methylimidazolium Hexafluorophosphate and 1-Butyl-3-methylimidazolium Bis(trifluoromethylsulfonyl)imide. *J. Chem. Eng. Data* **2007**, *52*, 1080–1085.

[40] Geng Y., Chen S., Wang T., Yu D., Peng C., Liu H., Hu Y. Density, viscosity and electrical conductivity of 1-butyl-3-methylimidazolium hexafluorophosphate + monoethanolamine and + N, N-dimethylethanolamine. *J. Mol. Liq.* **2008**, *143*, 100–108.

[41] Dintcheva N. T., Furlani M., Jayasundara W. J. M. J. S. R., Bandara T. M. W. J., Mellander B.-E., La Mantia F. P. Rheological behavior of PAN-based electrolytic gel containing tetrahexylammonium and magnesium iodide for photoelectrochemical applications. *Rheol. Acta* **2013**, *52*, 881–889.

[42] Oskam G., Bergeron B. V, Meyer G. J., Searson P. C. Pseudohalogens for Dye-Sensitized TiO_2 Photoelectrochemical Cells. *J. Phys. Chem. B* **2001**, *105*, 6867–6873.

[43] Wang P., Zakeeruddin S. M., Moser J.-E., Humphry-Baker R., Grätzel M. A Solvent-Free, $SeCN^-/(SeCN)_3^-$ Based Ionic Liquid Electrolyte for High-Efficiency Dye-Sensitized Nanocrystalline Solar Cells. *J. Am. Chem. Soc.* **2004**, *126*, 7164–7165.

[44] Wang P., Wenger B., Humphry-Baker R., Moser J.-E., Teuscher J., Kantlehner W., Mezger J., Stoyanov E. V., Zakeeruddin S. M., Grätzel M. Charge Separation and Efficient Light Energy Conversion in Sensitized Mesoscopic Solar Cells Based on Binary Ionic Liquids. *J. Am. Chem. Soc.* **2005**, *127*, 6850–6856.

[45] Ivaništšev V., V.Fedorov M. Interfaces between Charged Surfaces and Ionic Liquids: Insights from Molecular Simulations. *Electrochem. Soc. Interface* **2013**, 65–69.

[46] Salvatori P., Marotta G., Cinti A., Anselmi C., Mosconi E., De Angelis F. Supramolecular Interactions of Chenodeoxycholic Acid Increase the Efficiency of Dye-Sensitized Solar Cells Based on a Cobalt Electrolyte. *J. Phys. Chem. C* **2013**, *117*, 3874–3887.

[47] Ardo S., Sun Y., Staniszewski A., Castellano F. N., Meyer G. J. Stark Effects after Excited-State Interfacial Electron Transfer at Sensitized TiO_2 Nanocrystallites. *J. Am. Chem. Soc.* **2010**, *132*, 6696–6709.

[48] Kuwahara S., Taya S., Osada N., Shen Q., Toyoda T., Katayama K. Effect of electrolyte constituents on the motion of ionic species and recombination kinetics in dye-sensitized solar cells. *Phys. Chem. Chem. Phys.* **2014**, *16*, 5242.

[49] Pazoki M., Hagfeldt A., Boschloo G. Stark effects in D35-sensitized mesoporous TiO_2: influence of dye coverage and electrolyte composition. *Electrochim. Acta* **2015**, *179*, 174–178.

[50] Ooyama Y., Harima Y. Molecular Designs and Syntheses of Organic Dyes for Dye-Sensitized Solar Cells. *European J. Org. Chem.* **2009**, *2009*, 2903–2934.

[51] Ning Z., Zhang Q., Wu W., Pei H., Liu B., Tian H. Starburst Triarylamine Based Dyes for Efficient Dye-Sensitized Solar Cells. *J. Org. Chem.* **2008**, *73*, 3791–3797.

[52] Wang Z.-S., Koumura N., Cui Y., Takahashi M., Sekiguchi H., Mori A., Kubo T., Furube A., Hara K. Hexylthiophene-Functionalized Carbazole Dyes for Efficient Molecular Photovoltaics: Tuning of Solar-Cell Performance by Structural Modification. *Chem. Mater.* **2008**, *20*, 3993–4003.

Chapter 6

Conclusions

During my Ph.D. work, I have explored the possibility of increasing the performances of DSSC by modification of the photosensitizer chemical structure, semiconductor substrate composition and electrolyte solvent. Nevertheless, enhancement of the overall device efficiency was not the only goal of these studies, and topics such as the enhancement of dye stability, the expansion of available dye colorations and the need of insight on surface interaction mechanisms were addressed as well. Considering the complexity of the DSSC architecture, some of the above-mentioned activities pursued the aim of achieving modifications capable of enhancing efficiency without interfering with the overall electrochemical properties of the system.

The main part of my research activity consisted in the synthetic modification of the photoactive dyes by the introduction of electron withdrawing moieties, whose exploitation in DSSC was not reported yet, in different parts of the molecules. The first set of sensitizers was constituted by D-π-A dyes bearing a pyridine-containing anchoring moiety. (*Figure 6.1*)

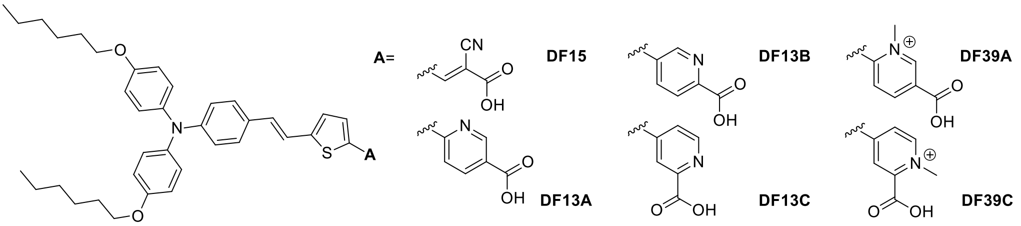

Figure 6 1: ***synthesized D- π -A dyes baring a pyridine-containing anchoring moiety.***

In this study large relevance was given to the fabrication of PV devices and their electronical characterization. The use of carboxy pyridine anchoring function was found to play a key role in enhancing the stability of dye absorption on TiO_2 substrates, proved both by chemical desorption experiments performed on the photoanode, and by aging tests of full PV devices. The proposed explanations for the isomers **DF13B** and **DF13C** increased in stability were the synergic linkage of the TiO_2 substrate by both the carboxylic function and the pyridinic nitrogen atom in anchoring, and the photo- thermal- stability of the substrate. Within the same project, I also performed the *N*-methyl-derivatization of the dyes. The carboxy-*N*-methylpyridinium dyes were synthesized aiming at enhancing device efficiency but, despite good spectroscopic features, they were found not to be enough stable on TiO_2 substrates and therefore unsuitable for application in DSSC.

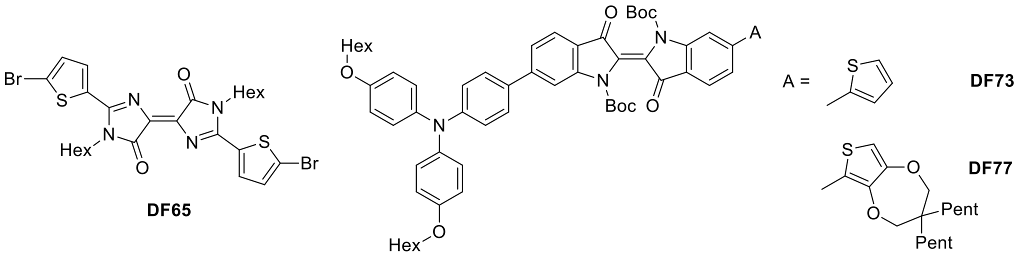

*Figure 6 2:**Synthesized dyes bearing a 5-membred heterocycle electron poor moiety.***

The second set of dyes had a D-A-π-A structure derived from the insertion of different heterocyclic chromophores inside the structure of **DF15** dye with the role of additional acceptor moieties. The first structural unit was a bisimidazolylidene-dione moiety, but the synthesized scaffold **DF65** (*Figure 6.2*) did not show the stability features desired for DSSC applications and this structure was abandoned. The second additional acceptor scaffold studied was Indigo. The enhancement of the, initially scarce, solubility of this compound was pursued by means of a bay-annulation derivatization of the scaffold or using the *t*-Boc protection strategy. A desymmetrization protocol *via* low-temperature Stille cross-coupling was employed to achieve D-A-π intermediates **DF73** and **DF77**. (*Figure 6.2*) Interestingly, upon *t*-Boc deprotection of a symmetric Indigo derivative, stable compounds, characterized by an intense green coloration, were obtained. The achievement of such a feature, uncommon in dyes for DSSCs, makes further development of this class of dyes particularly interesting.

The second topic of this study was the determination of light harvesting enhancement of the organic dye **DF15** due to electromagnetic interactions with metal nanocomposites used to functionalize the TiO_2 thin films constituting the DSSC photoanode. Here, I reported the synthesis of CTAB-stabilized monodisperse gold nanosphere colloids and the strategies used to form thin shells of oxides on the gold surface. A one-step procedure was reported for the functionalization and subsequent condensation of MPTMS to achieve coverage of the gold cores with thin homogeneous layers of SiO_2. Instead, $Ti(acac)_2(i\text{-}PrOH)_2$ was used to achieve good control of the TiO_2 layers growth on MAA functionalized gold surfaces. A protocol for the preparation of shelled AuNPs-doped thin semitransparent substrate of semiconductor was reported. An accurate method for the determination of dye loading and subsequent solid state spectroscopy investigation of dye-sensitized thin films proved that the nanocomposites were able to enhance the absorption properties of organic dyes. The absorption efficiency of the dyes was found to be enhanced by 81% in presence of AuNPs@TiO_2 in the semiconductor, and by 141% when AuNPs@SiO_2 were used instead. Thus, the outcome of this research opens the way to the use of core-shell nanocomposites to increase the efficiencies of organic dyes-based DSSCs as well. Nonetheless, due to the relative narrow adsorption bands of organic chromophore, speculations regarding the need of overlap between plasmonic absorption band and dye absorption band should still be probed.

In the last part of the manuscript, I reported investigations on the use of pure Ionic Liquids as electrolytes for DSSC. Kinetics studies have shown that ionic liquids can be used to slow down the interfacial charge recombination between TiO_2 electrons and oxidized organic dye **D35**, as well as between TiO_2 electrons and metallorganic dye $[Ru(dcb)_3]^{2+}$, while the recombination rates in **N3**/TiO_2 assemblies remained unaffected. By careful examination of the obtained kinetic data and literature reports, we attributed this behavior to an electrostatic effect at the TiO_2-dye-electrolyte interface. A mechanism where cations in the ILs are accumulated and/or adsorbed at the charged TiO_2 surface to locally compensate the charge of injected electrons was proposed. Electrostatic hindrance results in changes in the recombination rates. The extent of this effect might depend on the size of the ionic liquid cations and the structure of the dye, being the charge on the ligands the most important aspect. A consequence of the findings presented here is that the dye structure should be considered not only for its electron injection properties but also for how it may interact with the surrounding electrolyte. The study of electron interfacial dynamics can be used for probing local charge compensation and similar phenomena. In addition, control of interfacial charge recombination by modification of the surrounding electrolyte seems to be a practical and attractive strategy that could be useful in many solar energy conversion applications.